

Numerical Analyses of Geocell-Reinforced Granular Soils under Static and Repeated Loads

By

Xiaoming Yang

Submitted to the graduate degree program in Civil, Environmental, and
Architectural Engineering and the Graduate Faculty of the University of Kansas
in partial fulfillment of the requirements for degree of Doctor of Philosophy

Dr. Jie Han

Chairperson*

Dr. Weizhang Huang

Dr. Anil Misra

Dr. Robert L. Parsons

Dr. Steven D. Schrock

Committee members

Date defended: August 12, 2010

The dissertation Committee for Xiaoming Yang certifies that this is the approved version of the following dissertation:

**Numerical Analyses of Geocell-Reinforced Granular Soils
under Static and Repeated Loads**

Committee

Dr. Jie Han

Chairperson*

Dr. Weizhang Huang

Dr. Anil Misra

Dr. Robert L. Parsons

Dr. Steven D. Schrock

Committee members

Date approved: August 16, 2010

Table of Contents

Abstract	xiv
Acknowledgements.....	xvi
Chapter 1 Introduction.....	1
1.1 Background.....	1
1.2 Objective and scope.....	5
1.3 Organization of this dissertation.....	6
Chapter 2 Literature review.....	8
2.1 Overview.....	8
2.2 Constitutive models for granular soil.....	8
2.2.1 Under static load	9
2.2.2 Under repeated load	16
2.3 History of geocell.....	25
2.4 Geocell reinforced soil supporting static load	27
2.4.1 Experimental studies	27
2.4.2 Analytical and numerical studies	34
2.5 Geocell reinforced soil supporting repeated load	43
2.5.1 Experimental studies	43
2.5.2 Analytical and numerical studies	46
2.6 Summary.....	48
Chapter 3 Laboratory model tests	51

3.1	Overview.....	51
3.2	Static Load tests.....	52
3.2.1	Test setup and procedure.....	52
3.2.2	Material used	56
3.2.3	Test results and discussion	61
3.3	Moving-wheel test.....	63
3.3.1	Test setup and procedure.....	64
3.3.2	Materials used	68
3.3.3	Test results and discussion	78
3.4	Summary.....	88
Chapter 4	Numerical analysis of geocell-reinforced soil under a static load.....	91
4.1	Overview.....	91
4.2	FLAC ^{3D}	91
4.3	Material models and parameters	92
4.3.1	Sand	92
4.3.2	Geocell	94
4.4	Modeling of the static load test.....	96
4.4.1	Numerical mesh and boundary conditions	96
4.4.2	Numerical results	99
4.5	Parametric study	106
4.5.1	Unreinforced and reinforced bases	106
4.5.2	Effect of the thickness of the geocell-reinforced sand layer	113

4.5.3	Effect of the modulus of the geocell	114
4.5.4	Effect of the geocell-soil interface shear modulus.....	115
4.5.5	Effect of the type of subgrade.....	116
4.6	Summary.....	117
Chapter 5 Numerical analysis of geocell-reinforced soil under a repeated load.		120
5.1	Overview.....	120
5.2	Mechanistic-empirical model for geocell-reinforced soil.....	120
5.2.1	Three-dimensional tangent resilient modulus model.....	122
5.2.2	Initial horizontal stress increase due to compaction effort.....	125
5.2.3	Residual stress accumulated in the infill soil.....	130
5.2.4	Equivalent resilient modulus parameters.....	143
5.3	Material model and parameters	144
5.4	Modeling of the moving wheel test	146
5.4.1	Numerical mesh and boundary conditions	147
5.4.2	Load application	149
5.4.3	Resilient response	149
5.4.4	Permanent deformation	157
5.5	Parametric study	162
5.5.1	Reinforced and unreinforced bases	162
5.5.2	Effect of the resilient modulus of the infill material.....	163
5.5.3	Effect of the modulus of the geocell	164
5.5.4	Effect of the stiffness of the subgrade.....	165

5.6	Mechanistic-empirical design method for the geocell-reinforced base in paved and unpaved roads	167
5.6.1	Paved roads.....	167
5.6.2	Unpaved roads.....	168
5.7	Summary.....	169
Chapter 6	Conclusions and recommendations	172
6.1	Conclusions from this study.....	172
6.1.1	Experimental study	173
6.1.2	Numerical analyses on geocell-reinforced granular soil under a static load.....	175
6.1.3	Numerical analyses on geocell-reinforced granular soil under a repeated load.....	176
6.2	Recommendations for future studies.....	178
References	180
Appendix A	Cyclic triaxial tests on base materials and parameter calibration.....	190

List of Figures

Figure 1.1 Typical geometry of geocell	2
Figure 1.2 Examples of geocell application	4
Figure 2.1 Mohr-Coulomb model vs. Duncan-Chang model	15
Figure 2.2 Response of elastoplastic materials in shakedown theory (Collins et al. 1993b).....	18
Figure 2.3 Resilient response and permanent deformation of soil under repeated load.....	21
Figure 2.4 Typical test setup of the laboratory model test.....	28
Figure 2.5 Mohr circle construction for calculating the apparent cohesion of the geocell-soil composite (Bathurst and Karpurapu 1993).....	36
Figure 2.6 Configuration of single-cell and multi-cell reinforced soil sample for triaxial tests (Rajagopal et al. 1999).....	37
Figure 2.7 Failure envelopes with different configurations of geocell in p - q space($p=(\sigma_1 + \sigma_3)/2$, $q=(\sigma_1 - \sigma_3)/2$) (Rajagopal et al. 1999).....	38
Figure 2.8 Three-dimensional model of single cell-reinforced soil (Han et al. 2008)	41
Figure 2.9 Single-geocell-reinforced aggregate sample for resilient modulus test (Mengelt et al. 2000)	47
Figure 3.1 Static load test setup.....	53
Figure 3.2 Installation of strain gauge on the geocell.....	54
Figure 3.3 Pocket size of geocell (before installation)	55

Figure 3.4 Pocket size of geocell (after compaction)	55
Figure 3.5 Load plate and dial gauge setup	56
Figure 3.6 Grain size distribution of the sand	57
Figure 3.7 Triaxial compression test result.....	58
Figure 3.8 Isotropic compression test result.....	59
Figure 3.9 Stress-strain behavior of the geocell materials	60
Figure 3.10 Load vs. displacement.....	62
Figure 3.11 Tensile strain in geocell vs. pressure	63
Figure 3.12 Accelerated pavement testing facility	64
Figure 3.13 Moving-wheel test setup.....	66
Figure 3.14 DCP test results from clay subgrade	67
Figure 3.15 Installation of NPA geocell	67
Figure 3.16 Compaction curve of the subgrade clay	69
Figure 3.17 Unconfined compression test device	70
Figure 3.18 Unconfined compression test result	70
Figure 3.19 Grain size distribution of AB-3	71
Figure 3.20 Compaction curve of AB-3.....	72
Figure 3.21 Shear stress vs. displacement.....	73
Figure 3.22 Shear strength vs. normal stress	73
Figure 3.23 Cyclic triaxial test machine (UI-FastCell)	74
Figure 3.24 Grain size distribution of the river sand.....	76
Figure 3.25 Compaction curve of the river sand	76
Figure 3.26 Triaxial compression test result.....	77

Figure 3.27 Isotropic compression test result.....	77
Figure 3.28 Rut depth vs. Number of passes, N	79
Figure 3.29 Exhumed geocells in Sections 2 and 3	81
Figure 3.30 Road section profile before and after the test (Section 2).....	82
Figure 3.31 Road section profiles before and after the test (Section 3).....	82
Figure 3.32 Location of the strain gauges	83
Figure 3.33 Profile of the peak horizontal strain in geocell across the wheel path (Section 2)	86
Figure 3.34 Profile of the residual horizontal strain in geocell across the wheel path (Section 2)	86
Figure 3.35 Peak horizontal strain in geocell vs. number of passes (Section 2)	87
Figure 3.36 Residual horizontal strain in geocell vs. number of pass (Section 2).....	87
Figure 4.1 Triaxial compression test data vs. calculated results.....	93
Figure 4.2 Isotropic compression test data vs. calculated results	94
Figure 4.3 Interface shear behavior between the infill soil and the geocell	96
Figure 4.4 Numerical mesh for the static load tests.....	98
Figure 4.5 Horizontal displacement contour (Plate displacement = 10mm)	101
Figure 4.6 Horizontal stress contour (Plate displacement = 10mm)	102
Figure 4.7 Horizontal stress in the geocell (Plate displacement = 10mm)	103
Figure 4.8 Load-displacement curves (Test vs. Numerical results).....	105
Figure 4.9 Tensile strain on the geocell (Test vs. Numerical results)	105
Figure 4.10 Numerical mesh of the baseline model.....	108
Figure 4.11 Pressure-displacement curves of unreinforced vs. reinforced sand	111

Figure 4.12 Horizontal displacement contours	112
Figure 4.13 Effect of the thickness of geocell-reinforced sand on pressure- displacement curves.....	114
Figure 4.14 Effect of geocell modulus on pressure-displacement curves	115
Figure 4.15 Effect of geocell-soil interface shear modulus on pressure- displacement curves.....	116
Figure 4.16 Effect of subgrade soil on pressure-displacement curves	117
Figure 5.1 Modified general hysteretic K_0 -loading model (modified from Duncan and Seed, 1986)	127
Figure 5.2 Suggested relationship between $\sin\phi'$ and α (Duncan and Seed 1986) ..	128
Figure 5.3 Geocell stabilizes the passive earth failure	128
Figure 5.4 Initial horizontal stress after compaction in Section 1 and 2	130
Figure 5.5 Initial horizontal stress after compaction in Section 3 and 4	130
Figure 5.6 The stress state of the soil in a cyclic triaxial test after the sample reaches the resilient state	133
Figure 5.7 Measured resilient modulus vs. bulk stress for Rodefeld sand (Mengelt et al. 2000).....	140
Figure 5.8 Calculated resilient modulus vs. bulk stress for Rodefeld sand.....	140
Figure 5.9 Measured resilient modulus vs. bulk stress for Antigo silt loam (Mengelt et al. 2000)	141
Figure 5.10 Calculated resilient modulus vs. bulk stress for Antigo silt loam	141
Figure 5.11 Calculated vs. measured resilient moduli for Lodefild sand.....	142
Figure 5.12 Calculated vs. measured resilient moduli for Antigo silt loam	142

Figure 5.13 Numerical mesh of the response model (Section 2)	148
Figure 5.14 Contours of vertical displacement (Unit: m).....	151
Figure 5.15 Contours of vertical stress (Unit: Pa).....	152
Figure 5.16 Contours of vertical stress in the subgrade (Unit: Pa)	153
Figure 5.17 Contours of horizontal resilient stress in geocell (Unit: N/m)	154
Figure 5.18 Vertical resilient strains along the center line (Sections 1 and 2).....	155
Figure 5.19 Vertical resilient strains along the center line (Sections 3 and 4).....	156
Figure 5.20 Calculate vs. measured rut depths (Sections 3 and 4)	160
Figure 5.21 Accumulated rut depths of the road with vs. without geocell reinforcement	163
Figure 5.22 Accumulated rut depths of the road with different infill materials.....	164
Figure 5.23 Accumulated rut depth of the road with different geocell modulus.....	165
Figure 5.24 Accumulated rut depth of the road with different types of subgrade (high-quality infill material).....	166
Figure 5.25 Accumulated rut depth of the road with different types of subgrade (low-quality infill material)	167
Figure A.1 Permanent strain accumulation of Kansas River Sand	193
Figure A.2 Permanent strain accumulation of AB3	193

List of Tables

Table 2.1 Empirical permanent deformation models (after Lekarp et al. 2000b; Pérez et al. 2006)	24
Table 2.2 Experimental studies reviewed on geocell reinforced soil supporting static load.....	31
Table 2.3 Numerical modeling studies reviewed on geocell reinforced soil supporting static load	42
Table 2.4 Experimental studies reviewed on geocell-reinforced soil supporting repeated loads.....	45
Table 3.1 Stress-strain behavior of the geocell materials.....	60
Table 3.2 Creep resistance properties of the HDPE and the NPA materials (from PRS Mediterranean, Inc.)	61
Table 3.3 Other properties of the NPA material (from PRS Mediterranean, Inc.)	61
Table 3.4 Peak horizontal strain in the geocell (Unit: %, Positive = Tension).....	83
Table 3.5 Residual horizontal strain in the geocell (Unit: %, Positive = Tension)	84
Table 4.1 Duncan-Chang model parameters for the sand.....	93
Table 4.2 Model parameters for the geocell.....	95
Table 4.3 Constitutive models and parameters used in the baseline model	109
Table 5.1 Material parameters from Mengelt et al. (2000)	138
Table 5.2 Measured and calculated resilient moduli of unreinforced and geocell-reinforced sand.....	139

Table 5.3 Measured and calculated resilient modulus of unreinforced and geocell-reinforced silt loam	139
Table 5.4 Material parameters of each material.....	145
Table 5.5 Equivalent resilient modulus parameters for the geocell reinforced sand	146
Table 5.6 Layer thickness and materials in the response model	147
Table 5.7 Some resilient responses from the response models	150
Table 5.8 Calibrated parameters for rutting prediction from Section 2 (based on permanent deformation test data)	158
Table 5.9 Calibrated parameters for rutting prediction from Section 2 (based on the permanent deformation model in MEPDG (Equation 2.24))	159
Table 6.1 Features of the numerical models developed in this study	172
Table A.1 Cyclic triaxial test on Kansas River Sand (resilient modulus)	191
Table A.2 Cyclic triaxial test on Kansas River Sand (Permanent deformation) .	191
Table A.3 Cyclic triaxial test on AB-3 (resilient modulus)	192
Table A.4 Cyclic triaxial test on AB-3 (Permanent deformation).....	192

Abstract

Geocell is one of the geosynthetic products used primarily for soil reinforcement. It was originally developed by US Army Corps of Engineers in 1970s for quick reinforcement of cohesionless soil in the military field. Due to its unique three-dimensional geometry, geocell can provide great lateral confinement to the infill soil without relying on the interlocking or friction with the infill soil. Despite the successful applications in various types of civil engineering projects, the mechanism of geocell reinforcement has not been well understood, especially for load-supporting applications.

In this study, laboratory model tests (including static load tests and moving wheel load tests) were performed to characterize the performance of the geocell-reinforced soil. A total of four types of geocell (manufactured by PRS Mediterranean, Inc.) were tested in this study. One was made from conventional high density polyethylene (HDPE) and the other three were made from novel polymer alloy (NPA). NPA is a new material characterized by flexibility at low temperatures similar to HDPE with elastic behavior similar to engineering thermoplastic. Test result showed that geocell products tested in this study can improve the modulus and strength of the granular soil under static load, as well as reduce the permanent deformation of the unpaved road under moving wheel loads.

Three-dimensional numerical models were developed in this study to simulate the behavior of geocell-reinforced soil under static and repeated loads. In the model for static loading, the infill soil is modeled using a non-linear elastoplastic model (also known as the Duncan-Chang model), and the geocell was modeled using linear elastic plate model. A mechanistic-empirical model was developed for NPA geocell-reinforced soil under repeated loads. This model was developed based on the stress-dependent response model in the current mechanistic-empirical pavement design guide (MEPDG). Some modifications were made to consider (a) the three-dimensional constitutive equation of tangent resilient modulus, (b) the compaction-induced initial horizontal stress in the soil, and (c) the residual stress increase due to the accumulated permanent deformation of geocell with the number of load passes. Analyses showed that the numerical models created in this study can well simulate the experimental result from the geocell-reinforced soils. Based on the calibrated numerical models, a parametric study was performed to investigate the effects from various factors, i.e., (a) thickness of the geocell-reinforced layer, (b) geocell modulus, (c) subgrade stiffness and strength, (d) interface shear modulus, and (e) infill material modulus. The mechanistic-empirical design methods for paved and unpaved roads with geocell-reinforced bases were also discussed.

Acknowledgements

First of all, I would like to express my deepest gratitude to my adviser, Professor Jie Han, for his guidance, support, care, and encouragement through my Ph.D. study. Professor Han is a very nice person and very dedicated to his students. Besides advising our studies, he also looks for every opportunity for us to develop useful skills for our future careers. His office is always open to us and all kinds of discussions. I really enjoy my four-year study with him at the University of Kansas.

This research was jointly funded by the University of Kansas, Transportation Research Institute from Grant #DT0S59-06-G-00047, provided by the US Department of Transportation – Research and Innovative Technology Administration and PRS Mediterranean, Inc. in Israel. Dr. Robert Honea, the director of the Kansas University Transportation Research Institute (KUTRI), Mr. Oded Erez, president, Mr. Izhar Halahmi, chief scientist, and Dr. Ofer Kief, pavement and soil consultant, of PRS Mediterranean, have provide great support for this research. Their supports are greatly appreciated.

The experiments in this study were performed at the University of Kansas, Kansas State University, and the University of Illinois at Urbana-Champaign. A number of people have helped in the experimental works. Sanat K. Pokharel (Ph.D. candidate) from the University of Kansas shared a lot of work in

preparation and measurement of the moving wheel tests as well as laboratory and in-situ material tests. Professor Mustaque Hossain at Kansas State University provided technical support on the moving wheel tests. Mr. Randy Testa (research technician), Dr. Chandra Manandhar (post-doc), Luke McIntosh (undergraduate research assistant), and other students from Kansas State University helped in preparing the unpaved road sections. Dr. Sari W A Abusharar (post-doc research associate), Cheng Lin (graduate research assistant), Dr. Anil Bhandari, Yu Qian (graduate research assistant), Yanli Dong (visiting student from China), Subhash Thakur (graduate research assistant), and Yan Jiang (visiting student from China) from the University of Kansas also helped in preparing the unpaved road sections and exhuming the sections after the tests. Mr. Jim Weaver (laboratory manager) and Mr. Matthew Maksimowiczat (laboratory technician) provided technical support in the laboratory tests at the University of Kansas. Professor Erol Tutumluer and his students, Maziar Moaveni (graduate research assistant) and Debakanta Mishra (graduate research assistant), from the University of Illinois at Urbana-Champaign provided generous support and help in running the resilient modulus tests. I would like to extend my sincere gratitude to all these people.

I would like to thank my Ph.D committee members, Professor Robert L. Parsons, Professor Anil Misra, Professor Steven D. Schrock, and Professor Weizhang Huang for their guidance and help in reviewing this dissertation. I would also

like to thank Professor Dov Leshchinsky from the University of Delaware for all the valuable discussions and supports on this study.

Finally, I want to thank my family especially my wife for their support and understanding throughout my study. Since we got married, my wife has been taking care of most of the housework and meanwhile working on her own Ph.D. dissertation. Without the efforts she made, I would not be able to focus on my dissertation and finish it on time.

Chapter 1 Introduction

1.1 Background

Since 1970s, geosynthetics have been increasingly used as construction materials in civil engineering projects such as roads, retaining walls, landfills, etc. Today, there are many types of geosynthetic products (e.g., geogrid, geotextile, geocell, geomembrane, etc.) available in the market. Each product is designed to solve a particular range of civil engineering problems.

Geocell is one of the geosynthetic products used primarily for soil reinforcement. It was originally developed by the US Army Corps of Engineers in 1970s for quick reinforcement of cohesionless soil in the military field. Like other geosynthetic products, geocell is usually made from polymeric materials (e.g., HDPE). For convenient transportation, most geocell products have a foldable three-dimensional geometry (often honeycomb shaped after stretched, as shown in Figure 1.1). During construction, geocell has to be first stretched to the desired width and fixed to a leveled surface. A layer of nonwoven geotextile is often placed under the geocell to separate the infill material from the underlying soil. The infill material is then poured into the pockets of the geocell. Compaction may be required depending on the type of application. Today, geocell has been successfully used in various types of civil engineering projects

as a quick and effective technique of soil reinforcement. Some examples of the application of geocell are shown in Figure 1.2.

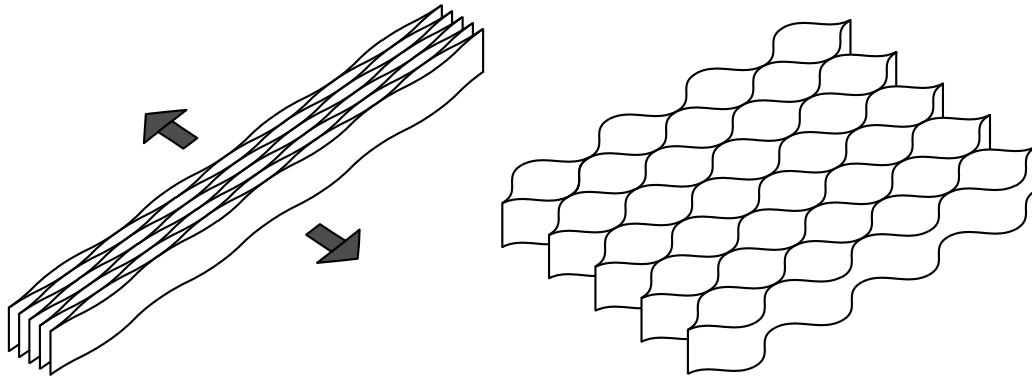
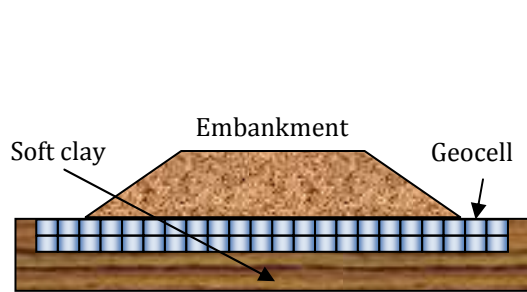


Figure 1.1 Typical geometry of geocell

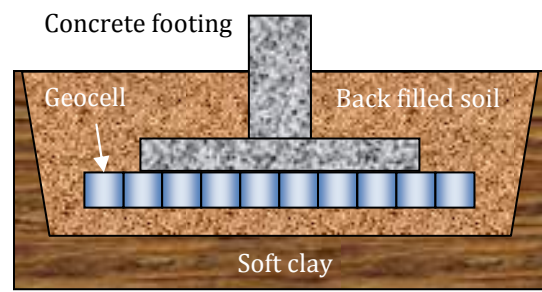
The most important purpose of using geocell reinforcement is to support load, either static or repeated. Figure 1.2(a, b) shows two examples of geocell reinforcement supporting static load. In these two cases, geocell is used to improve the bearing capacity of the soft soil and meanwhile reduce the settlement. Figure 1.2(c, d) shows the application of geocell-reinforced base courses supporting repeated traffic load in paved and unpaved roads. In this case, the function of geocell is to provide lateral confinement to the cohesionless base course materials. Geocell reinforcement will increase the stiffness and shear strength of the base course layer, which will help distribute the wheel load to a wider area onto the soft subgrade. As a result, the rutting of the road (caused by the permanent deformation of the base course and subgrade soils) after a certain number of wheel passes will be reduced. In other words, the required design thickness of the road base course can be reduced to meet the

same rut depth design criterion. Besides load-support, geocell can be used for erosion control and earth retaining structures (as shown in Figure 1.2(e, f)). For these applications, the primary function of geocell is to provide lateral confinement to the soils.

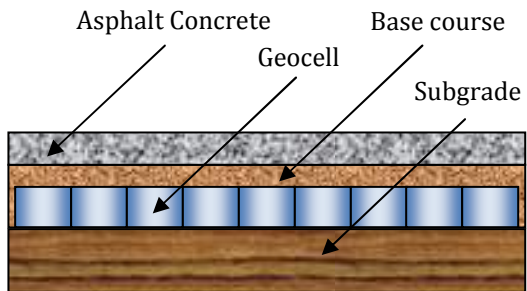
In contrast to the successful application of geocell in civil engineering projects, the mechanism of geocell reinforcement has not been well understood, especially for load-supporting applications. In the past, most of the research studies on the load-supporting geosynthetic reinforcement focused on planar geosynthetic products such as geogrid and geotextile. Only a limited number of studies aimed to develop design methods for the geocell reinforcement. Widely accepted design methods for different applications of geocell are still unavailable. Such a gap between theory and application limited the usage of geocell. To facilitate the development of design methods for geocell reinforcement for load-supporting purposes, the behavior of geocell-reinforced soil, under both static and repeated loading conditions, has to be studied.



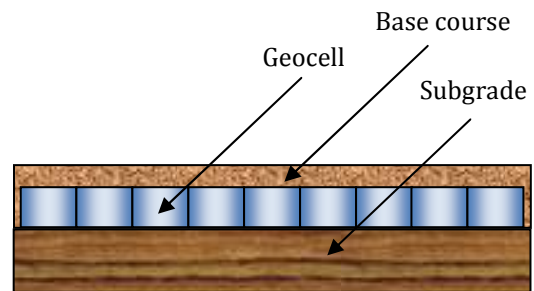
(a) Embankment foundation



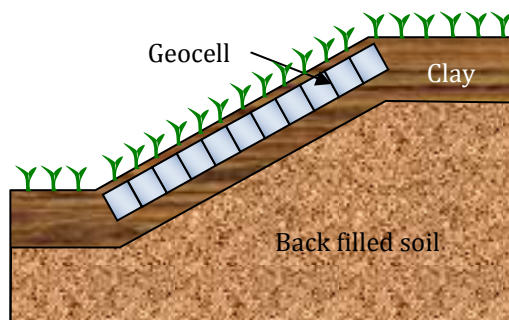
(b) Spread footing foundation



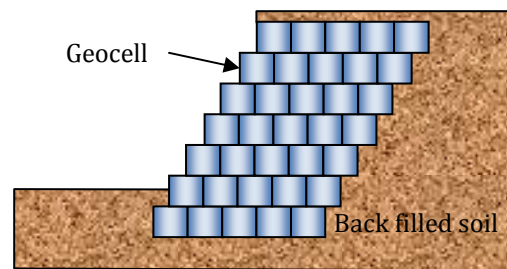
(c) Paved road



(d) Unpaved road



(e) Slope erosion control



(f) Earth Retaining wall

Figure 1.2 Examples of geocell application

1.2 Objective and scope

The objective of this study is to investigate the behavior of the geocell-reinforced soils under static and repeated loads. The findings of this study will help develop design methods for geocell reinforcement for load-supporting purposes. Numerical analysis is employed as the major investigation tool to study the mechanism of geocell reinforcement.

In this study, numerical models are created using a commercial finite difference code, Fast Lagrangian Analysis of Continua in Three-Dimensions (FLAC^{3D}). Two sets of numerical models were created for modeling the geocell-reinforced soil under static and repeated loading conditions. The numerical models are able to simulate:

- the stress dependent non-linear elastic behavior of granular soils;
- the elastic behavior of geocell;
- the normal and the frictional stresses between soil-geocell interface;
- the increased stiffness and shear strength of the geocell-reinforced soil when subjected to static loads;
- the increased resilient modulus and the reduced permanent deformation of the geocell-reinforced soil when subjected to repeated loading;

The behavior of geocell-reinforced soil is influenced by numerous factors, such as the type of the infill soil, the geometry and the material properties of geocell,

temperature, loading conditions, etc. It is extremely difficult to create and calibrate such a numerical model that can consider all these factors. Thus, it is necessary to set the following limits to the scope of this study:

- The modulus and tensile strength of polymeric materials are often influenced by temperature, loading rate, stress level, etc. In this study, all the laboratory tests were performed under room temperature. The maximum tensile strain of the geocell measured during the tests was relatively low to exhibit considerable rate-dependent or stress-dependent behavior. So, geocell will be modeled using a linear elastic membrane model in this study.
- The behavior, especially the plastic behavior, of granular soil under repeated load is very complicated and still under investigation. In this study, the elasto-plastic constitutive models and empirical relationships proposed by the previous researchers are reviewed. However, the focus of this study will not be placed on this area. Instead, it will be on the interaction between geocell and the infill soil.

1.3 Organization of this dissertation

This dissertation comprises of five chapters and one appendix. Following this chapter, a literature review of the previous studies on the related areas is presented in chapter two. Chapter three describes the laboratory model tests performed to evaluate the behavior of geocell-reinforced soils under static and

repeated loads. The development of the numerical models and the numerical analyses of the behavior of geocell-reinforced soils under static and repeated loads are covered in chapter four and chapter five respectively. Appendix A presents the results of the cyclic triaxial tests on different base materials and the calibrated material parameters.

Chapter 2 Literature review

2.1 Overview

This chapter provides a literature review on the related topics of this study. Firstly, the constitutive models for the granular soil are discussed. Then a brief history about the development of the geocell product is introduced. After that, the previous studies on geocell reinforced granular soil are reviewed in two following sections, one covering static load support and the other covering repeated load support. In each section, the experimental and analytical/numerical studies are discussed separately.

2.2 Constitutive models for granular soil

A constitutive model (or constitutive equation) is the mathematical approximation of the stress-strain behavior of a material. It is an essential, if not the most important, component of the finite element/difference analysis. The stress-strain relationship of soils is often very complicated depending on soil type, water content, density, stress level, etc. It is neither feasible nor necessary to simulate all the characteristics of the soil behavior using one constitutive model. Instead, constitutive models are often developed to capture part of the important characteristic behaviors of a particular type of soil. In the last four

decades, numerous constitutive models were developed. In this section, a number of the constitutive models for granular soils were reviewed in two categories, one for modeling granular soils under static load and the other for modeling the granular soils under repeated load. This literature review will serve as the basis of the constitutive model selection in this study.

2.2.1 Under static load

2.2.1.1 Linearly elastic model

The simplest constitutive model is the isotropic linearly elastic model. In this model, the stress-strain relationship can be determined by any two of the four material properties (i.e., Young's modulus E , Poisson's ratio ν , bulk modulus K , and shear modulus G). The stress-strain relationship of an isotropic linearly elastic model can be expressed in Equation 2.1 (also known as the generalized form of Hooke's Law):

$$\begin{aligned}
 \varepsilon_{11} &= \frac{1}{E} [\sigma_{11} - \nu(\sigma_{22} + \sigma_{33})] \\
 \varepsilon_{22} &= \frac{1}{E} [\sigma_{22} - \nu(\sigma_{11} + \sigma_{33})] \\
 \varepsilon_{33} &= \frac{1}{E} [\sigma_{33} - \nu(\sigma_{11} + \sigma_{22})] \\
 \varepsilon_{12} &= \frac{\sigma_{12}}{2G} \\
 \varepsilon_{13} &= \frac{\sigma_{13}}{2G} \\
 \varepsilon_{23} &= \frac{\sigma_{23}}{2G}
 \end{aligned} \tag{2.1}$$

An elastic model can simulate the elastic (recoverable) deformation of soil in response to external forces. However, in most cases, soil's behavior is so complicated that the assumption of elasticity is no longer acceptable. As pointed out by Lade (2005), phenomena such as plastic strain, stress-path dependency, shear-dilatancy, rotation of principal stress axes, and most near and post failure behaviors of soil cannot be modeled by elastic models. If any of the above mentioned phenomena are critical for a particular problem, an elastoplastic constitutive model for soil must be used in the numerical analysis.

2.2.1.2 Elastoplastic model

All the elastoplastic constitutive models are based on some plasticity theories. Different elastoplastic constitutive models describe the behavior of soil by using different yield criteria, hardening/softening laws and flow rules. One of the simplest elastoplastic models is the linearly elastic perfectly plastic model (also known as the Mohr-Coulomb model in most finite element/difference programs). In this model, Mohr-Coulomb's yield criterion and a non-associated flow rule for shear failure were used. Equation 2.2 shows a simple form of Mohr-Coulomb's yield criterion.

$$\tau = c + \sigma \tan (\phi) \quad 2.2$$

where τ and σ are respectively the shear stress and the normal stress on the plain on which slip is initiated, and c and ϕ are respectively the cohesion and the internal friction angle of the soil. In terms of maximum and minimum principle stresses, Mohr-Coulomb's yield criterion can be written as

$$\frac{\sigma_1 - \sigma_3}{2} = \frac{\sigma_1 + \sigma_3}{2} \sin(\phi) + c \cos(\phi) \quad 2.3$$

The Mohr-Coulomb model was found by many studies to be effective in modeling the shear strengths of soils and rocks. However, it assumes the elastic properties of soil as constants, which is not true since the modulus of soil is often stress-dependent. This assumption sometimes leads to considerable deviation between the calculated and the actual deformation of soil especially when the soil is subjected to some forms of reinforcement. For this reason, when modeling the geosynthetic reinforced soil, some researchers chose to use non-linear elastoplastic models to account for the increased stiffness of soil due to additional confining stress.

To account for the non-linearity, Kondner (1963) proposed using a hyperbolic equation (Equation 2.4) to fit the triaxial test stress-strain curves of soil:

$$(\sigma_1 - \sigma_3) = \frac{\varepsilon_1}{\frac{1}{E_i} + \frac{\varepsilon_1}{(\sigma_1 - \sigma_3)_{ult}}} \quad 2.4$$

where E_i is the initial tangent modulus or the initial slope of the stress-strain curve. $(\sigma_1 - \sigma_3)_{ult}$ is the asymptotic value of the deviatoric stress. ε_1 is the axial strain. Janbu (1963) suggested using the Equation 2.5 to represent the relation between E_i and σ_3 :

$$E_i = K p_a \left(\frac{\sigma_3}{p_a} \right)^n \quad 2.5$$

where K is the modulus number, n is the modulus exponent, and p_a is the atmospheric pressure. K and n are both dimensionless parameters, which can be obtained from a series of triaxial tests under different confining stress σ_3 . Equation 2.5 indicates that the initial tangent modulus E_i increases with the confining stress σ_3 . It should be noted that σ_3 here can only take a positive value, which means the soil is under compressive confining stress. Unlike triaxial test, a soil element may experience tensile stress in the numerical model. To avoid mathematical error, a very small confining stress (e.g., $\sigma_3 = 1$ Pa) should be used in Equation 2.5 if $\sigma_3 \leq 0$. $(\sigma_1 - \sigma_3)_{ult}$ can be related to the triaxial compressive strength $(\sigma_1 - \sigma_3)_f$ of soil by:

$$(\sigma_1 - \sigma_3)_f = R_f (\sigma_1 - \sigma_3)_{ult} \quad 2.6$$

where R_f is the failure ratio, which can also be determined from a series of triaxial tests, and $(\sigma_1 - \sigma_3)_f$ can be calculated based on Mohr-Coulomb's yield criterion:

$$(\sigma_1 - \sigma_3)_f = \frac{2c \cos \phi + 2\sigma_3 \sin \phi}{1 - \sin \phi} \quad 2.7$$

Note that Equation 2.7 is simply a transformation from Equation 2.3.

In a finite element/difference analysis, a stress-strain relationship should be defined in an incremental form. For modeling non-linear stress-strain behavior, tangent modulus must be used. Duncan et al. (1980) derived the equation for the tangent Young's modulus E_t by substituting Equations 2.5, 2.6, and 2.7 into Equation 2.4, and then differentiating Equation 2.4 with respect to the axial strain ε_1 :

$$E_t = \left[1 - \frac{R_f(1 - \sin \phi)(\sigma_1 - \sigma_3)}{2c \cos \phi + 2\sigma_3 \sin \phi} \right]^2 K p_a \left(\frac{\sigma_3}{p_a} \right)^n \quad 2.8$$

As mentioned previously, the elastic stress-strain relationship needs two elastic properties to be determined. Duncan et al. (1980) suggested use the following equation to calculate the bulk modulus B :

$$B = K_b p_a \left(\frac{\sigma_3}{p_a} \right)^m \quad 2.9$$

where K_b and m are respectively the dimensionless bulk modulus number and the bulk modulus exponent. Duncan et al. (1980) also considered the stress-dependency of friction angle:

$$\phi = \phi_0 - \Delta\phi \log_{10} \left(\frac{\sigma_3}{p_a} \right) \quad 2.10$$

where ϕ_0 is the friction angle when $\sigma_3 = 1$ atmosphere, and $\Delta\phi$ is the reduction of friction angle for every 10-times increase in σ_3 .

Equations 2.8, 2.9, and 2.10 together are also referred to as the Duncan-Chang model. All the nine parameters (i.e., c , ϕ , R_f , K , n , K_b , m , ϕ_0 , and $\Delta\phi$) can be obtained from a series (at least three) of triaxial tests with the sample volume change monitored. Obviously, the Duncan-Chang model is just a modification of the Mohr-Coulomb model with considerations to the stress-dependency of soil. A qualitative comparison of the Mohr-Coulomb model and the Duncan-Chang model is shown in Figure 2.1.

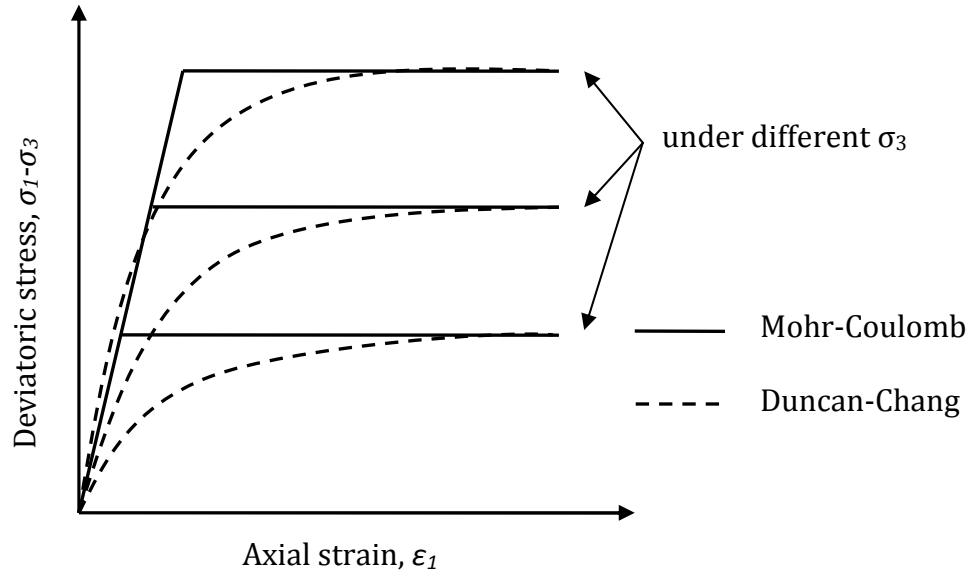


Figure 2.1 Mohr-Coulomb model vs. Duncan-Chang model

For its simplicity and effectiveness, the Duncan-Chang model has gained wide popularity. However, like every constitutive model, the Duncan-Chang model also has its limitations. First of all, this model was developed based on the observation of triaxial test data, where soil is in an axisymmetric situation ($\sigma_2 = \sigma_3$). Thus when applying this model to a three dimensional problem, the effect of σ_2 will be ignored. To overcome this issue, a simple modification adopted by some researchers (e.g., Rodriguez-Roa 2000) is substituting all the (σ_3/p_a) terms in Equations 2.8 to 2.10 by $(\sigma_2 + \sigma_3)/(2p_a)$. Secondly, as noticed by Boscardin et al. (1990), the bulk modulus B in Equation 2.9 is the secant bulk modulus. Boscardin et al. (1990) proposed using the following equation instead of Equation 2.9 for calculating the tangent bulk modulus B_t :

$$B_t = B_i \left(1 + \frac{\sigma_m}{B_i \varepsilon_u} \right)^2 \quad 2.11$$

where B_i is the initial bulk modulus when $\sigma_3 = 1$ atmosphere, ε_u is the asymptotic value of the volumetric strain. These two parameters from an isotropic compression test. σ_m is the mean effective stress ($\sigma_m = (\sigma_1 + \sigma_2 + \sigma_3)/3$).

2.2.2 Under repeated load

Under repeated load, the behavior of soil is more complicated than under static load. Granular soil can develop considerable plastic deformation under repeated load, even when the magnitude of the repeated load is lower than the shear strength of the soil determined under static load test. This phenomenon is very common in paved and unpaved roads, where rutting of the road is resulted by the repeated application of wheel load. In the last thirty years, many studies were carried out to improve our understanding about the response of granular soil to repeated load and also to improve the design method of paved and unpaved roads.

2.2.2.1 Shakedown theory

Shakedown theory was originally developed for analyzing metallic structures under cyclic loadings and was introduced to pavement analysis by Sharp and Booker (1984). According to shakedown theory, as described by Collins et al. (1993b), the stress-strain response of granular soil under different levels of repeated load can be categorized into four types (shown in Figure 2.2):

(1) Purely elastic

When the load level is sufficiently small, the material only exhibits elastic response.

(2) Elastic shakedown

When the load is a little lower than the elastic shakedown limit, the material exhibits elastoplastic response in a finite number of load cycles. With the number of load cycle increasing, residual stress will built up in the soil and the permanent strain developed in each cycle will become smaller and smaller. Finally the material will reach a purely elastic response. Such behavior is also called “shakedown”.

(3) Plastic shakedown;

When the load is larger than the elastic shakedown limit and lower than the plastic shakedown limit, the material will also reach a steady state after a finite

number of load cycles. But at the steady state, the material will still absorb some energy in each load cycle.

(4) Incremental collapse or ratcheting.

When the repeated load is larger than the plastic shakedown limit, plastic strain will accumulate rapidly in the material. The material will fail in a relatively short term.

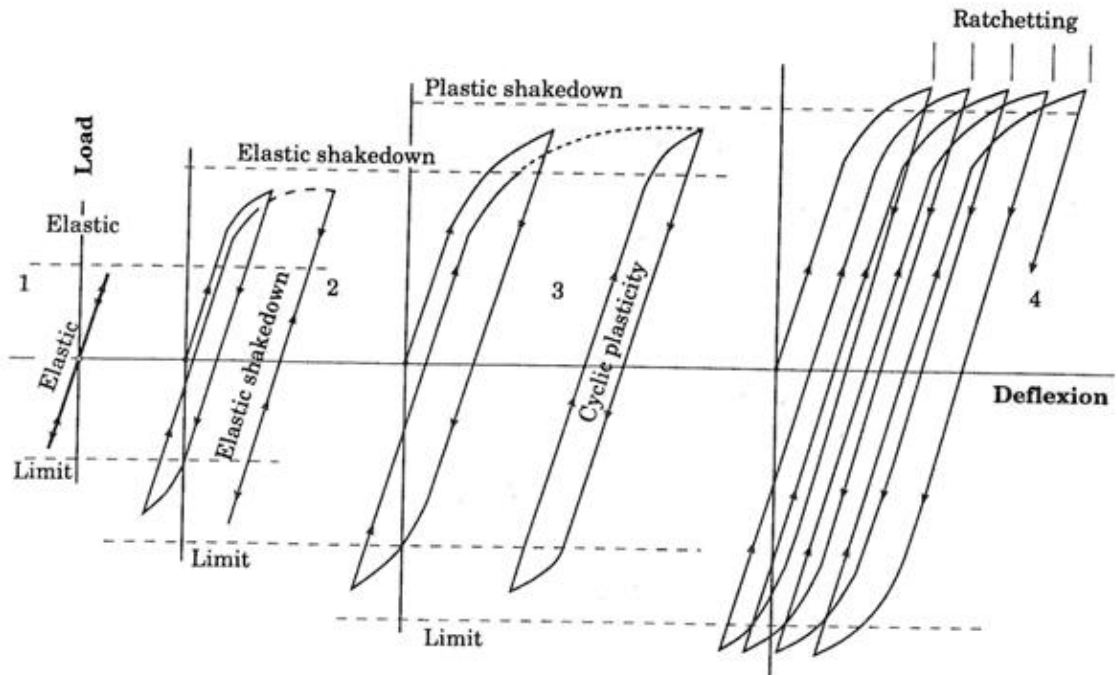


Figure 2.2 Response of elastoplastic materials in shakedown theory (Collins et al. 1993b)

According to shakedown theory, the target of pavement design is to avoid the maximum cyclic stress in any pavement layer exceeding the plastic shakedown

limit, given that the accumulated permanent strain is sufficiently small when all the pavement layers “shakedown”. However, shakedown theory cannot be easily incorporated into a routine pavement design, because the shakedown limits are difficult to estimate. Some researchers (Collins et al. 1993a; Boulbibane et al. 1999; Collins and Boulbibane 2000; García-Rojo and Hermann 2005) used upper bound theorem (due to Koiter 1960) and/or lower theorem (due to Melan 1938) to approximate the shakedown limits of soil under particular loading conditions. Other researchers proposed simplified equations to estimate the shakedown limit. For example, (Werkmeister et al. 2003) proposed using the following equation to characterize the critical stress condition at the plastic shakedown limit:

$$\sigma_{1 \max} = \alpha \left(\frac{\sigma_{1 \max}}{\sigma_c} \right)^\beta \quad 2.12$$

where σ_1 is the total axial stress, σ_c is the confining pressure, and α and β are model constants that can be calibrated by a series of cyclic triaxial tests. However, such kind of simplified models have not gained wide acceptance yet.

2.2.2.2 Mechanistic-Empirical model

As discussed above, the constitutive behavior of granular soil under repeated load is very complicated. Although some elastoplastic constitutive models (Mróz

1983; Desai and Faruque 1984; Bardet 1986; Bonaquist and Witczak 1997; Desai 2007) in this category were developed, the implementation of these models in pavement design and analysis is still under investigation. First of all, directly using an elastoplastic model to simulate the pavement response under each wheel pass for the entire service life of the road is extremely time-consuming. Secondly, these models often require more parameters, which are too complicated for normal design agencies to determine.

In the newly developed pavement design guide in the United States, the behavior of granular soil under repeated load is analyzed using a mechanistic-empirical model. This model was based on the observation that when the applied load is lower than a “threshold level” (also called the “elastic shakedown limit” in the shakedown theory), granular soil will (1) eventually become purely elastic after a large number of load passes (also called resilient response), and (2) accumulate permanent strain ϵ_p with the increase of the number of load cycle N , as shown in Figure 2.3. In the mechanistic-empirical model, these two phenomena were modeled separately by the response model and the permanent deformation model (also called damage model). The response model simulates the resilient response of the pavement structure characterized by the resilient modulus M_r and the Poisson’s ratio ν . The permanent deformation model is the empirical correlation between the permanent strain ϵ_p and the resilient strain ϵ_r with different number of wheel passes N .

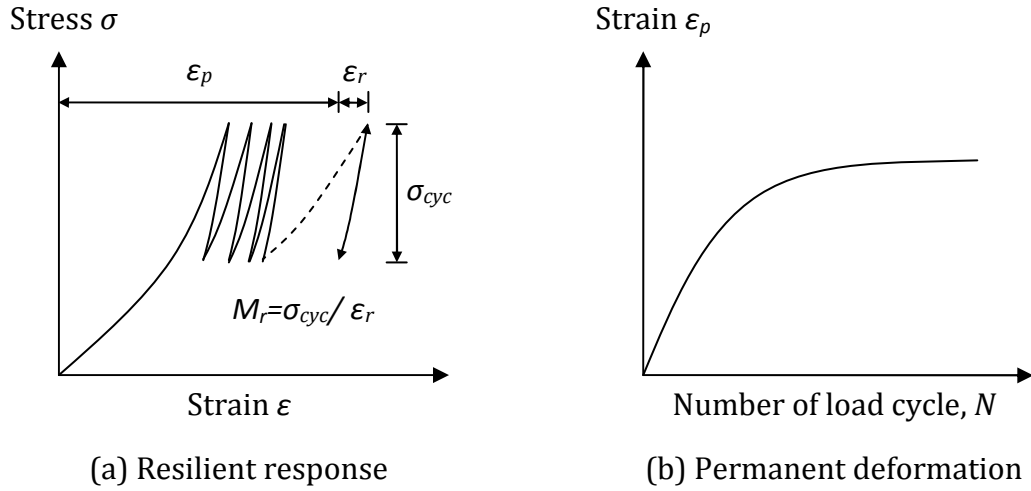


Figure 2.3 Resilient response and permanent deformation of soil under repeated load

unbound aggregates. As they summarized, the resilient response of unbound aggregates is influenced by several factors such as stress, density, grading, moisture, aggregate type and particle shape. Given a particular type of soil, the resilient modulus and the Poisson's ratio are both related to stress. A number of models were proposed to define such correlations. For example, the K- θ model (Hicks 1970) correlates the resilient modulus with the bulk stress θ ($\theta = \sigma_1 + \sigma_2 + \sigma_3$):

$$M_r = k_1 p_a \left(\frac{\theta}{p_a} \right)^{k_2} \quad 2.13$$

where p_a is atmospheric pressure, k_1 and k_2 are dimensionless parameters. Uzan (1985) included shear stress into the K- θ model and proposed the following equation:

$$M_r = k_1 p_a \left(\frac{\theta}{p_a} \right)^{k_2} \left(\frac{\tau_{oct}}{p_a} \right)^{k_3} \quad 2.14$$

where θ is the bulk stress; τ_{oct} is the octahedral shear stress ($\tau_{oct} = \sqrt{(\sigma_1 - \sigma_2)^2 + (\sigma_2 - \sigma_3)^2 + (\sigma_1 - \sigma_3)^2} / 3$); k_1 , k_2 , and k_3 are dimensionless parameters. Andrei (1999) proposed a more general form of the previous models:

$$M_r = k_1 p_a \left(\frac{\theta - 3k_6}{p_a} \right)^{k_2} \left(\frac{\tau_{oct}}{p_a} + k_7 \right)^{k_3} \quad 2.15$$

Equation 2.15 with $k_6 = 0$ and $k_7 = 1$ has been adopted by the current Mechanistic-Empirical Pavement Design Guide (MEPDG) developed by the NCHRP Project 1-37a (NCHRP 2004):

$$M_r = k_1 p_a \left(\frac{\theta}{p_a} \right)^{k_2} \left(\frac{\tau_{oct}}{p_a} + 1 \right)^{k_3} \quad 2.16$$

Dimensionless parameters k_1 , k_2 , and k_3 were suggested to be obtained from cyclic triaxial tests run at several different confining and deviatoric stresses. Yau (2002) performed a non-linear regression using data from the Long Term Pavement Performance (LTPP) database and proposed statistical relationships between k_1 , k_2 , k_3 and the soil properties (such as grain size distribution, water content, etc.) for different types of soils.

By definition, the resilient modulus M_r is the secant modulus when the stress of the soil element transits from hydrostatic state ($\sigma_1 = \sigma_2 = \sigma_3$) to the maximum stress state ($\sigma_1 > \sigma_2 > \sigma_3$) while σ_3 remains unchanged. When performing a finite element/difference analysis on the resilient response of soil, tangent modulus must be used instead of secant modulus. In an axisymmetric problem, the maximum stress state can be re-written as $\sigma_1 > \sigma_2 = \sigma_3$. In this case the tangent resilient modulus E_t can be derived from Equation 2.16 (NCHRP 2004; Perkins 2004):

$$E_t = \frac{M_r}{1 - (\sigma_1 - \sigma_3) \left[\frac{k_2}{\theta} + \frac{\sqrt{2}k_3}{3(\tau_{oct} + p_a)} \right]} \quad 2.17$$

Compared to resilient modulus, Poisson's ratio ν of granular soils varies with stress in a relatively narrow range (from 0.2 to 0.4). Although some researchers (e.g., Hicks and Monismith 1971) proposed stress dependent models for Poisson's ratio, it was assumed as a constant in most studies (Lekarp et al. 2000a).

To study the permanent deformation behavior, some researchers performed cyclic triaxial tests (run to thousands or millions of load cycles) on granular soils. Empirical permanent deformation models can be developed by fitting the curve of permanent strain ε_{1p} (or the ratio of permanent strain to resilient strain

$\varepsilon_{1p}/\varepsilon_r$) against the number of cycle N . Literature reviews on the empirical models developed in the past were performed by Lekarp et al. (2000b) and Pérez et al. (2006). Some of the models are listed in Table 2.1.

Table 2.1 Empirical permanent deformation models (after Lekarp et al. 2000b; Pérez et al. 2006)

Equation		Reference	Parameters
$\varepsilon_{1p} = A + B \cdot \log N$	2.18	Barksdale 1972	A, B
$\varepsilon_{1p} = A \cdot N^B + C$	2.19	Paute 1988	A, B, C
$\frac{\varepsilon_{1p}}{\varepsilon_r} = \left(\frac{\varepsilon_0}{\varepsilon_r}\right) \cdot e^{-\left(\frac{\rho}{N}\right)^B}$	2.20	Tseng and Lytton 1989	ε_0, A, B
$\varepsilon_{1p} = A \cdot N^B$	2.21	Sweere 1990	A, B
$\varepsilon_{1p} = (m \cdot N + A)(1 - e^{-B \cdot N})$	2.22	Wolff and Visser 1994	A, B, m
$\varepsilon_{1p}^* = A \left[1 - \left(\frac{N}{100} \right)^B \right]$	2.23	Paute 1994	A, B

The permanent deformation model for granular base materials accepted in the current MEPDG was modified from Tseng and Lytton's model (Equation 2.20). A large amount of calibration work has been performed in the NCHRP Project 1-37a against the permanent deformation data collected from the Long Term Pavement Performance (LTPP) Program. Finally the calibrated form of permanent deformation model for granular materials is as follows:

$$\begin{aligned}
PD &= \beta_{s1} k_{s1} \varepsilon_v h_{soil} \left(\frac{\varepsilon_0}{\varepsilon_r} \right) \cdot e^{-\left(\frac{\rho}{N} \right)^\beta} \\
\left(\frac{\varepsilon_0}{\varepsilon_r} \right) &= \frac{0.15 \cdot e^{(\rho)^\beta} + 20 \cdot e^{\left(\frac{\rho}{10^9} \right)^\beta}}{2} \\
\log \beta &= -0.61119 - 0.017638 W_c \\
\rho &= 10^9 \left(\frac{-4.89285}{1 - (10^9)^\beta} \right)^{\frac{1}{\beta}}
\end{aligned} \tag{2.24}$$

where PD is the permanent or plastic deformation accumulated in the layer, N is the number of axle load applications, ε_v is the average vertical strain in the layer, k_{s1} is the global calibration coefficients ($k_{s1} = 1.673$ for granular materials and $k_{s1} = 1.35$ for fine-grained materials), and β_{s1} is the local calibration constant for the rutting in the unbound layers (by default $\beta_{s1} = 1.0$). It should be noted that the water content W_c is the only parameter needed in Equation 2.24, because it was calibrated by the best fit of all the data collected regardless of aggregate type, density, or stress level.

2.3 History of geocell

In late 1970s, U.S. Army Engineer Waterways Experiment Station performed a series of studies (Webster and Watkins 1977; Webster 1979a; Webster 1979b) to develop rapid and effective soil reinforcement techniques. Such techniques would help build roads quickly on unstable soils to support military vehicles.

Webster and Watkins (1977) built seven unpaved test road sections (one unreinforced control section and six sections with different types of reinforced base courses) on soft clay to compare different reinforcement techniques. By measuring the rut depth developed on the road after traffic loading, they found that one of the sections with a 30 cm (12 inch) thick sand (not a suitable material for base course) base course reinforced by cellular-confinement (made up of isolated plastic tubes of 15 cm (6 inch) diameter and 30 cm (12 inch) long) marginally outperformed the control section with a 36 cm (14 inch) thick crushed stone base course. After this study, a cellular confinement system, named “grid cell”, was soon developed, which is made up of square shaped grids and filled with sand. To assist design and application, both laboratory model test (Rea and Mitchell 1978) and full-scale road test (Webster 1979a; Webster 1979b) were performed to investigate a variety of factors that may influence the behavior of grid cell reinforced sand. The factors evaluated in these studies include grid size, grid shape, grid material, thickness of the sand-grid layer, subgrade stiffness, type of sand, compaction, load type, etc. These test data were later summarized and analyzed by Mitchell et al. (1979), who then proposed some useful analytical formulas to predict the capacity of the grid cell reinforced sand base course against different failure modes.

The grid cell used in Webster’s (1979b) test study was made of paper and aluminum. Both materials have some drawbacks since paper has a poor resistance to water and aluminum is relatively expensive. Webster (1979b)

further suggested that plastic might be a good material worth investigation. In 1980s, polymeric cellular confinement product was developed, and the general term “geocell” was first used to refer to this kind of products. Meanwhile, the benefit of using geocell reinforcement was widely demonstrated and studied in the U.S. as well as in Europe and Asia. Today geocell has been successfully used in various types of civil engineering projects as a quick and effective technique of soil reinforcement.

2.4 Geocell reinforced soil supporting static load

2.4.1 Experimental studies

The behavior of geocell-reinforced soil supporting static load has been studied mostly through laboratory model tests. The purposes of running these tests were (1) to demonstrate the benefit of using geocell by comparing reinforced cases with the unreinforced cases and (2) to investigate the effect of different parameters. Some of the previous experimental studies are summarized in Table 2.2. Most of these studies utilized similar setups (as illustrated in Figure 2.4). The major output from this test is the load-displacement curve. Other data such as displacement profile and the vertical earth pressure in the underlying soil were also measured in some studies.

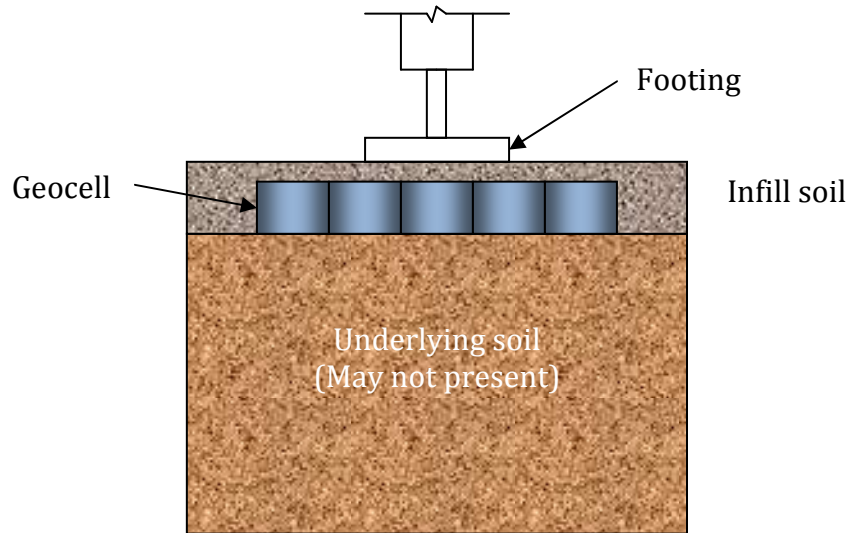


Figure 2.4 Typical test setup of the laboratory model test

Some of the common findings from the previous experimental studies are summarized below.

Benefit of using geocell

Most of the previous experimental studies demonstrated that the geocell can significantly increase the bearing capacity and the stiffness of the granular soil (sand and aggregate). For example, Mitchell et al.'s test study showed that the effective modulus of the geocell reinforced sand is about 2 to 3 times that of unreinforced sand (Mitchell et al. 1979). Dash et al. (2003) found that the bearing capacity of geocell reinforced sand could be up to seven times more than the bearing capacity of the unreinforced sand.

Effect of cell dimension

The influence of the dimension of the cell (or pocket) was studied usually by changing the cell width w and the cell height h . Generally, the bearing capacity increases with the cell height and decreases with the cell width. Rea and Mitchell (1978) found that the optimum cell height to cell width ratio (h/w) was around 2.25, beyond which the improvement was less significant. The optimum ratio of footing diameter D to cell width w suggested by Rea and Mitchell was about 1.5 to 2.0. Mitchell et al. (1979) performed some laboratory tests on geocell reinforced sand without underlying soft soil and found that the bearing capacity and the modulus of the geocell reinforced soil appeared to increase with the number of joints per unit area under the footing. Mitchell et al. (1979) also confirmed that the optimum cell height to cell width ratio (h/w) was in the order of 2 to 3.

Cover thickness

Thallak et al. (2007) tried placing geocell at different depths in his test. It was shown that the bearing capacity increased sharply when the geocell is placed at a shallower depth (less than 0.5 times circular footing width). However, from practical point of view, they suggested to put a thin layer of aggregate to protect the geocell from direct contact with the footing. Mitchell et al. (1979) suggested that an aggregate cover layer would not increase the bearing capacity or the modulus of the soil, but it would provide protection to the geocell.

Stiffness of geocell material

Previous studies indicated that geocell made of stiffer material will provide better improvement to the reinforced composite (Bathurst 1988; Pokharel et al. 2009b).

Table 2.2 Experimental studies reviewed on geocell reinforced soil supporting static load




Reference	Footing	Infill soil	Underlying soil	Geocell	Parameters studied
Rea and Mitchell 1978	Circular footing Diameter=51mm/ 77mm/ 102mm/ 128mm/ 153mm	Uniform fine quartz sand.	Rubber/ Sand	Material: Paper Pocket shape: 	Ratio of footing diameter to cell width; Ratio of cell width to cell height; Subgrade stiffness.
Mitchell et al. 1979	Circular footing Diameter=32mm/ 51mm/ 77mm/ 128mm/ 153mm	Uniform fine quartz sand	--	Material: Paper Pocket shape: 	Ratio of footing diameter to cell height; Ratio of cell width to cell height;
De Garidel and Morel 1986	Circular footing Diameter=300mm	Fine sand	Natural silt	Material: Bonded non- woven geotextile Pocket shape: 	Geocell material; Side length of the cell; Height of the cell.

Table 2.2 Experimental studies reviewed on geocell reinforced soil supporting static load (continued)







Reference	Footing	Infill soil	Underlying soil	Geocell	Parameters studied
Bathurst 1988	Strip footing Length=205mm Width=73mm	Good quality crushed limestone aggregate	Finely fibrous horticultural sphagnum peat	Material: polyethylene/ Bounded geogrid Pocket shape: 	Geocell material; Base thickness.
Mandal and Gupta 1994	Strip footing Length=205mm Width=73mm	Sand	Reconstituted soft marine clay	Material: Bonded non-woven geotextile Pocket shape: 	Ratio of cell height to footing width; Side length of the cell.
Adams and Collin 1997	Square footing Width= 30mm/ 46mm/ 61mm/ 91mm	Poorly graded sand	Same as the infill soil	Material: high-density polyethylene Pocket shape: n/a	Load area.
Dash et al. 2003	Circular footing Diameter=150mm	Poorly graded sand	Low plasticity silty clay	Material: Bounded geogrid Pocket shape: 	Ratio of cell height to cell width; With or without geogrid placed below the geocell.

Table 2.2 Experimental studies reviewed on geocell reinforced soil supporting static load (continued)

Reference	Footing	Infill soil	Underlying soil	Geocell	Parameters studied
Dash et al. 2004	Strip footing Length=330mm Width=100mm	Poorly graded sand	Same as the infill soil	Material: bounded geogrid Pocket shape: 	Pocket shape; With or without geogrid placed below the geocell.
Thallak et al. 2007	Circular footing Diameter=150mm	Low plasticity silty clay	Same as the infill material	Material: Bonded geogrid Pocket shape: 	Cover thickness; Height of the cell; Width of the cell; Width of the geocell mattress.
Pokharel et al. 2009b	Circular footing Diameter=152mm	Poorly graded sand	--	Material: HDPE/ Novel polymeric alloy Pocket shape: 	Stiffness and strength of geocell material; Pocket shape.

2.4.2 Analytical and numerical studies

The first analytical work conducted on the geocell reinforced soil was performed by Mitchell et al. (1979), who identified seven possible failure modes when geocell reinforced sand overlying soft subgrade was subjected to a static vertical load on the ground surface. The seven possible failure modes are respectively (1) cell penetration of the subgrade, (2) cell bursting, (3) cell wall buckling, (4) bearing capacity, (5) bending, (6) durability failure, and (7) excessive rutting. Although Mitchell and his colleagues did not address all the failure modes with analytical solution, their study provided valuable understandings about the problem to the later researchers. For example, they first noticed the difficulties in estimating the modulus of the geocell reinforcement layer because of “the stress-dependent nature of the sand stiffness and the three-dimensionality of the grid cell network” (Mitchell et al. 1979).

Bathurst and Karpurapu (1993) performed triaxial compression tests on a single cell-reinforced granular soil sample. By analyzing the Mohr circles and the Mohr-Coulomb failure envelopes of the unreinforced and reinforced samples, they proposed using the apparent cohesion c_r to account for the strength increase of the geocell. The apparent cohesion c_r was resulted by the increased confining stress $\Delta\sigma_3$ provided by the geocell onto the infill soil (Equation 2.25):

$$c_r = \frac{\Delta\sigma_3}{2} \tan\left(\frac{\pi}{4} + \frac{\phi}{2}\right) \quad 2.25$$

In Equation 2.25, ϕ is the friction angle of the soil; the increased stress $\Delta\sigma_3$, as suggested by Bathurst and Karpurapu (1993), can be estimated by the following equation:

$$\Delta\sigma_3 = \frac{2M}{d} \left[\frac{1 - \sqrt{1 - \varepsilon_a}}{1 - \varepsilon_a} \right] \quad 2.26$$

where M is the tensile stiffness of the geocell material; d is the initial diameter of the geocell pocket; and ε_a is the axial strain for the soil. Equation 2.26 was originally developed by Henkel and Gilbert (1952) for estimating the membrane's effect on the triaxial test sample. When deriving this equation, it is assumed that (1) the volume of the soil sample was constant and (2) the deformed sample was still a right cylinder. Based on Equation 2.25 and 2.26, Madhavi Latha et al. (2006) developed a design method for the geocell reinforcement supporting embankment.

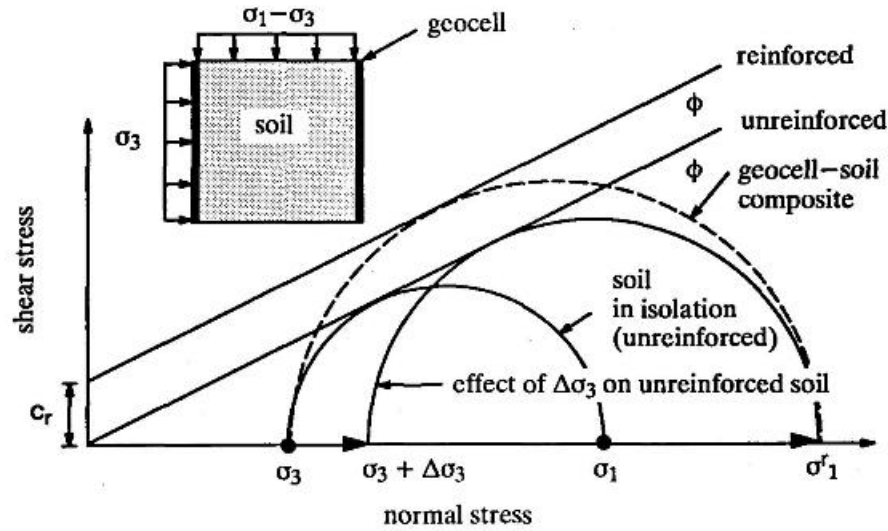


Figure 2.5 Mohr circle construction for calculating the apparent cohesion of the geocell-soil composite (Bathurst and Karpurapu 1993)

Rajagopal (1999) also performed triaxial tests on single-cell and multi-cell reinforced sand samples (see Figure 2.6). His test data confirmed that the geocell reinforced sample has a friction angle almost the same as the reinforced soil, but with an increased cohesion (as shown in Figure 2.7). Based on his test results, Rajagopal (1999) suggested that reinforced samples with at least three interconnected cells should be used in the triaxial test in order to accurately estimate the apparent cohesion.

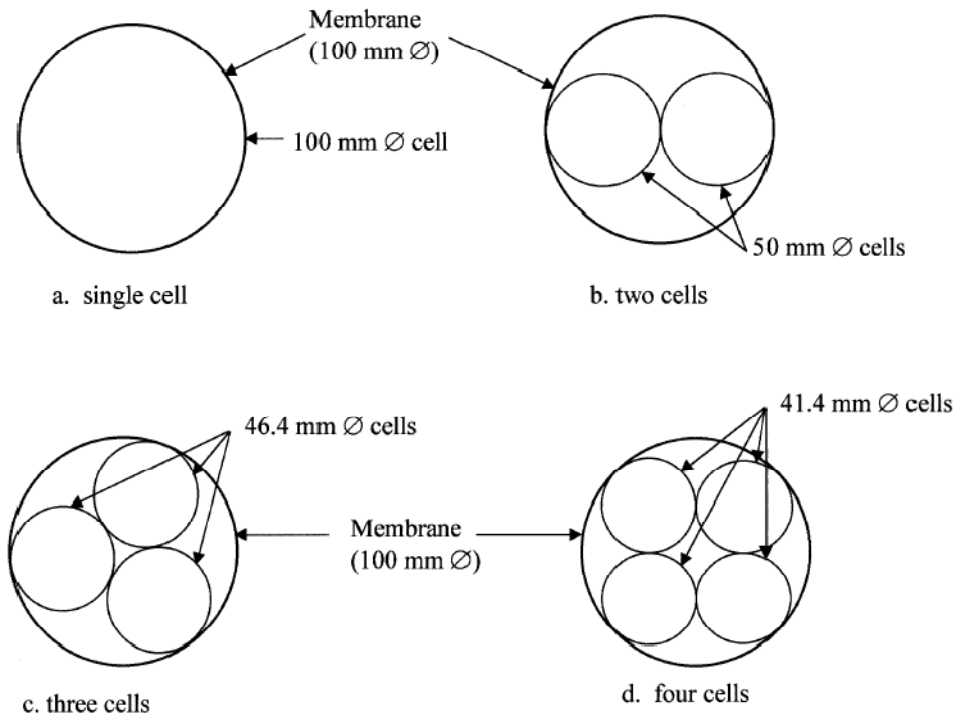


Figure 2.6 Configuration of single-cell and multi-cell reinforced soil sample for triaxial tests (Rajagopal et al. 1999)

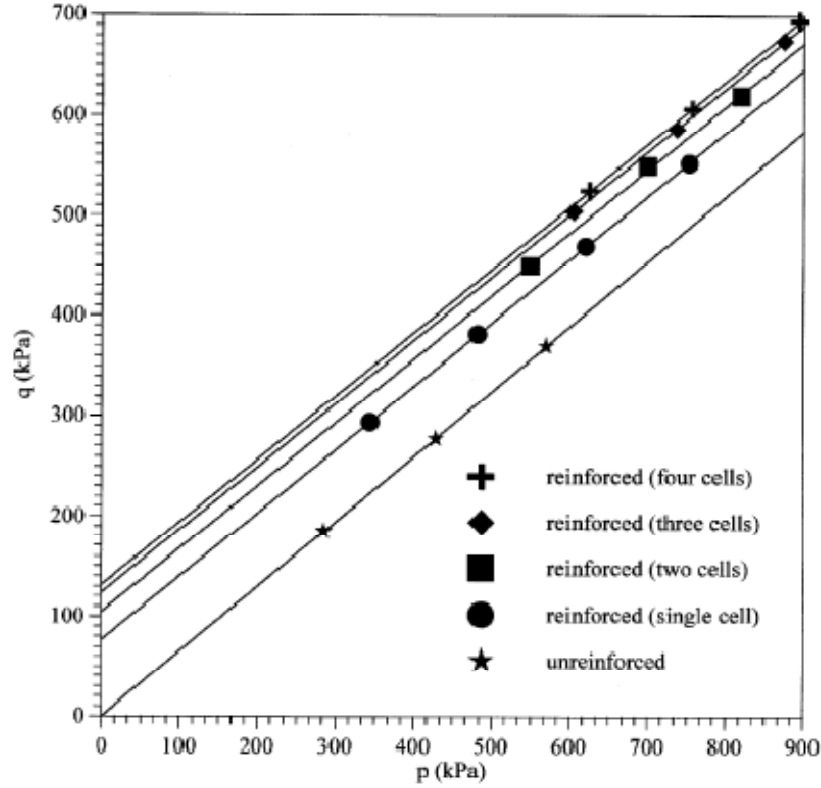


Figure 2.7 Failure envelopes with different configurations of geocell in p - q space ($p=(\sigma_1+\sigma_3)/2$, $q=(\sigma_1-\sigma_3)/2$) (Rajagopal et al. 1999)

Wesseloo (2004) performed unconfined compression tests on single-cell and multi-cell (2×2 , 3×3 , and 7×7) reinforced soil. For the particular materials used in his study, he developed an elastoplastic constitutive model for the infill soil and rate-dependent non-linearly elastic membrane models for the geocell. Based on his model, Wesseloo (2004) analyzed the stress-strain behavior of the single cell-reinforced sand based on his model. He also raised the problem that the stress-strain behavior measured from single cell-reinforced soil could not represent that of multi-cell reinforced soil. He proposed introducing an efficiency factor f_{eff} (≤ 1) to account for the multi-cell effect:

$$f_{eff} = \frac{\sigma_{a \text{ single-cell}}}{\sigma_{a \text{ multi-cell}}} \quad 2.27$$

where $\sigma_{a \text{ single-cell}}$ is the axial stress in a single cell structure at a specified diameter and axial strain rate, and $\sigma_{a \text{ multi-cell}}$ is the axial stress in a multi-cell structure at the same specified cell diameter and axial strain rate. The efficiency factor should be determined from unconfined compression tests.

The increased stiffness of geocell-reinforced soil was studied by Madhavi Latha (2000), who proposed an empirical equation to estimate the modulus number K_r of the geocell-soil composite from the modulus number K_e of the unreinforced soil:

$$K_r = K_e + 200M^{0.16} \quad 2.28$$

where K_r and K_e corresponds to the modulus number K in the Duncan-Chang model (Equation 2.8); M has the same meaning as that in Equation 2.26.

A number of numerical studies were reviewed and summarized in Table 2.3. Among the publications reviewed, the Duncan-Chang model has been frequently used to simulate the stress-dependency of the granular soils. Some researchers (Mhaikar and Mandal 1996; Bathurst and Knight 1998; Madhavi Latha and Rajagopal 2007; Madhavi Latha et al. 2008; Madhavi Latha and Somwanshi 2009) modeled geocell-reinforced soil as a composite material with the

equivalent parameters determined by Equations 2.25, 2.26, and 2.28. Such simplification is helpful when analyzing a three-dimensional problem using two-dimensional numerical software. However, the equivalent model can not accurately simulate the interaction between the infill soil and the geocell. One problem with this method is that the axial strain ε_a of the geocell-reinforced soil at failure has to be first estimated in order to calculate apparent cohesion c_r from Equations 2.25 and 2.26. In the reality, the value of ε_a may vary from cell to cell, especially when the geocell reinforcement is supporting load in a limited area (such as from a circular footing). As Mitchell et al. (1979) pointed out, the confining stress in the cells beneath the loading area is much larger than that in the cells outside the loading area, which means the apparent cohesion and the modulus of the reinforced soil under the loading area should be larger than that outside the loading area.

Han et al. (2008) probably was the first to model soil and geocell separately in a three-dimensional numerical model. They performed a laboratory model test on unreinforced and single cell-reinforced sand supporting a rectangular footing. In the numerical model created by FLAC^{3D}, they used the Mohr-Coulomb model for the sand and linearly elastic membrane model for the geocell. It was found that benefit of geocell on the bearing capacity shown in the test cannot be simulated using this model because Mohr-Coulomb model ignored the stress-dependency of soil. In order to match the test result, modulus of the soil inside the geocell has to be increased about 1.9 times.

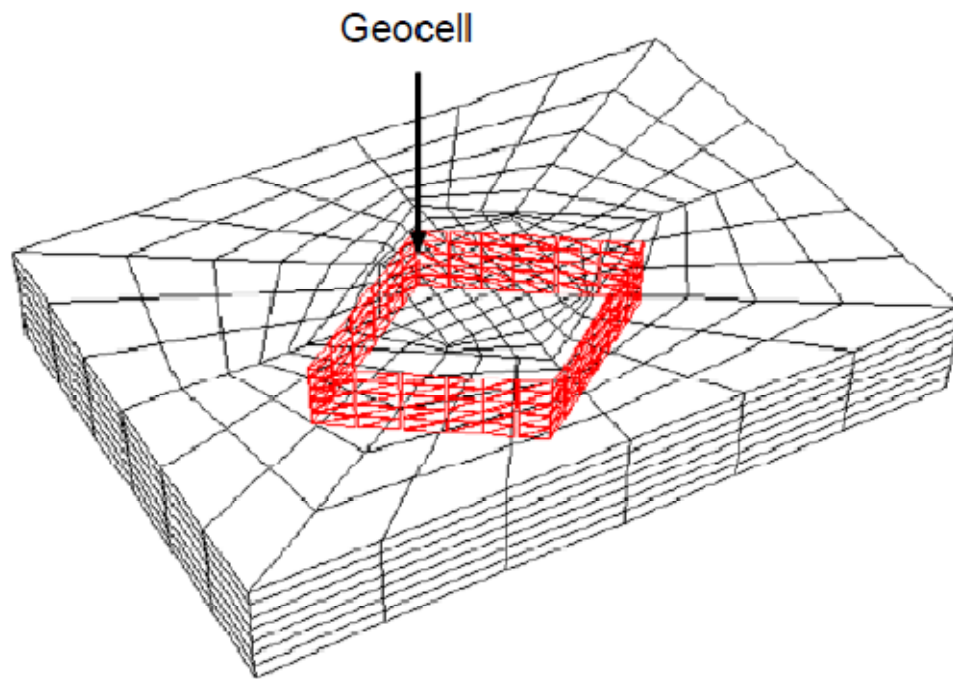


Figure 2.8 Three-dimensional model of single cell-reinforced soil (Han et al. 2008)

Table 2.3 Numerical modeling studies reviewed on geocell reinforced soil supporting static load

Reference	Model	Program/ (2D or 3D)	Infill soil model	Geocell model
Evan 1994	Geocell reinforced sand on top of soft subgrade supporting an embankment load	SSTIPG/ 2-Dimensional	Duncan-Chang model	Equivalent Linearly elastic planar reinforcement
Mhaikar and Mandal 1996	Geocell reinforced sand on top of clay subgrade supporting a rectangular footing	ANSYS/ 3-Dimensional	Geocell reinforced soil was modeled as a composite material using Drucker-Prager model	
Bathurst and Knight 1998	Geocell reinforced sand over a steel conduit	GEOFEM/ 2-Dimensional	Geocell reinforced soil was modeled as a composite material using Duncan-Chang model	
Madhavi Latha and Rajagopal 2007	Geocell reinforced sand on top of clay subgrade supporting an embankment load	GEOFEM/ 2-Dimensional	Geocell reinforced soil was modeled as a composite material using Mohr-Coulomb model	
Han et al. 2008	Single cell-reinforced sand supporting rectangular footing	FLAC ^{3D} / 3-Dimensional	Mohr-Coulomb model	Linearly elastic membrane
Madhavi Latha et al. 2008	Geocell reinforced sand supporting a strip footing	GEOFEM/ 2-Dimensional	Geocell reinforced soil was modeled as a composite material using Duncan-Chang model	
Madhavi Latha et al. 2009	Geocell reinforced sand supporting a strip footing	GEOFEM/ 2-Dimensional	Geocell reinforced soil was modeled as a composite material using Duncan-Chang model	
Madhavi Latha and Somwanshi 2009	Geocell reinforced sand supporting a square footing	FLAC ^{3D} / 3-Dimensional	Geocell reinforced soil was modeled as a composite material using Duncan-Chang model	

2.5 Geocell reinforced soil supporting repeated load

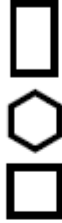


2.5.1 Experimental studies

The concept of cellular confinement was first tested out in full-scale road test in 1970s by the U.S. Army Engineer Waterways Experiment Station (Webster 1979a; Webster 1979b). A total of four road sections with 18 sand-grid (the early form of geocell) test items were constructed. Traffic load was applied by driving a 5-ton (49 kN) military truck (with 70 psi (483 kPa) tire pressure) on the road sections back and forward. Factors investigated included grid shape, grid size, grid material, with or without asphalt surface, and compaction effort. These tests yielded some important findings:

- (1) Sand-grid material type, cell size, thickness, sand type and cover are all related to the traffic performance of the reinforced road.
- (2) Square shaped and hexagonal shaped grids performed better than rectangular grids. Performance of the sand-grid layer decreases as the cell area increases.
- (3) The grid should be expanded and placed along the traffic direction for best performance.
- (4) Adequate cover must be placed over the grid cells.
- (5) Sand type becomes more influential to the road performance as the grid size increasing and also as the grid thickness decreasing.

Surprisingly few studies (listed in Table 2.4) were documented on testing geocell reinforced soil under repeated load after Webster's study, probably due to the complexity and cost of such tests. Sekine et al. (1994) constructed a 3.5 m long, 7 m wide railroad section to investigate the geocell reinforced railroad base. Repeated load of 90 kN at 11 Hz frequency was applied on the rails. Crushed stone was used as the infill material. During construction of the road section, Sekine et al. (1994) found that with the same compaction effort, the density of the geocell-reinforced base was lower than that of the unreinforced base. The compaction issue seemed to influence the performance of the base because one of the reinforced sections rutted more than the unreinforced control section. Overall, Sekine et al. (1994) found the geocell was effective in reducing the deformation of the road bed when the bearing capacity subgrade was low. Mhaikar and Mandal (1994) also demonstrated the benefit of using geocell in reducing the permanent deformation of pavements under a repeated load. Instead of constructing a road section, they conducted the repeated load test inside a test box. The test results showed that geocell-reinforced base performed distinctly better than the geotextile reinforced base and the unreinforced base.

Table 2.4 Experimental studies reviewed on geocell-reinforced soil supporting repeated loads

Reference	Repeated Load	Infill soil	Underlying soil	Geocell	Parameters studied
Webster 1979a; Webster 1979b	5-ton (49 kN) M51 tandem axle military truck With 70psi (483kPa) tire pressure	Poorly graded sand	Same as the infill soil	Material: Paper/ Aluminum Pocket shape: 	Grid shape; Grid size; Grid material; With or without asphalt surface; Compaction effort.
Sekine et al. 1994	Sine wave Maximum 90kN Minimum 10kN 11Hz Applied on the rails (3.5m long)	Crushed stone	Sand	Material: HDPE Pocket shape: 	Compaction effort; Subgrade stiffness.
Mhaiskar and Mandal 1994	Rectangular footing Length=350mm Width=250mm Maximum 4kN Minimum 0 5 cycle/minute	Sand	Soft clay	Material: Bonded woven geotextile Pocket shape: Unknown	With or without geocell.
Pokharel et al. 2009a	Circular footing Diameter=150mm Maximum 345kPa Minimum 0 1 cycle/minute	Poorly graded sand	--	Material: Novel polymeric alloy Pocket shape: 	--

2.5.2 Analytical and numerical studies

Although geocell has been proved to be efficient in reducing the permanent deformation in pavements, limited effort was made to develop a design method for geocell reinforcement. The recommended configuration (cell size, thickness, etc.) of geocell-reinforced bases provided by a test study cannot be simply applied to another situation with different soil type or different geocell product. A rational design model is in great need to predict the pavement response (such as resilient modulus and permanent deformation) with consideration of geocell reinforcement.

The only pavement design method for geocell-reinforced road bases was proposed by Mengelt et al. (2000), who performed laboratory resilient modulus tests on unreinforced and single-geocell-reinforced soils. Both cohesive and granular soils were used as the infill material. A special chamber was made for the single-geocell-reinforced sample (see Figure 2.9) because the diameter of such a sample (25cm) was larger than the standard diameter (15cm) of the sample for the test equipment. Test results showed that the resilient modulus of the geocell-reinforced granular soil was slightly (1.4% to 3.2%) larger than that of the unreinforced granular soil, whereas the resilient modulus of the geocell-reinforced fine-grained soil increased 16.5% to 17.9% as compared with that of the unreinforced soil. As for permanent deformation, the permanent deformation was reduced by 50% for the aggregate sample and 44% for the

sand sample when geocell reinforcement was included. Mengelt et al. (2000) also proposed a method to incorporate these findings into the flexible pavement design method (Huang 1993).



Figure 2.9 Single-geocell-reinforced aggregate sample for resilient modulus test (Mengelt et al. 2000)

No published literature was found on numerical modeling of geocell-reinforced soil supporting repeated loads. Some researchers (Perkins 2004; Kwon et al. 2009) modeled geogrid-reinforced aggregate road bases based on the framework of the mechanistic-empirical model. Although the reinforcement mechanism of geogrid and geocell are quite different, these numerical models provided valuable understandings on the problem, which is helpful for this study. For example, Perkins (2004) and Kwon et al. (2009) both emphasized the

importance of considering the residual horizontal stress within the base course induced by compaction. In Perkins' model, an isolated compaction model was run first to calculate the residual stress induced by compaction. The residual stress was estimated indirectly by shrink the geocell by 1% strain horizontally. And then two traffic models (Traffic I and II) are used to calculate the residual stress in the base after a certain number of wheel passes. Finally, the residual stress obtained from the traffic models is assigned as the initial stress to the response model (Traffic III) for calculating the resilient response of the pavement. Perkins (2004) also developed a permanent deformation model for geogrid-reinforced soil, which must be calibrated by performing cyclic triaxial tests on geogrid-reinforced soil samples. Kwon et al. (2009) directly assigned a 41 kPa initial horizontal stress to the base within 102mm above the geogrid to consider the compaction effect. They used an anisotropic resilient modulus model for the aggregate base to account for the different behavior of soil under cyclic axial stress and cyclic confining stress. Due to the planar geometry of geogrid, Perkins (2004) and Kwon et al. (2009) both used two-dimensional (axisymmetric) models.

2.6 Summary

This chapter reviewed in constitutive model theories, history of geocell, as well as the experimental, analytical and numerical studies conducted on geocell reinforcement supporting static and repeated load. These studies provided

valuable understandings and experiences on the target problem of the current study. Based on the literature review, several conclusions can be drawn:

- (1) Geocell-reinforced granular soil is generally both stiffer and stronger than the unreinforced granular soil under a static load. The modulus and the shear strength of the geocell-soil composite depends on a number of factors such as infill soil properties, loading area, materials of the geocell, and geometry of the geocell. Generally, for a particular infill soil and loading condition, the modulus and the shear strength of the geocell-soil composite will increase with the cell height to cell width ratio (h/w).
- (2) The increased modulus and shear strength of the geocell-soil composite is caused by the stress-dependency of the soil and the additional confining stress provided by the geocell. To simulate the interaction between soil and geocell, a stress-dependent model (e.g., the Duncan-Chang model) for soil must be used. In the past, geocell and soil were often modeled as homogeneous isotropic composite materials with some equivalent properties. Such simplifications cannot accurately simulate the interaction between soil and geocell, especially when the load is applied in a limited area.
- (3) Geocell product was originally developed for reinforcing roadway bases. Full-scale road tests have proved the efficiency of geocell in reducing the permanent deformation of soil under a repeated load, especially when used with sand. Some valuable conclusions and recommendations in

using geocell reinforced bases are documented. However a rational design method is in great need.

(4) Numerical modeling of permanent deformation of soil under repeated loading using an elasto-plastic model is difficult and extremely time-consuming. The mechanistic-empirical model has been successfully used in analyzing flexible pavements with geogrid-reinforced bases. This model may be used to analyze the geocell-reinforced bases. However, issues such as the residual stress in the geocell-reinforced base need to be considered.

(5) Triaxial and resilient modulus tests have been performed on single cell-reinforced granular soil samples. Triaxial test results showed that the increased shear strength of the geocell-reinforced soil can be simply represented by apparent cohesion c_r . From resilient modulus tests, it was found that geocell did not significantly increase the resilient modulus of granular soil, but significantly reduced the potential of permanent deformation. However, it was also noticed by some researchers that these findings drawn from single cell-reinforced soil cannot be applied to multi-cell-reinforced soil directly. Multi-cell interaction effect should be considered.

Chapter 3 Laboratory model tests

3.1 Overview

Two sets of laboratory model tests were performed in this study: (1) static load tests on geocell-reinforced sand and (2) moving-wheel tests on unpaved road sections with geocell-reinforced bases. These two sets of model tests, as well as the laboratory tests for determining the material index properties, are introduced in the following two sections (Sections 3.2 and 3.3). The purpose of running these tests is to validate and calibrate the numerical models created in this study.

Totally four types of geocell were tested in the laboratory model tests. Type I geocell was made from high density polyethylene (HDPE). Types II, III and IV geocells were made from novel polymeric alloy (NPA). The novel polymeric alloy is characterized by flexibility at low temperatures similar to HDPE with an elastic behavior similar to engineering thermoplastic. The geocells used in the experiments were manufactured and provided by PRS Mediterranean, Inc. in Israel.

3.2 Static Load tests

Static load tests were performed to determine the load-settlement behavior of geocell reinforced soil under a static load. A poorly-graded dry sand was used as the infill material. Three types of geocell (Type I (HDPE), Type II (NPA), and Type III (NPA)) were tested. These geocell products were with different tensile stiffness and strength but with the same geometry (pocket size and height).

3.2.1 Test setup and procedure

Since the main purpose of running these tests is to validate and calibrate the numerical model, a simple test setup (with only one cell) was adopted (see Figure 3.1). The test was conducted in a test box of 80 cm long, 80 cm wide and 60 cm high. The vertical load was applied by an air pressure chamber. To minimize the friction between sand and the box (so that a smooth bottom boundary condition can be used in the numerical model), a thin stainless steel sheet was placed at the bottom of the box.

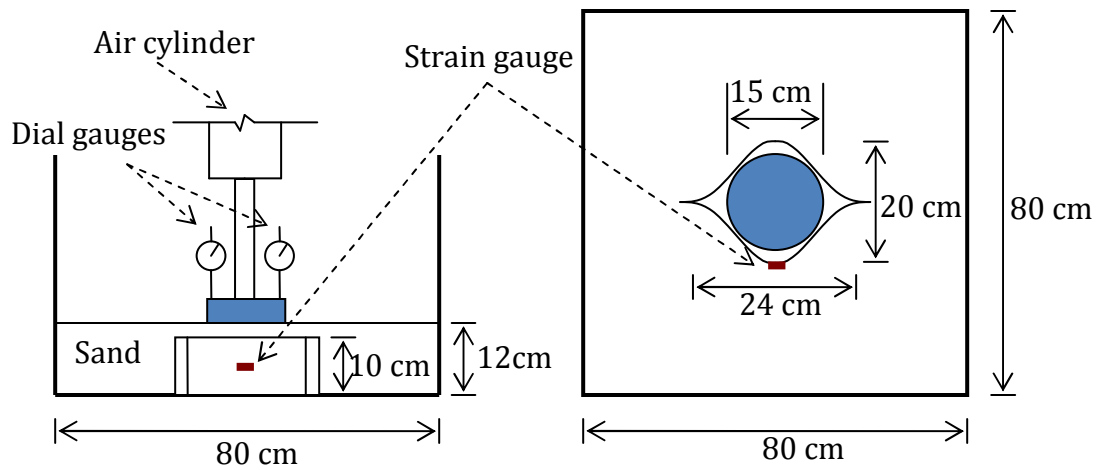


Figure 3.1 Static load test setup

A strain gauge was attached at the mid-depth of the outside surface of each geocell (see Figure 3.2). The strain gauge can measure up to 3% tensile strain. The geocell was placed at room temperature for more than 24 hours to allow the protection coating on the strain gauge to cure. After that, the geocell was placed at the center of the bottom of the box. To ensure the same pocket size of geocell in each test, a 20 cm long wood stick was used to expand the geocell (Figure 3.3). Sand was poured into the box and compacted in three layers (5 cm, 5 cm and 2 cm) to a total thickness of 12 cm. The soil in each sub-layer was weighed before being placed to ensure a uniform relative density of 70% after compaction. The stick was taken out before the second 5 cm sand was compacted.

A circular steel plate with a diameter of 15 cm was placed at the center of the top surface of the sand. The displacement of the plate was measured by two dial

gauges. The vertical load was applied in steps by adjusting the air pressure in the air cylinder. Each load step was maintained (typically two to five minutes) until the plate displacement became stable. Meanwhile, the strain gauge data was recorded with a data acquisition system during the test. The test was conducted up to the failure of the soil. For comparison purpose, a load test on unreinforced sand with the same thickness was also conducted.

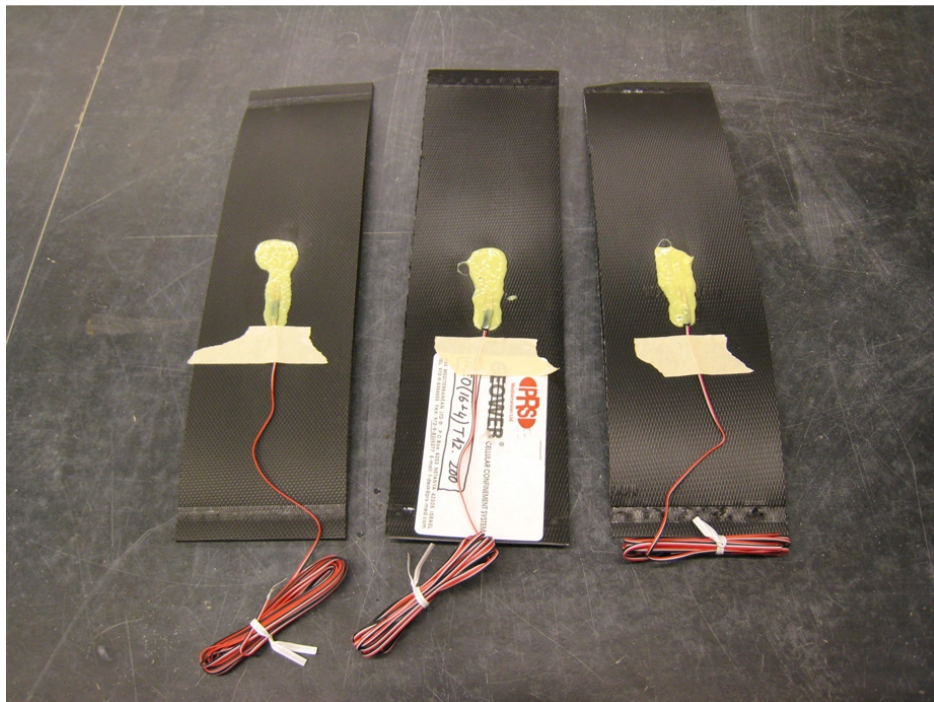


Figure 3.2 Installation of strain gauge on the geocell

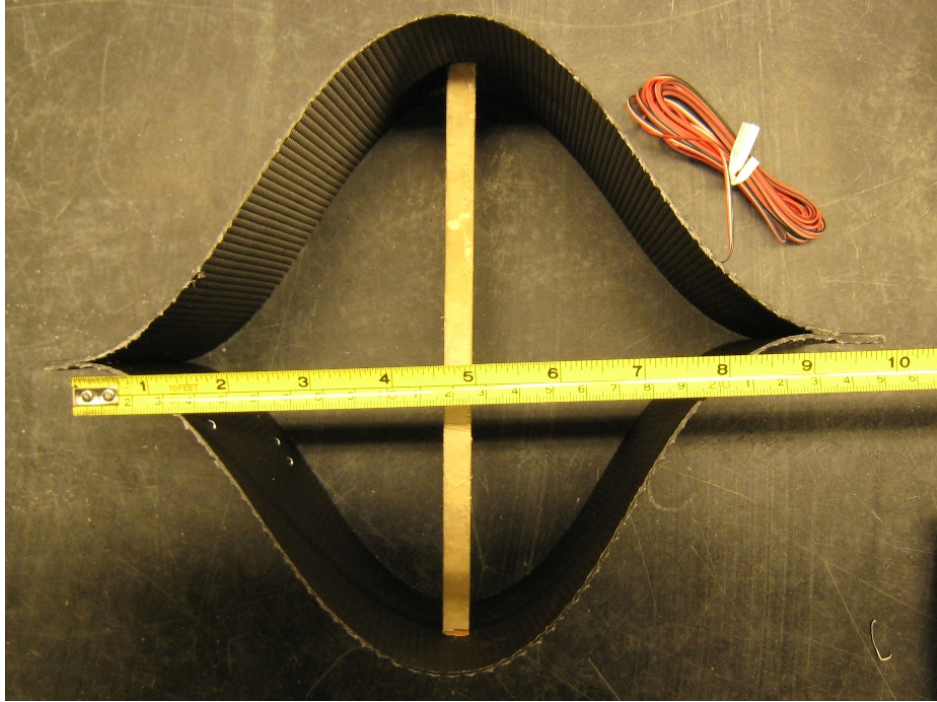


Figure 3.3 Pocket size of geocell (before fill)

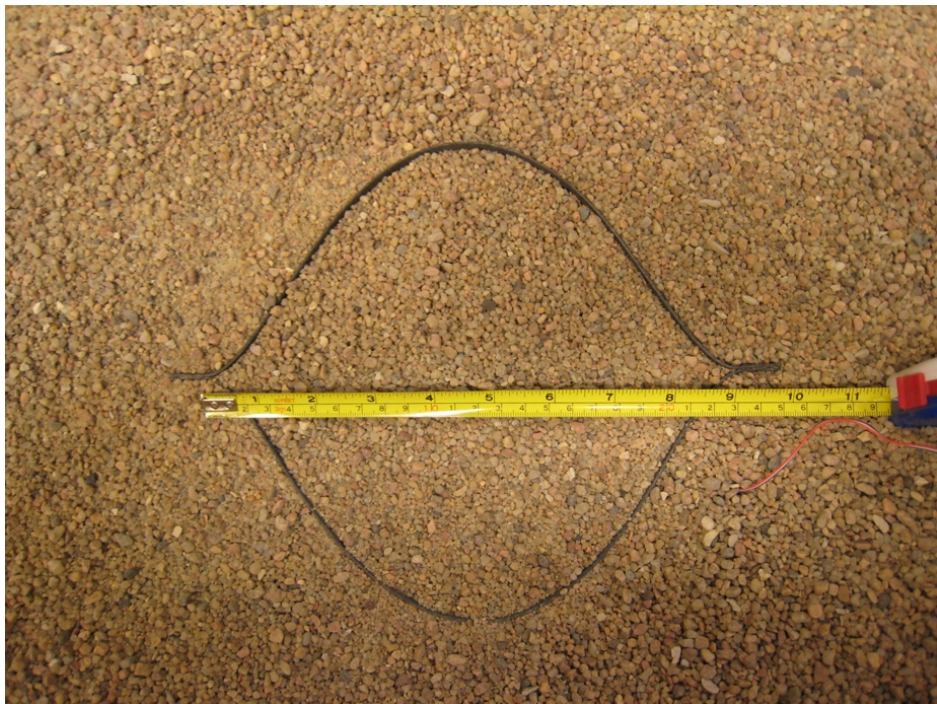


Figure 3.4 Pocket size of geocell (after fill and compaction)



Figure 3.5 Load plate and dial gauge setup

3.2.2 Material used

3.2.2.1 Sand

A poorly-graded dry sand was used in this test. The sand was obtained by sieving out the particle finer than 0.15mm from a local river sand (named Kansas River sand). The grain size distribution of this sand is shown in Figure 3.6. Some properties of sand are: $G_s = 2.65$, $C_c = 0.98$, $C_u = 2.73$, $\gamma_{min} = 16.4 \text{ kN/m}^3$, and $\gamma_{max} = 19.5 \text{ kN/m}^3$.

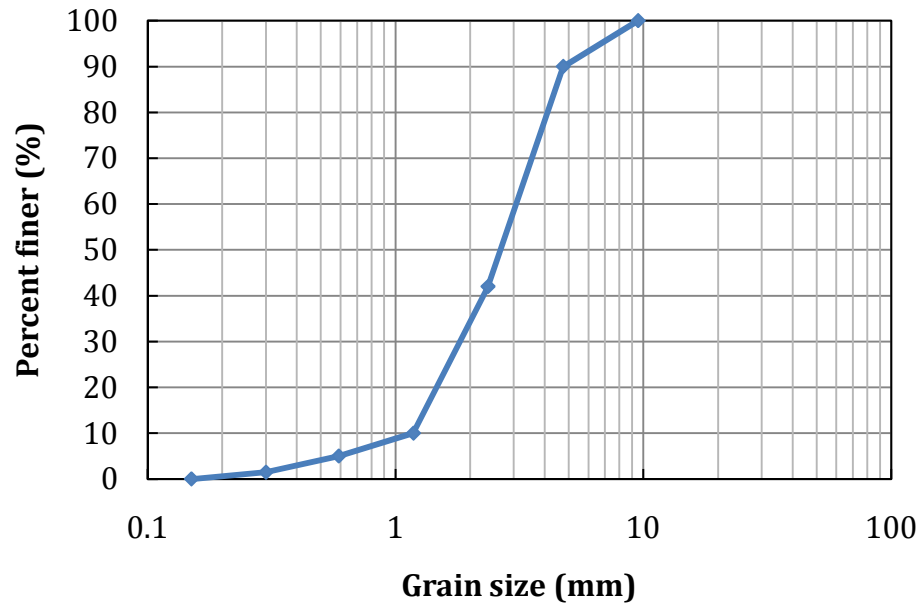


Figure 3.6 Grain size distribution of the sand

Three triaxial compression (CD) tests and one isotropic compression test were conducted on the sand samples prepared at 70% relative density. The triaxial compression tests were conducted at confining stresses of 68.9kPa (10psi), 103.4kPa (15psi), and 137.9kPa (20psi). The deviatoric stress was applied at a constant strain rate of 0.1%/min. The triaxial compression test data are plotted in Figure 3.7.

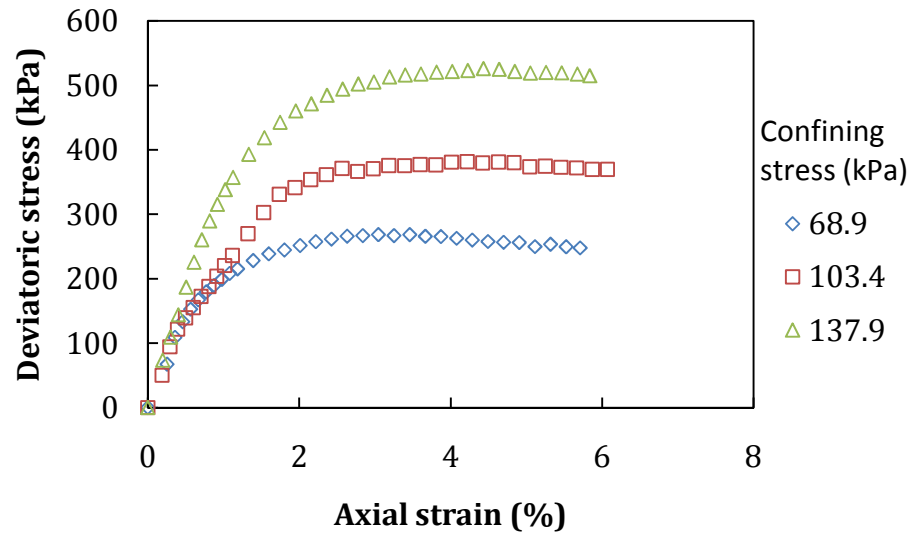


Figure 3.7 Triaxial compression test result

An isotropic compression test was conducted to determine the bulk modulus parameters of the sand. Sample preparation for this test was the same as that for triaxial compression tests. In this test, the same water pressure was initially applied inside and outside the saturated sand sample. Then the water pressure outside the sample was increased by an increment of 13.8kPa (2psi). Each stress increment was maintained until the volume of the sample became stable. The isotropic compression test data are plotted in Figure 3.8.

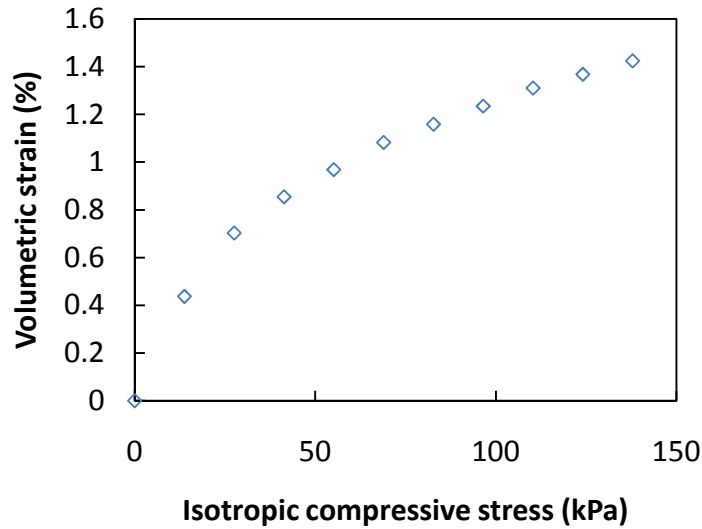


Figure 3.8 Isotropic compression test result

3.2.2.2 Geocell

Three types of geocell (Type I, Type II, and Type III) were used in the static load tests. Type I geocell was a HDPE geocell. Type II and Type III geocells were NPA geocells. The stress-strain characteristics of these geocell materials under uniaxial tension were shown in Figure 3.9 and Table 3.1. It is shown that the elastic modulus E (at 1% strain) of the three geocell material increases from Type I to Type III (i.e., $E_{III} > E_{II} > E_I$). However, since the thickness of the Type I material is larger than Type II and Type III materials, the tensile stiffness M (taking account of the thickness of the geocell strip) of Type I geocell strip lies between the Type II and Type III geocell strips ($M_{III} > M_I > M_{II}$). Table 3.2 shows the creep resistance properties of the HDPE and the NPA (Type IV) materials. Type IV NPA geocell was used in this study in the moving wheel tests,

which is described later in this chapter. It is shown in Table 3.2 that the NPA material has a better creep resistance behavior than the HDPE material. Some other properties of the NPA material provided by the manufacturer are presented in Table 3.3.

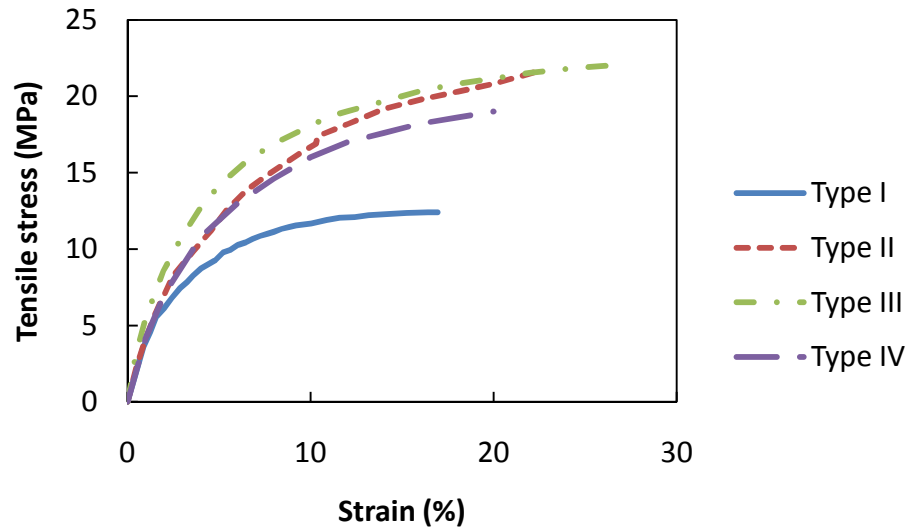


Figure 3.9 Stress-strain behavior of the geocell materials

Table 3.1 Stress-strain behavior of the geocell materials

Geocell	Thickness t (mm)	Tensile strength (MPa)	Elastic modulus E at 1% strain (MPa)	Tensile stiffness M at 1% strain ($M = E \cdot t$) (kN/m)
Type I (HDPE)	1.5	12.4	392	588
Type II (NPA)	1.1	21.6	418	460
Type III (NPA)	1.1	22.0	550	605
Type IV (NPA)	1.1	19.0	420	462

Table 3.2 Creep resistance properties of the HDPE and the NPA materials (from PRS Mediterranean, Inc.)

Stress to create 10% strain at 23°C for (Years)	HDPE (N/mm)	NPA (N/mm)
25	3.41	5.82
50	3.33	5.65
75	3.27	5.56

Table 3.3 Other properties of the NPA material (from PRS Mediterranean, Inc.)

Properties	Description	Unit	Test method
Tensile strength	>20	N/mm	PRS method
Allowed strength for design of 50 years	>5.7	N/mm	ASTM D6992
Creep reduction factor	<3.5		ASTM D6992
Coefficient of thermal expansion (CTE)	≤80	ppm/°C	ISO 11359-2 ASTM E831
Flexural Storage Modulus at	30°C >750	MPa	ISO 6721-1 ASTM E2254
	45°C >650		
	60°C >550		
	80°C >300		
Oxidative Induction Time (OIT)	≥100	minutes	ISO 11375-6 ASTM D3895 (OIT @ 200°C, 35kPa)
Durability to UV Degradation	>400	minutes	ASTM D5885 (HPOIT @ 150°C, 3500kPa)

3.2.3 Test results and discussion

The load-displacement curves obtained from the static load tests are plotted in Figure 3.10. The results clearly showed that geocell reinforcement increased the bearing capacity of the sand. At 5mm displacement (where the soil started to

“yield”), the bearing capacity of unreinforced sand was 102kPa, whereas the bearing capacities of different geocell reinforced sand were 147kPa (Type I HDPE geocell), 138kPa (Type II NPA geocell), and 150kPa (Type III NPA geocell) respectively. From the test results, it seems that the tensile strength of the geocell material has no significant effect on the bearing capacity improvement.

The test result also showed that the slopes of the load-displacement curves for reinforced and unreinforced cases were initially close to each other. The curves started to separate when the displacement reached 2mm. In another word, geocell reinforcement needs some displacement to take effect. The reason for this phenomenon may be that the hoop stress from the geocell is proportional to the tensile stress of geocell. So the geocell provides more and more confining stress to sand as the tensile stress (or strain) in the geocell increases.

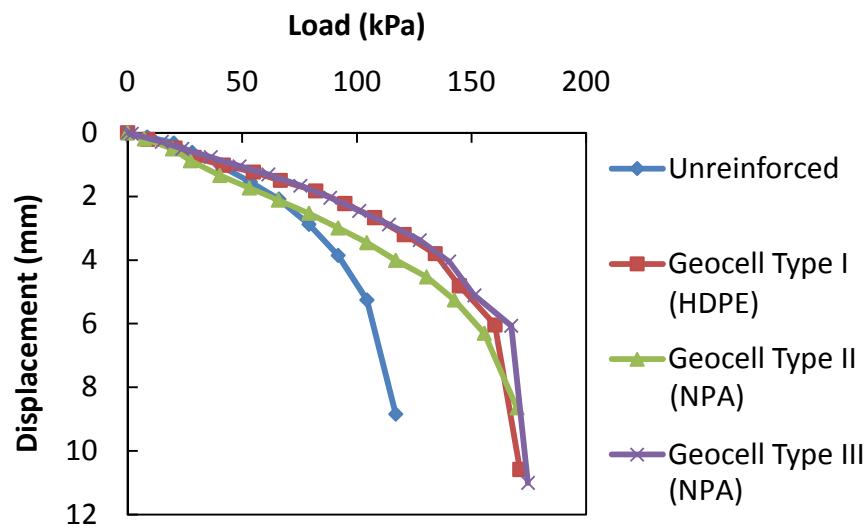


Figure 3.10 Load vs. displacement

The tensile strains of the geocell measured by the strain gauges were plotted against the vertical load in Figure 3.11. Overall, the tensile strains of the geocell increased non-linearly with the applied vertical load, which means the geocell took more and more load as the soil approaching its shear strength. The maximum tensile strain (0.6%) was measured in Type I geocell.

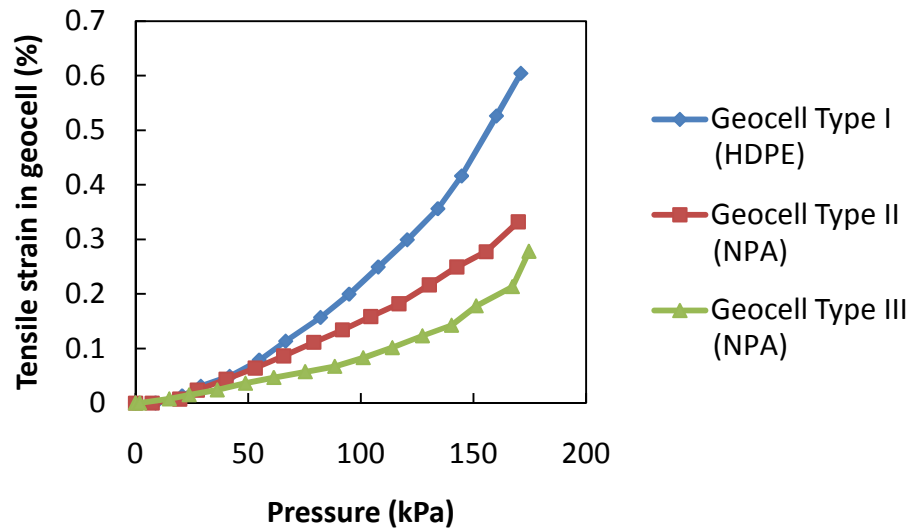


Figure 3.11 Tensile strain in geocell vs. pressure

3.3 Moving-wheel test

Moving-wheel tests were performed on unpaved road sections to study the behavior of geocell reinforced granular base courses under repeated loads. The test was performed using the accelerated pavement testing (APT) facility (Figure 3.12) at Kansas State University.

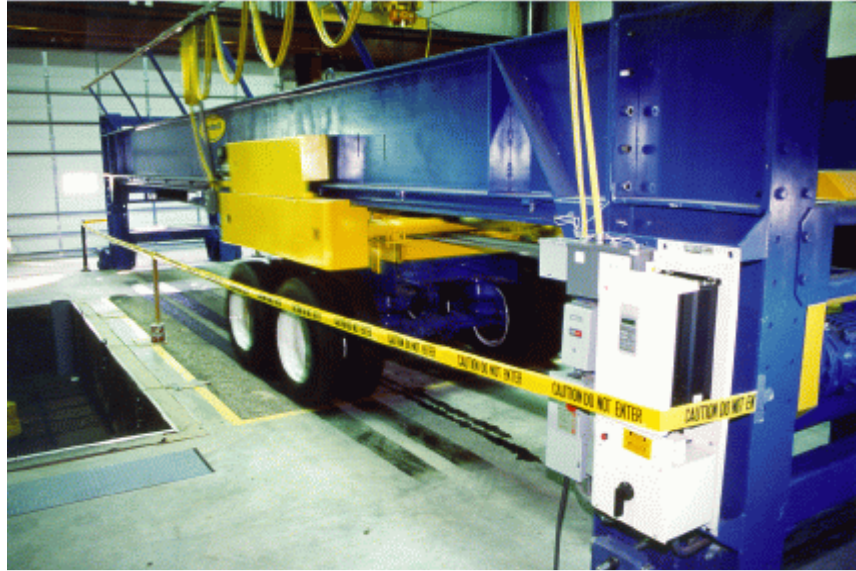


Figure 3.12 Accelerated pavement testing facility

3.3.1 Test setup and procedure

Four unpaved road sections were constructed inside a test pit of 6.1m long, 4.9m wide and 1.8m deep. The materials, instrumentation, and design thickness of each layer in the four test sections are shown in Figure 3.13. It should be noted that the actual layer profiles after construction were slightly different from the design thickness. The actual layer thickness was measured after the test and the values are provided in parentheses following the design thickness in Figure 3.13.

The clay subgrade was first prepared in layers by controlling the target California Bearing Ratio (CBR) at 5%. After the clay subgrade was prepared, Dynamic Cone Penetrometer (DCP) tests were performed at each test section to double check the stiffness of the subgrade. DCP test data are plotted in Figure

3.14. The CBR value of the soil can be estimated from the average DCP penetration rate (PR) using the following correlation:

$$CBR = 292/PR^{1.12} \quad 3.1$$

where the unit of *PR* is mm/blow. The estimated CBR values are 4.8 in Section 1, 5.8 in Section 2, 5.0 in Section 3, and 5.4 in Section 4.

The unreinforced sections (Sections 1 and 4) were originally designed using the same material and thickness as Sections 2 and 3 but without geocell. However, the unreinforced sections were so weak that the rut depth developed after the first wheel pass exceeded the displacement limit of the equipment, and the test had to be terminated. Sections 1 and 4 were then excavated and re-prepared using a whole layer of aggregate (AB-3) as the shown in Figure 3.13. The description of this aggregate will be provided later.

In the reinforced sections (Sections 2 and 3), a non-woven geotextile was first placed on the subgrade. Then Type IV NPA geocell was expanded and fixed on top of the geotextile (see Figure 3.15). Five strain gauges (locations marked in Figure 3.13) were installed on the NPA geocell in each section to measure horizontal strains at the mid-depth of the geocell. A local river sand (Kansas River sand) was used as the infill material of the geocell. After the NPA geocell had been filled, aggregate cover (AB-3) was placed on top of the geocell-

reinforced sand. Both the sand and the aggregate were compacted to 95% of the maximum density. The compaction was performed using a CAT CS54 vibratory soil compactor.

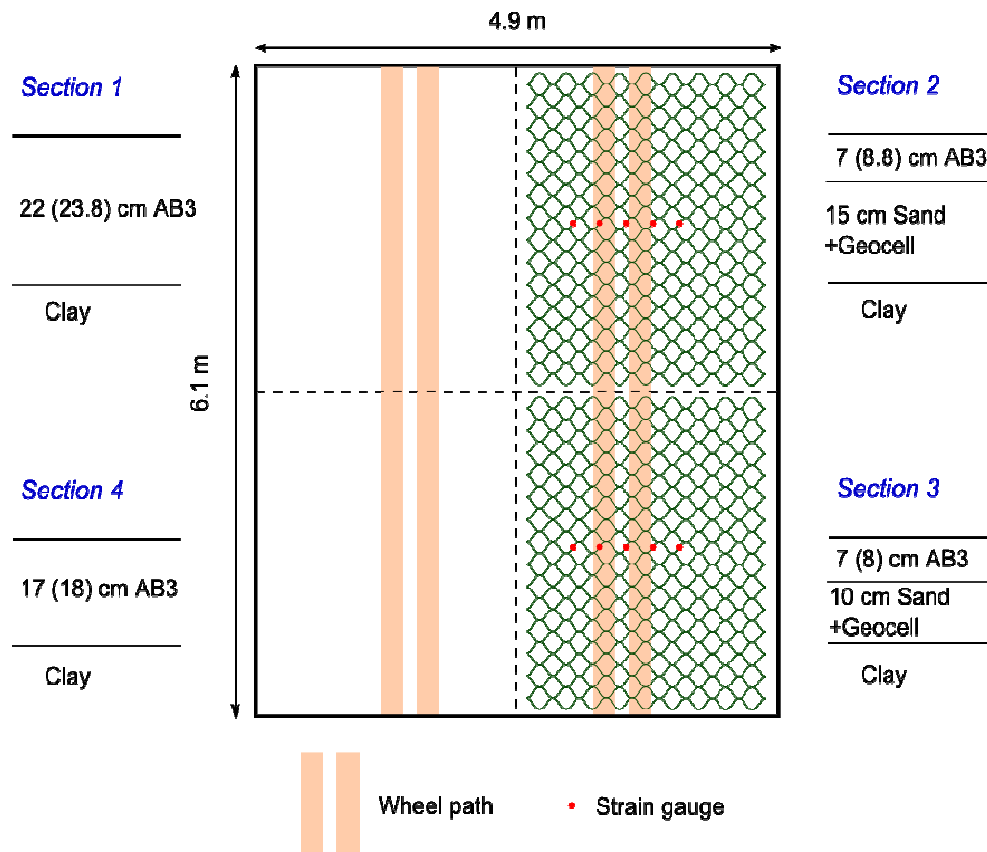


Figure 3.13 Moving-wheel test setup

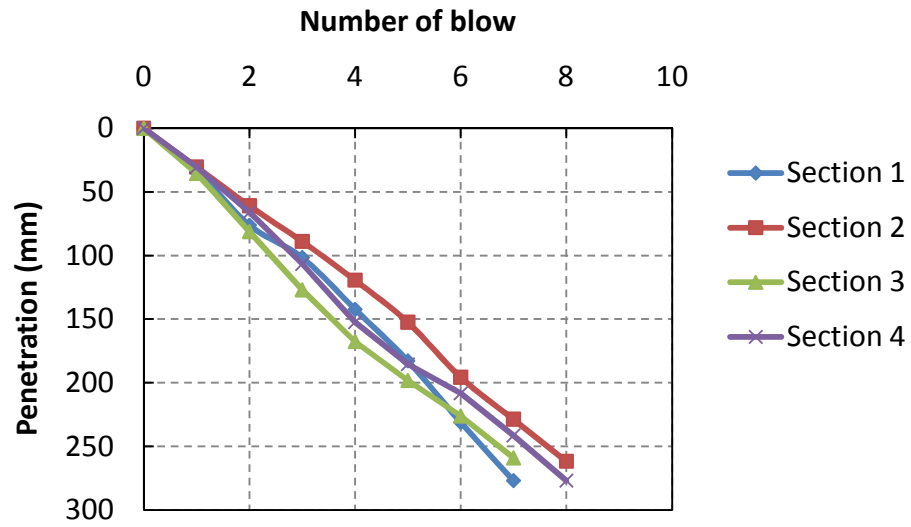


Figure 3.14 DCP test results from clay subgrade



Figure 3.15 Installation of NPA geocell

A repeated load of 80kN (18kips) was applied to the road sections by full-scale moving wheels with a single axle dual wheel setup. The tire pressure was set to

550kPa (80psi). The moving wheels ran back and forward on the unpaved road sections at a frequency of 10 passes/minute.

A total of 5000 passes of wheel load were applied to the road sections. Rut depths (maximum vertical displacement inside the wheel path) of each section were measured when the number of wheel passes reached 100, 200, 300, 400, 1000, 2000, 3000, 4000, and 5000.

3.3.2 Materials used

3.3.2.1 Subgrade clay

The subgrade material used in this study is classified as A-7-6 clay according to the AASHTO soil classification. Standard compaction tests (according to ASTM D698) were performed to determine the optimum moisture content and the maximum dry density of the clay (see Figure 3.16).

An unconfined compression test was performed on a reconstituted clay sample. The reconstituted clay was prepared by mixing oven-dried clay with water at a moisture content of 23.4% to achieve a target CBR of 5.0%. Then the soil was sealed for 48 hours to allow the moisture to be absorbed uniformly. Before the unconfined compression test, the moisture content and the CBR of the clay was re-determined in the laboratory. Test results showed that the moisture content

and CBR of the reconstituted clay were 22.7% and 5.4% respectively. The cylinder sample for the unconfined compression test was prepared following ASTM standard D1632-07.

The unconfined compression test device is shown in Figure 3.17. The clay sample used was 71mm in diameter and 157mm in height. The loading rate was controlled at 1 mm/min. The test result is plotted in Figure 3.18. It is shown that the subgrade clay has a Young's modulus E of 10.3MPa and an unconfined compressive strength q_u of 104.6kPa.

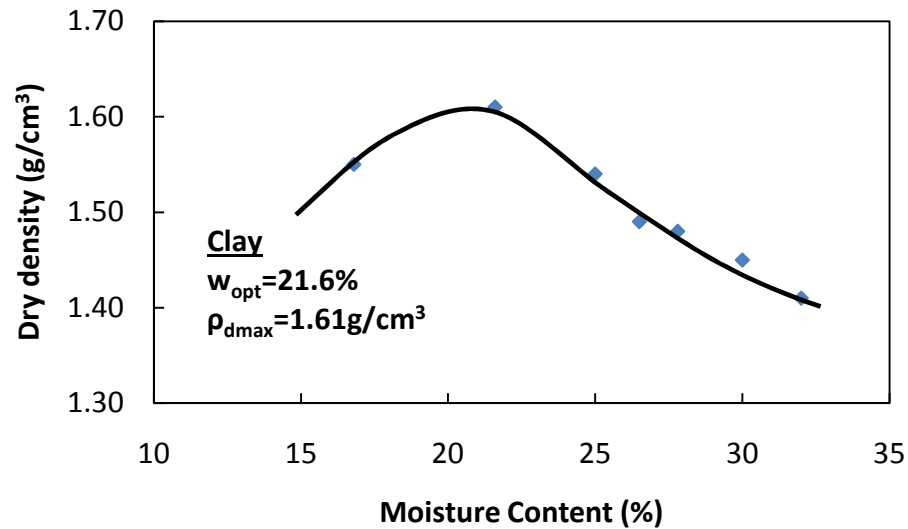


Figure 3.16 Compaction curve of the subgrade clay

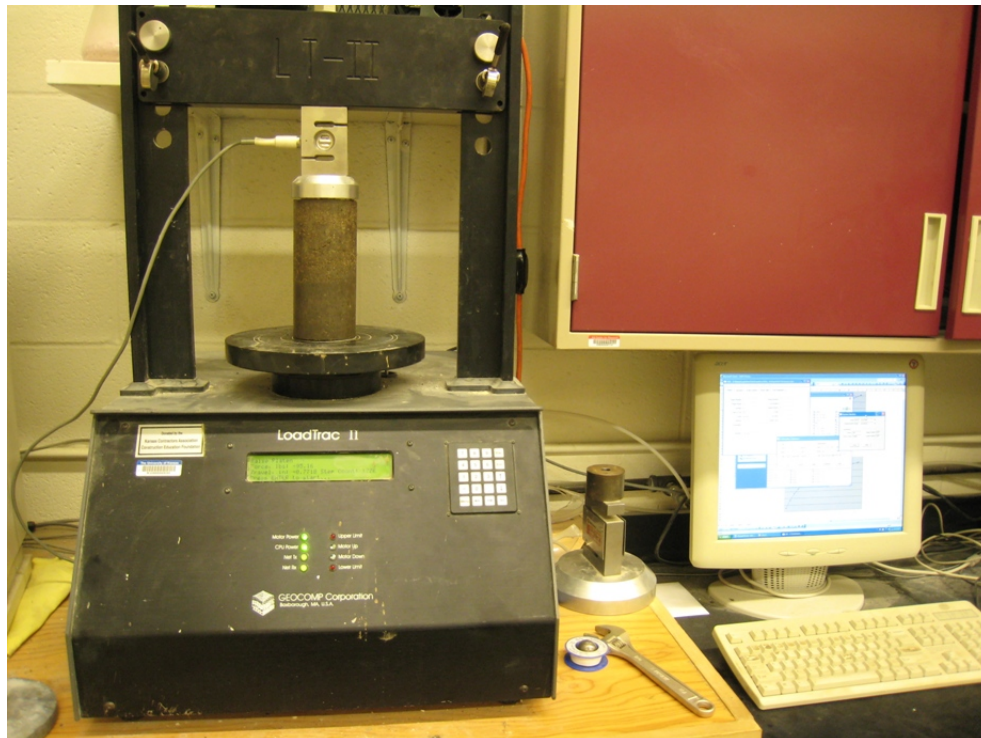


Figure 3.17 Unconfined compression test device

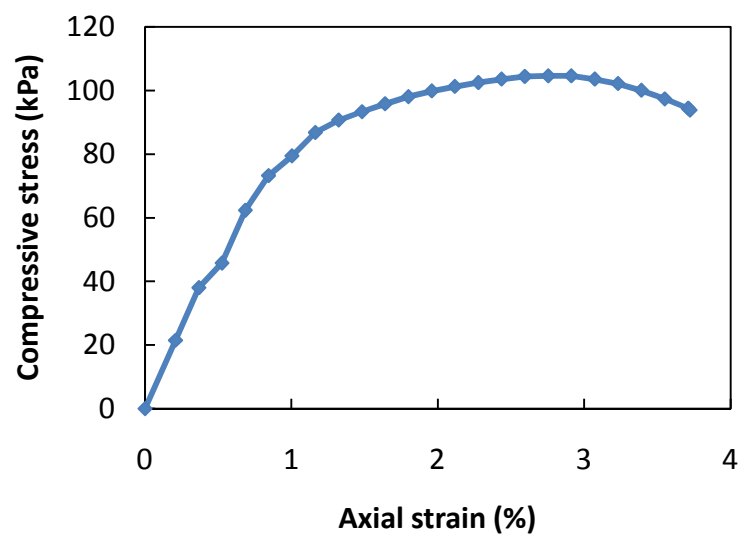


Figure 3.18 Unconfined compression test result

3.3.2.2 AB-3

A well-graded aggregate, AB-3, was used as the base material of unreinforced sections and the cover layer material in the reinforced sections. AB-3 is classified as A-1-a aggregate according to the AASHTO soil classification system. It is an ideal material for roadway base courses. The grain size distribution of AB-3 is shown in Figure 3.19. The standard compaction test result of AB-3 is shown in Figure 3.20.

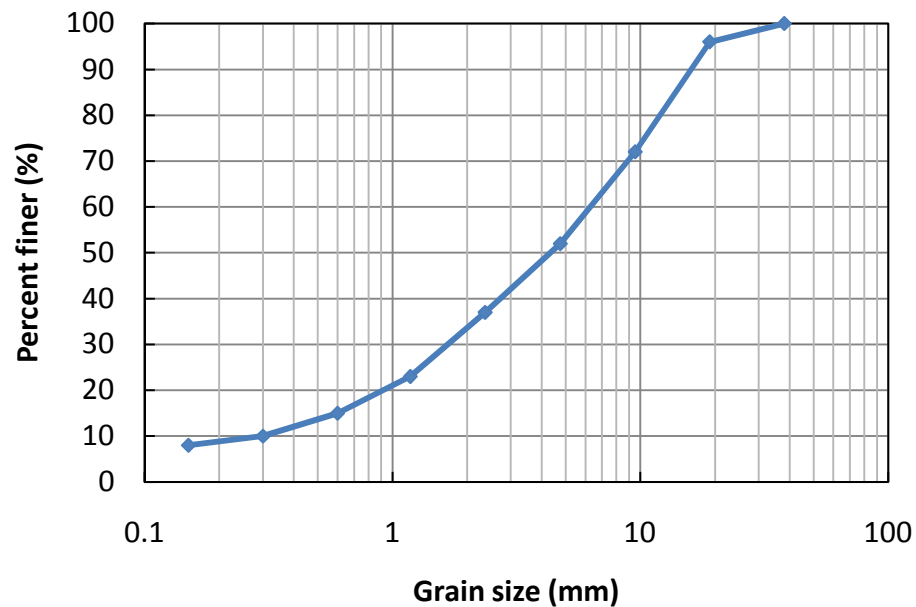


Figure 3.19 Grain size distribution of AB-3

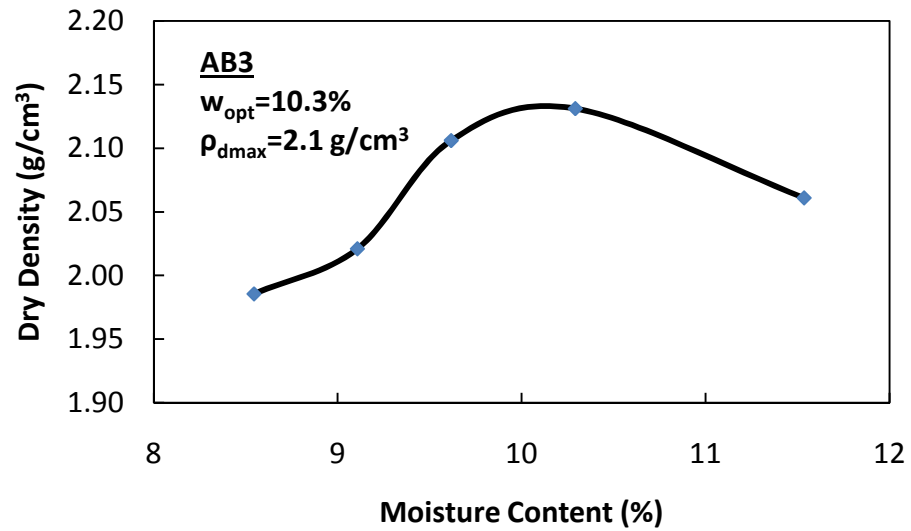


Figure 3.20 Compaction curve of AB-3

Direct shear tests were performed to determine the shear strength parameter of AB-3 at its optimum moisture content. Normal stresses of 5.3, 10.5 and 15.8 kPa were applied. The shear stress-displacement curves from the direct shear test are shown in Figure 3.21. The cohesion and friction angle obtained from the direct shear test are shown in Figure 3.22.

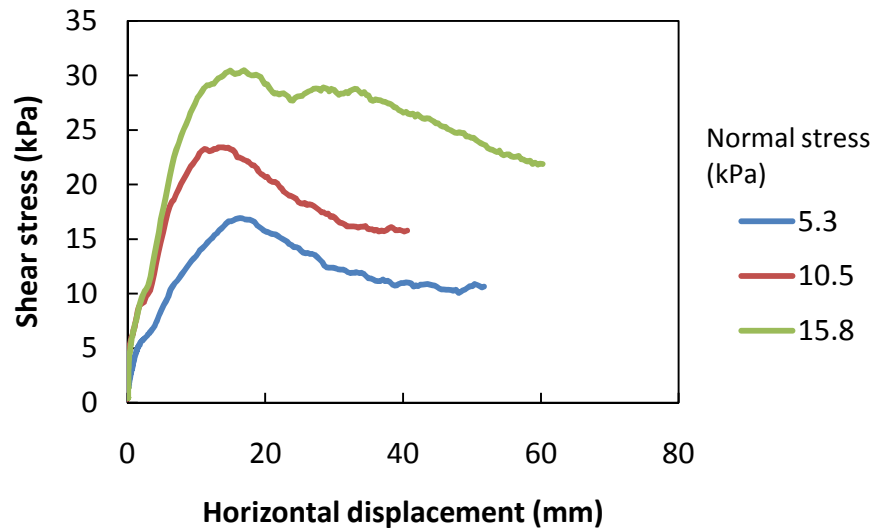


Figure 3.21 Shear stress vs. displacement

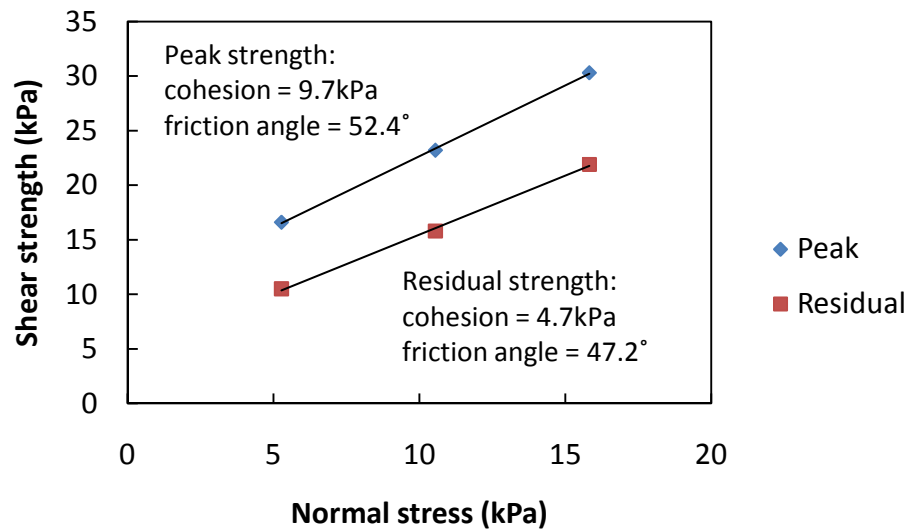


Figure 3.22 Shear strength vs. normal stress

A resilient modulus test was performed (according to the standard AASHTO T 307-99) on an AB3 sample compacted to 95% maximum density to determine the resilient modulus and permanent deformation parameters. The test was

performed using the cyclic triaxial test machine (shown in Figure 3.23) at the University of Illinois at Urbana-Champaign. The resilient modulus test results and the calibrated resilient modulus parameters (k_1 , k_2 , and k_3) for AB-3 are provided in Appendix A.



Figure 3.23 Cyclic triaxial test machine (UI-FastCell)

3.3.2.3 Kansas River sand

A local river sand (Kansas River sand) was used as the infill material for the geocell reinforced sections. This sand is classified as A-1-b sand according to the AASHTO soil classification system. Other properties of this sand are: minimum density $\rho_{d\ min} = 1.71\text{ g/cm}^3$, maximum density $\rho_{d\ max} = 1.97\text{ g/cm}^3$, and specific gravity $G_s = 2.58$. The grain size distribution of the Kansas River sand is shown in Figure 3.24. The standard compaction test result of the Kansas River sand is shown in Figure 3.25.

Triaxial compression and isotropic compression tests were also conducted. The triaxial compression tests were conducted under three different confining stress levels, i.e., 34.5kPa, 68.9kPa, and 137.9kPa. The triaxial test results are plotted in Figure 3.26 and Figure 3.27.

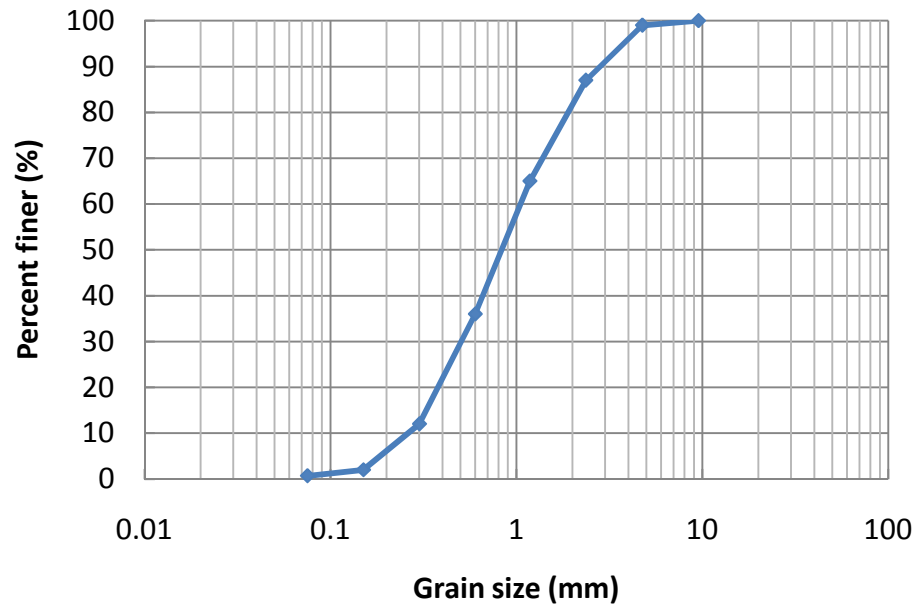


Figure 3.24 Grain size distribution of the river sand

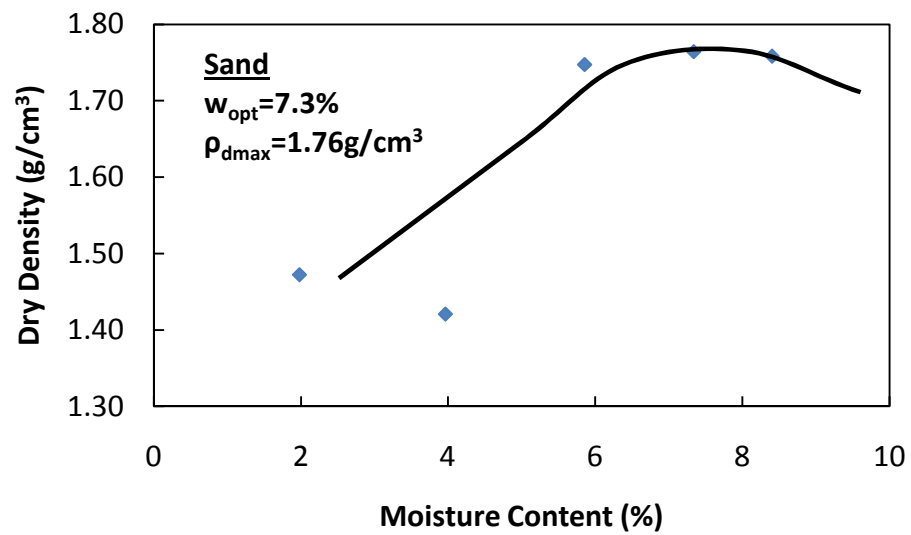


Figure 3.25 Compaction curve of the river sand

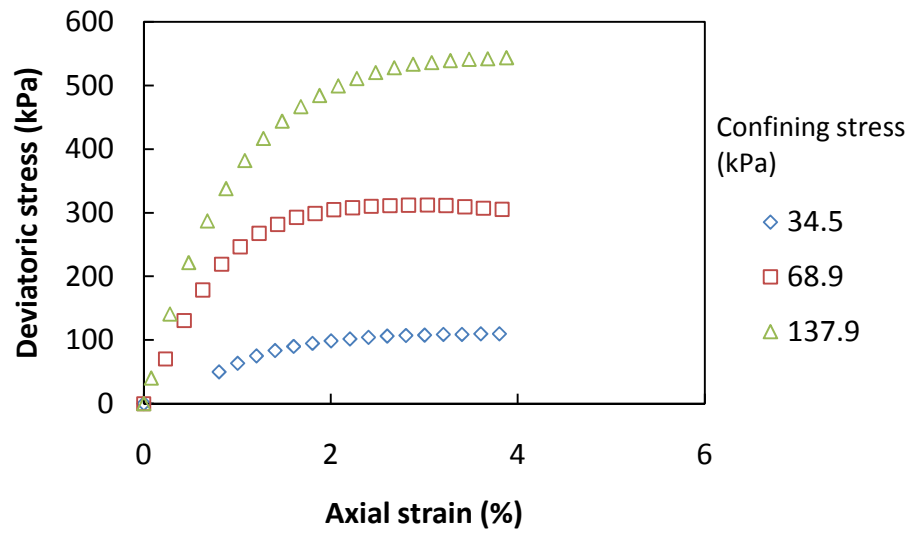


Figure 3.26 Triaxial compression test result

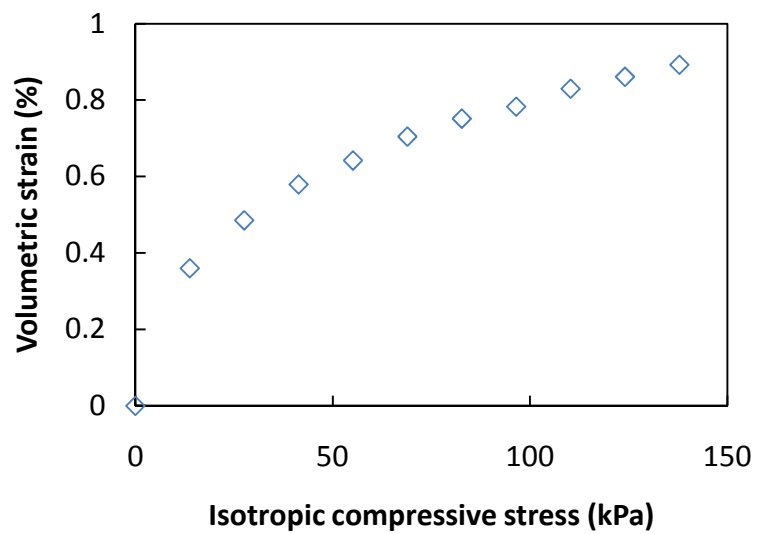


Figure 3.27 Isotropic compression test result

A resilient modulus test was performed on the Kansas River sand sample prepared at 95% maximum density. The test procedure for this sand was the

same as that for AB3. The resilient modulus test result and the calibrated resilient modulus parameters (k_1 , k_2 , and k_3) for Kansas River sand are provided in Appendix A.

3.3.2.4 Geocell

The NPA geocell (Type IV) was used in the moving-wheel tests. A description about the NPA material has been provided previously. The cell pocket size of the Type IV geocell was the same as that of Type I, II, and III geocells discussed earlier. The stress-strain behavior of Type IV NPA geocell material is shown in Figure 3.9 and Table 3.1 together with the other three geocell materials used in the static load test. Some other properties of the NPA material provided by the manufacturer are presented previously in Table 3.2 and Table 3.3.

3.3.3 Test results and discussion

The rut depth development with the number of wheel passes in each test section is plotted in Figure 3.28. After 5000 wheel passes, the accumulated rut depths in Sections 1, 2, and 4 appeared to become stable, whereas Section 3 continued to develop considerable rutting. The final rut depth in Section 1, 2, 3, and 4 after 5000 wheel passes were respectively 4.9, 4.8, 9.3, and 5.5 cm. In the two unreinforced sections, Section 4 (with an 18-cm-thick AB-3 base) developed slightly more rutting than Section 1 (with a 23.8-cm-thick AB-3 base). The

thicker aggregate base course, in this case, provided marginal benefit in reducing rut depth, mainly because the subgrade (CBR=5%) was relatively firm. On the contrary, in the two geocell-reinforced sections, Section 3 (with a 10cm geocell-reinforced sand layer) developed much more rutting than Section 2 (with a 15cm geocell-reinforced sand layer). Figure 3.28 shows that the rut depth development in Section 3 was close to that in Section 4 when the number of passes is less than 1000, beyond which Section 3 started to develop considerably more rut than Section 4.

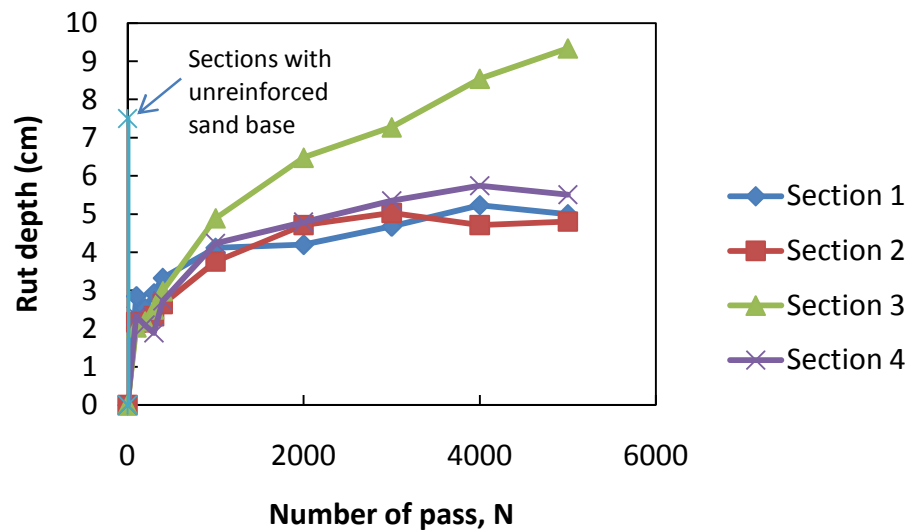
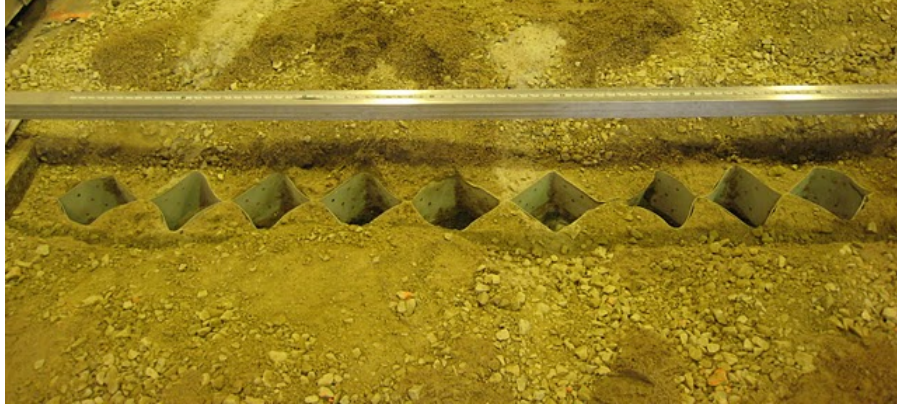


Figure 3.28 Rut depth vs. Number of passes, N

To investigate the failure mode, the geocells in Sections 2 and 3 were exhumed. It was found that the failure mode of the geocell reinforced sand in Section 3 was a “cell bursting” failure. The geocell in Section 3 where peeled apart at the joints (especially the joints under the wheel path) and the infill soil escaped laterally

out of the cell. On the contrary, the geocell in Section 2 remained contact. This phenomenon indicates that the tensile strength of the geocell joint (rather than the tensile strength of geocell material) may control the behavior of geocell reinforced soil when the geocell reinforced base course is relatively thin. The quick development of rut in Section 3 after 1000 wheel passes was likely caused by the tensile failure of some of the geocell joints under the wheel path.

After Sections 2 and 3 exhumed, the layer profiles were recorded at the top of geocell and the top of subgrade (see Figure 3.30 and Figure 3.31). In Section 2, small vertical deformation was found under the wheel path, and most of the vertical compression took place in the base layer. Whereas in Section 3, the cover aggregate was pressed into the cells and mixed with the sand layer, and considerable vertical deformation was observed on the top of the subgrade. This result indicates that the geocell-reinforced sand can effectively stabilize unpaved road bases, but the geocell-reinforced layer must be thick enough to prevent shallow failure.



(a) Section 2 (15cm geocell-reinforced sand + 8.8cm AB3 cover)



(b) Section 3 (10cm geocell-reinforced sand + 8.0cm AB3 cover)

Figure 3.29 Exhumed geocells in Sections 2 and 3

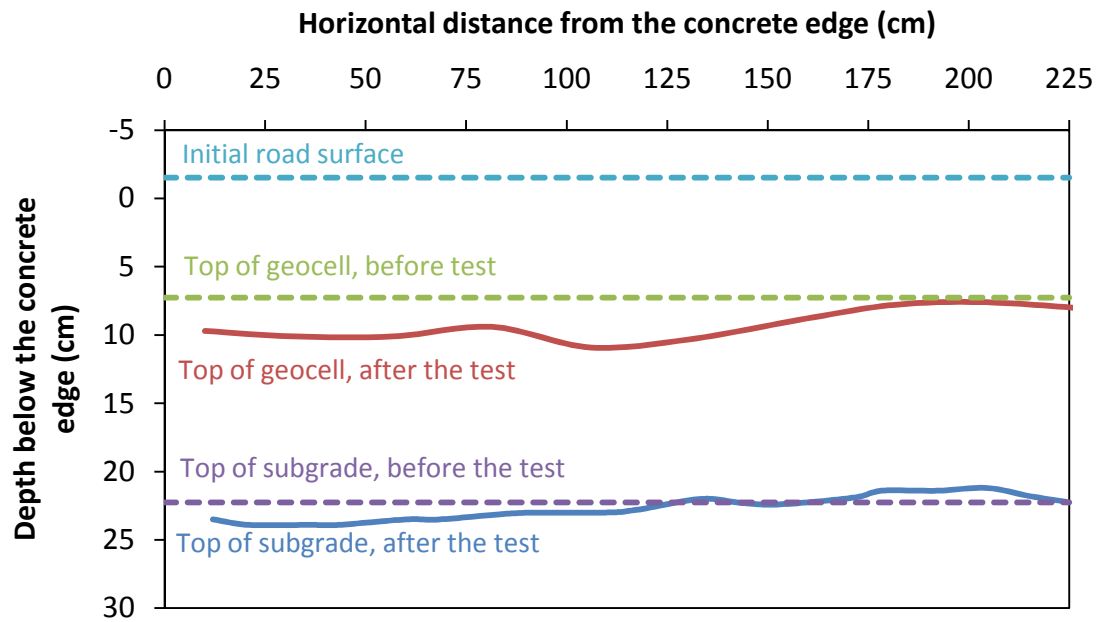


Figure 3.30 Road section profile before and after the test (Section 2)

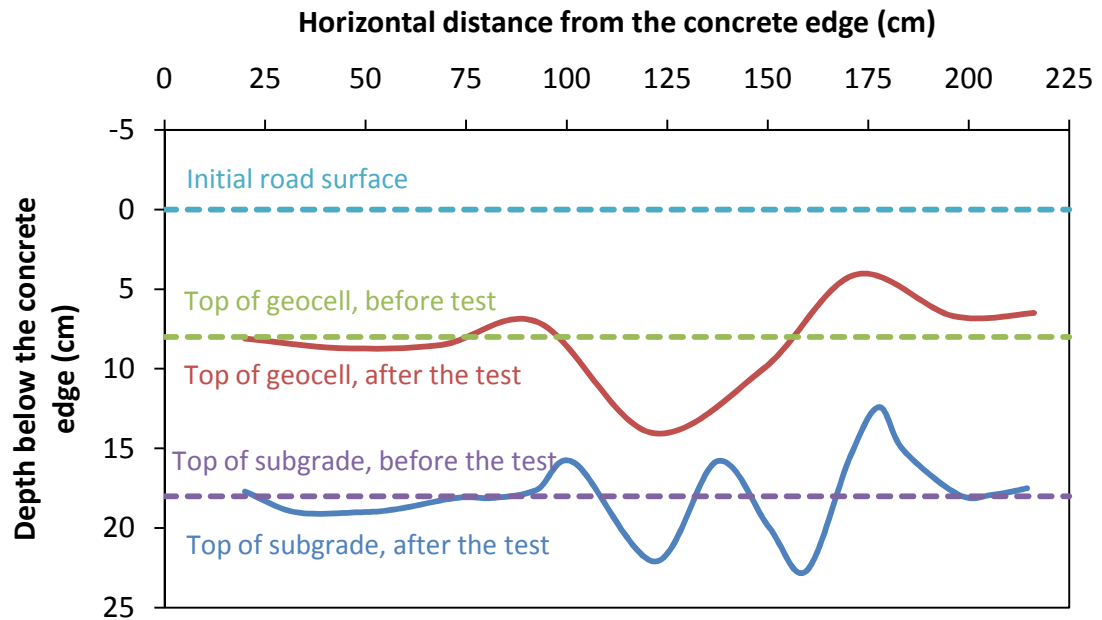


Figure 3.31 Road section profiles before and after the test (Section 3)

Five strain gauges each were installed on the NPA geocell in Sections 2 and 3. The locations of the strain gauges relative to the wheels are illustrated in Figure 3.32. The horizontal strain data was recorded up to 2000 wheel passes. From the vast amount of strain data, the peak strains and the residual (permanent) strains at certain numbers of wheel passes were selected and listed in Table 3.4 and Table 3.5. In this dissertation, a positive value represents a tensile strain, and a negative value represents a compressive strain.

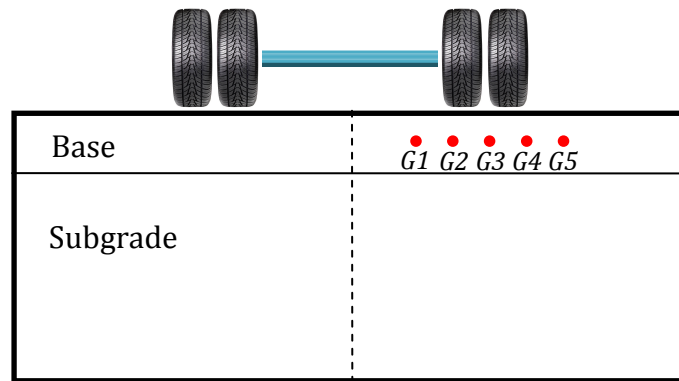


Figure 3.32 Location of the strain gauges

Table 3.4 Peak horizontal strain in the geocell (Unit: %, Positive = Tension)

Section 2 (15cm geocell reinforced sand + 8.8cm AB3 cover)						Section 3 (10cm geocell reinforced sand + 8cm AB3 cover)				
<i>N</i>	G1	G2	G3	G4	G5	G1	G2	G3	G4	G5
25	-0.090	0.296	0.115	0.126	-0.083	--	0.318	>2	0.240	--
50	-0.104	0.314	0.134	0.133	-0.101	--	0.341	>2	0.282	--
100	-0.110	0.338	0.152	0.108	-0.104	--	0.381	--	0.320	--
200	-0.100	0.331	0.167	0.101	-0.106	--	--	--	0.369	--
300	-0.091	0.329	0.175	0.091	-0.108	--	--	--	0.435	--
500	-0.081	0.351	0.200	0.072	-0.100	--	--	--	0.581	--
1000	-0.051	0.423	0.234	0.072	-0.090	--	--	--	0.785	--
2000	-0.023	0.539	0.298	0.096	-0.075	--	--	--	--	--

Table 3.5 Residual horizontal strain in the geocell (Unit: %, Positive = Tension)

Section 2 (15cm geocell reinforced sand + 8.8cm AB3 cover)						Section 3 (10cm geocell reinforced sand + 8cm AB3 cover)				
N	G1	G2	G3	G4	G5	G1	G2	G3	G4	G5
25	-0.049	0.045	0.046	-0.003	-0.044	--	0.043	0.164	-0.011	--
50	-0.063	0.054	0.062	-0.009	-0.059	--	0.040	0.083	0.006	--
100	-0.054	0.068	0.072	-0.025	-0.067	--	0.051	--	0.029	--
200	-0.063	0.082	0.079	-0.060	-0.070	--	--	--	0.075	--
300	-0.058	0.094	0.088	-0.063	-0.071	--	--	--	0.124	--
500	-0.047	0.122	0.107	-0.084	-0.066	--	--	--	0.250	--
1000	-0.020	0.201	0.148	-0.090	-0.054	--	--	--	0.418	--
2000	0.006	0.329	0.205	-0.077	-0.040	--	--	--	--	--

Overall, the strain data indicated that the geocell experienced tensile strains under the wheel path and compressive strains outside the wheel path. In Section 2, strain data were obtained from all the five gauges up to 2000 wheel passes. The profile of peak and residual horizontal strains in the geocell across the wheel path were plotted in Figure 3.33 and Figure 3.34. The largest peak tensile strain recorded in this section was 0.54%. The strain data are also plotted in Figure 3.35 and Figure 3.36 against the number of wheel passes. It is shown that the tensile strain of the geocell under the wheel path increased with the number of wheel passes. The compressive strain of the geocell outside the wheel path initially increased with the number of wheel passes then started to decrease after a certain point. In Section 3, only limited amount of strain data were obtained. Two of the strain gauges (G1 and G5) were broken during the base course construction. During the test, the data acquisition system lost connection with strain gauge G2 after 50 wheel passes and G3 after 100 wheel passes. Strain gauge G4 was able to work until 1000 wheel passes. The

disconnection during the test may be caused by the large deformation of the geocell in this section, as observed after exhuming the section. Compared to the strain measured in Section 2, the strains measured in Section 3 were much larger. The maximum tensile strain of the geocell in Section 3 exceeded 2% (the maximum value these strain gauges can measure) after 25 wheel passes.

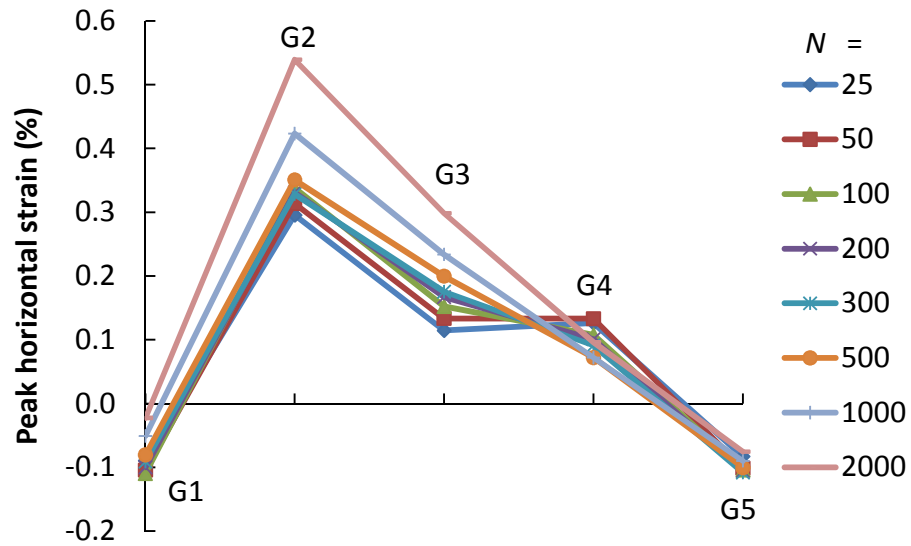


Figure 3.33 Profile of the peak horizontal strain in geocell across the wheel path (Section 2)

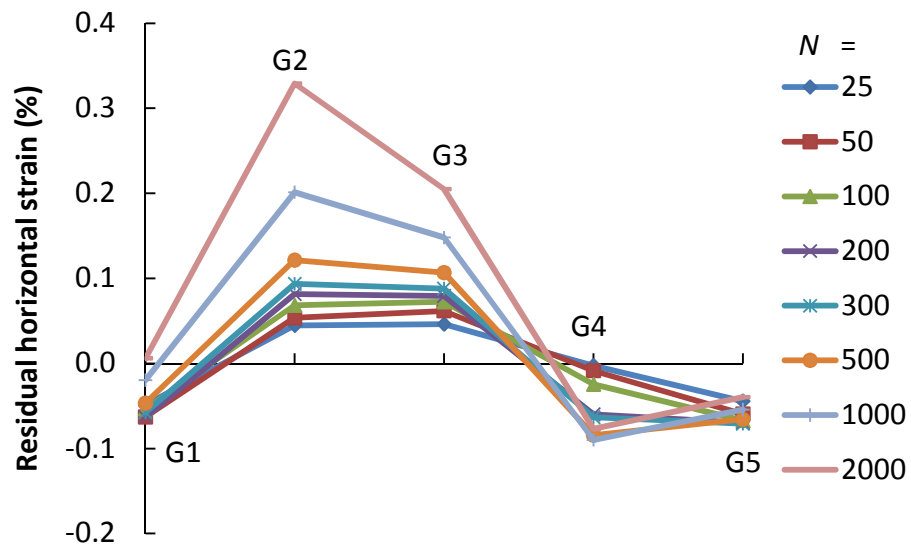


Figure 3.34 Profile of the residual horizontal strain in geocell across the wheel path (Section 2)

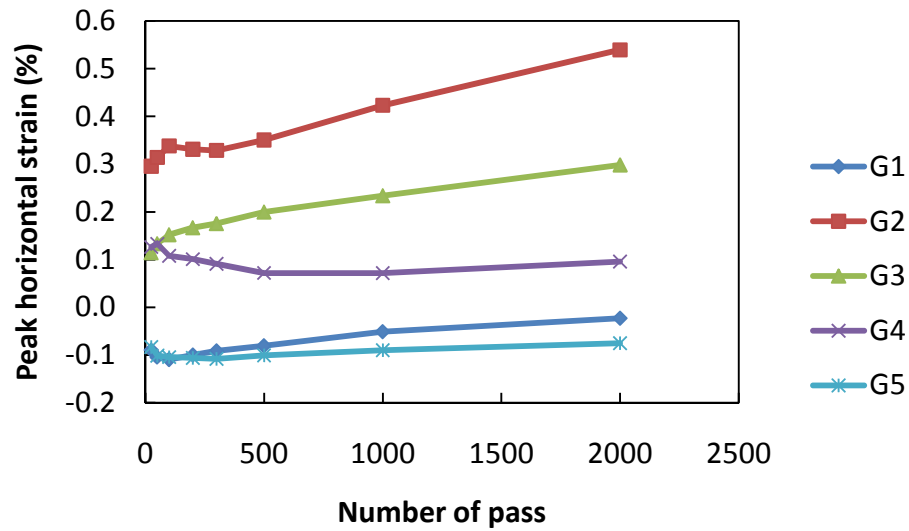


Figure 3.35 Peak horizontal strain in geocell vs. number of passes (Section 2)

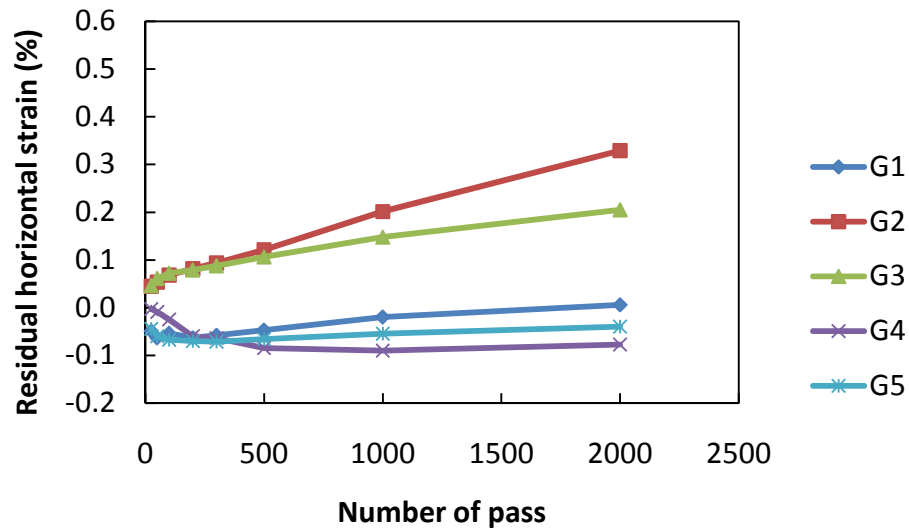


Figure 3.36 Residual horizontal strain in geocell vs. number of pass (Section 2)

3.4 Summary

This chapter describes the static load test and the moving-wheel test conducted in this study. The data obtained from these tests will be used to verify and calibrate the numerical models created in this study. Some conclusions can be drawn from the test results:

- (1) The static load test demonstrated that geocell-reinforcement improved the bearing capacity of the granular soil. The stiffness of the granular soil was also improved. However the improvement in soil stiffness was not significant until the geocell reinforced soil deformed to some extent.
- (2) For the particular test setup in this study, the ultimate tensile strength of the NPA geocell has no significant influence on the bearing capacity of the geocell-reinforced sand. Based on the measured strain of the geocell, the maximum tensile strain (<1%) developed in the geocell was much lower than the tensile strain (>10%) needed to mobilize the ultimate tensile strength of the material.
- (3) The moving wheel demonstrated the NPA geocell had a significant effect in improving the stability of unpaved roads and reducing the permanent deformation. Without the geocell-reinforcement, the unpaved road base with 15cm sand and 8.8cm AB3 cover could not support 80 kN (18 kips) traffic axle load for one pass. When geocell reinforcement was used, the same base course only developed 4.8cm rut depth after 5000 wheel passes,

which is comparable to the performance of a 23.8cm aggregate base course on the same subgrade.

- (4) Base course thickness is an important factor that influences the stability of the unpaved road under moving wheel loads. The geocell-reinforcement must be designed thick enough for the unpaved road to be stable.
- (5) For the particular test setup in this study, the geocell-reinforced base course with an inadequate thickness had a “cell bursting” failure. Under the wheel load, both the vertical and the horizontal stresses in the base under the wheel path increased considerably. The lateral movement of soil was restricted by the geocell. When the tensile stresses at joints of geocell exceeded the tensile strength of the joint (typically lower than the tensile strength of the geocell material), the soil escaped through the geocell joint and moved laterally to both sides of the wheel path. The loss of the base material under the wheel path resulted in a significant increase in the rut depth of the road.
- (6) Strain gauges were installed on the NPA geocell for the static load test and the moving-wheel test. In the static load test, the maximum tensile strain measured in the geocell was 0.6%. In the moving-wheel test, the maximum tensile strain measured in the geocell was 0.54% from the 15cm thick geocell and more than 2% from the 10cm thick geocell. The strain data also indicated that under the wheel load, the geocell under the wheel path experienced tensile stresses whereas the geocell outside the wheel path experienced compressive stresses. As the deformation of the geocell

increased, the horizontal stress in the geocell outside the wheel tended to transfer from compression to tension.

Chapter 4 Numerical analysis of geocell-reinforced soil under a static load

4.1 Overview

To investigate the mechanism of the geocell reinforcement, numerical analysis was carried out using a commercial software, Fast Lagrangian Analysis of Continua (FLAC^{3D}). In this chapter, numerical models were created to simulate the static load tests on unreinforced and geocell-reinforced sand. The test setup, materials, and test results were described in Chapter 3.

4.2 FLAC^{3D}

The numerical analysis in this study was performed using a commercial software, FLAC^{3D}. FLAC^{3D} is a finite difference program specially designed for solving three-dimensional geotechnical engineering problems. It has 11 built-in constitutive models (3 elastic and 8 elasto-plastic) for modeling various types of geomaterials. Reinforcements (e.g., pile, liner, soil nail, geosynthetic, etc.) can be modeled with special structure elements. Users are also allowed to produce and use their own constitutive model, which is also called user defined model (UDM). UDM should be programmed with C++ and compiled to a DLL file to be incorporated into FLAC^{3D}.

4.3 Material models and parameters

4.3.1 Sand

Based on the review of existing literature, the Duncan-Chang model (Duncan et al. 1980) was selected to model the poorly-graded dry sand used in the static load test. The constitutive equations for the Duncan-Chang model were described in Chapter 2. Two modifications to this model were adopted in this study. One is the tangent bulk modulus equation (Equation 2.11) proposed by Boscardin et al. (1990), and the other is the consideration of the effect of the intermediate principle stress σ_2 by substituting all the (σ_3/p_a) terms in Equations 2.8 to 2.10 by $(\sigma_2 + \sigma_3)/(2p_a)$. Details about these modifications were also discussed in Chapter 2. The Duncan-Chang model parameters (listed in Table 4.1) were calibrated from the results of the triaxial compression tests and the isotropic compression test discussed in Chapter 3. The triaxial test results and calculated stress-strain curves by the Duncan-Chang model are compared in Figure 4.1 and Figure 4.2. The comparison shows that the Duncan-Chang model can simulate the stress-strain behavior of this sand well.

The Duncan-Chang model is not a built-in constitutive model in FLAC^{3D}. In this study, the constitutive equations of the Duncan-Chang model were programmed in C++ and compiled to a DLL file, which was incorporated into FLAC^{3D} for analyses.

Table 4.1 Duncan-Chang model parameters for the sand

Parameters	Symbol	Unit	Values
Cohesion	c	kPa	1.0
Initial friction angle	ϕ_0	Degree	40.9
Friction angle parameter	$\Delta\phi$	Degree	0
Initial bulk modulus	B_i	kPa	3039
Asymptotic volumetric strain	ε_u	--	0.02
Failure ratio	R_f	--	0.76
Modulus number	K	--	555
Modulus exponent	n	--	0.37

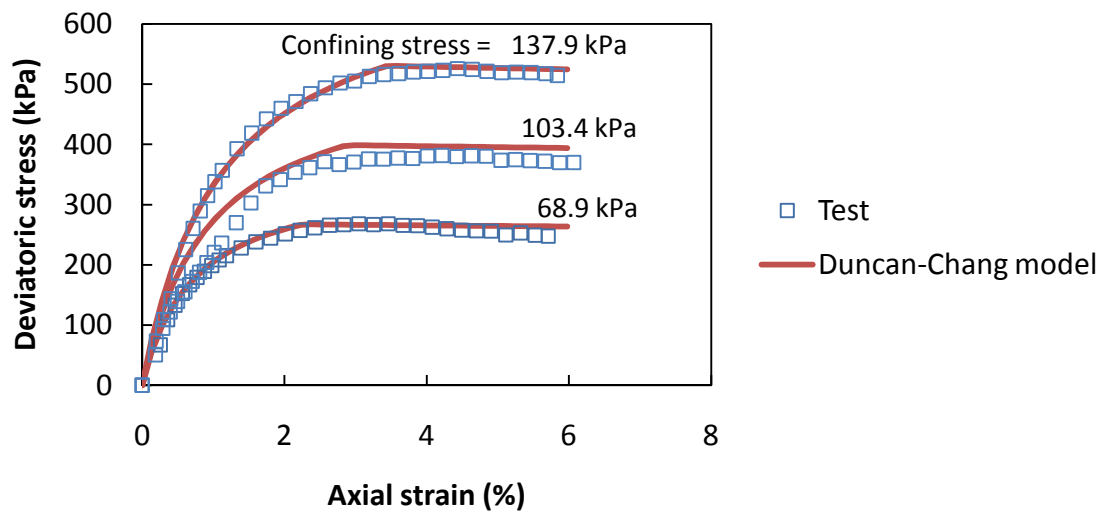


Figure 4.1 Triaxial compression test data vs. calculated results

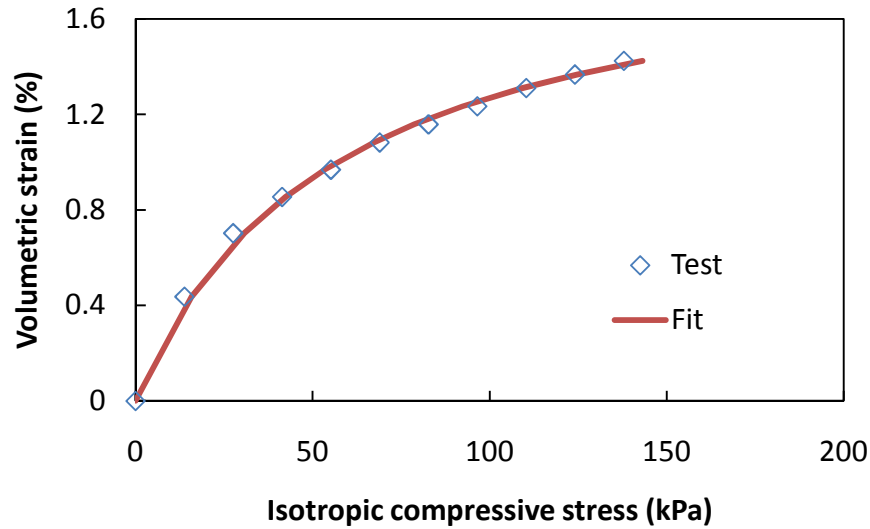


Figure 4.2 Isotropic compression test data vs. calculated results

4.3.2 Geocell

With the development of material science and technology, geocell manufacturers are making their products stiffer and stronger. A thin geocell strip today may carry a considerable bending load in addition to the membrane stresses. Thus in this study, plate elements were used instead of the membrane elements for modeling geocell. Polymeric materials often have non-linear and time-dependent stress-strain relationships. Such behavior was successfully modeled by some researchers (Ling et al. 2000; Wesseloo et al. 2004). However, as discussed in Chapter 3, the maximum tensile strain measured in the NPA geocell during the static load test was only about 0.6%. At such a small strain level, the geocell can be assumed as linearly elastic.

The interface friction is another important mechanism of geocell reinforcement. In this study, the shear stress-strain relationship between the geocell and the infill soil was modeled linearly with a Mohr-Coulomb yield criterion as shown in Figure 4.3.

The model parameters for geocell are listed in Table 4.2. The Young's moduli E of different types of geocell were obtained from the stress-strain curves at 1% tensile strain. Poisson's ratio ν of the HDPE and NPA materials was assumed to be 0.45. The interface shear modulus k_i was determined as 19.7MPa/m from interface direct shear tests under a normal stress of 68.9 kPa (10psi). Interface cohesion c_i and interface friction angle ϕ_i were estimated by multiplying the cohesion and the friction angle of the sand by an interaction coefficient of 0.8.

Table 4.2 Model parameters for the geocell

Parameters	Symbol	Unit	Values
Young's modulus	E	MPa	392 (Type I HDPE) 418 (Type II NPA) 550 (Type III NPA)
Poisson's ratio	ν	--	0.45
Interface shear modulus	k_i	MPa/m	19.7
Interface cohesion	c_i	kPa	0.8
Interface friction angle	ϕ_i	Degree	34.7
Thickness of the geocell	t	mm	1.5 (Type I HDPE) 1.1 (Type II NPA) 1.1 (Type III NPA)

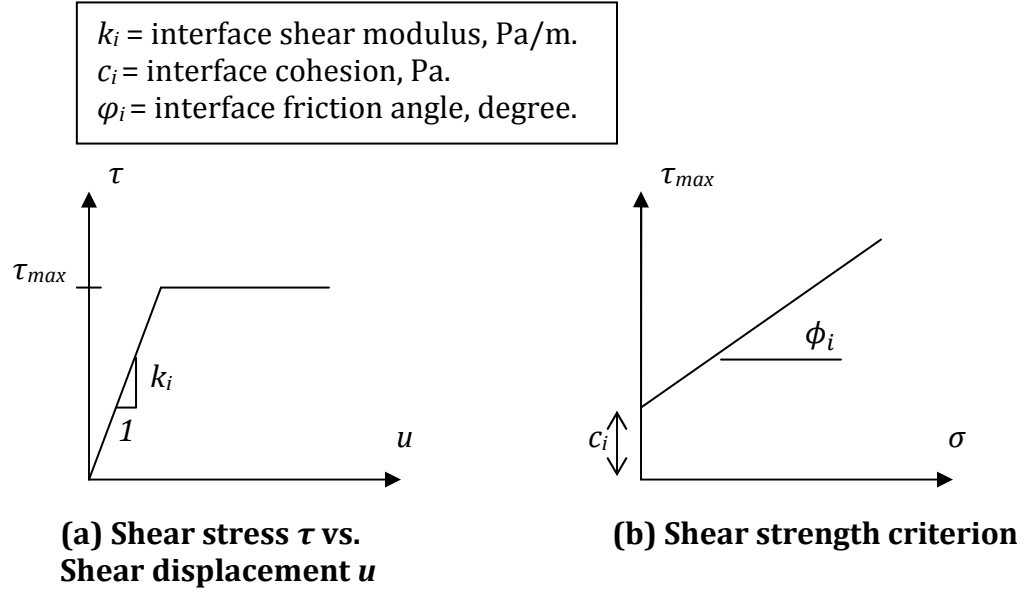


Figure 4.3 Interface shear behavior between the infill soil and the geocell

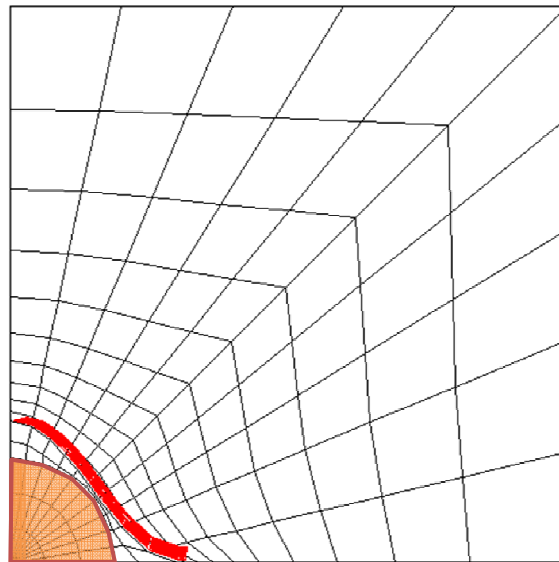
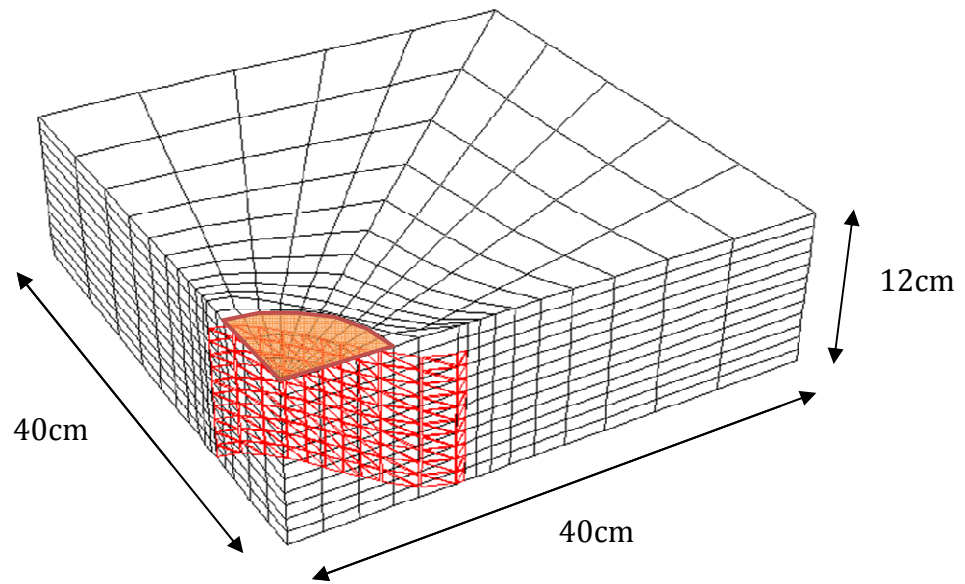
4.4 Modeling of the static load test

Numerical models were created with FLAC^{3D} to simulate the result of laboratory static load tests. The constitutive models and the parameter calibrations have been described in the previous sections.

4.4.1 Numerical mesh and boundary conditions

A quarter of the test box was modeled due to the symmetry of the test setup (see Figure 4.4). Vertical movement was fixed at the bottom boundary of the model, and horizontal movement was fixed at the four side boundaries. To account for

the compaction effect, the initial coefficient of lateral earth pressure k_0 was set as 1 in both the unreinforced and the reinforced cases. This value is higher than the typical k_0 for soils at rest. The value of 1 was selected to consider the increased horizontal stress after compaction. A velocity boundary ($V=-1\times 10^{-7}$ m/step) was applied on top of the sand (within the shaded region in Figure 4.4) to simulate the vertical load applied by a rigid plate. The models were solved for 10000 iteration steps until the vertical displacement on the top of the soil reached 10mm.



Top view

S

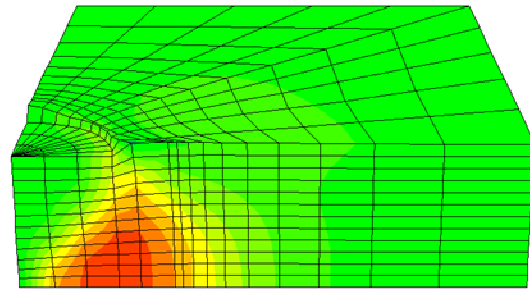
4.4.2 Numerical results

Figure 4.5 shows the horizontal displacement (in the x direction) contour in the unreinforced and reinforced models. It is obvious that, under the same plate displacement of 10mm on top of the sand, the unreinforced sand developed more horizontal movement than the reinforced sand. In the unreinforced case (shown in Figure 4.5(a)), the maximum horizontal displacement (=3.8mm) happened at the bottom of the sand layer. Whereas in the three reinforced case (shown in Figure 4.5(b)(c)(d)), the lateral movement of the sand was restrained by the geocell. The maximum horizontal displacement in the reinforced sand was 2.8mm with type I geocell, 2.9mm with type II geocell, and 2.8mm with type III geocell.

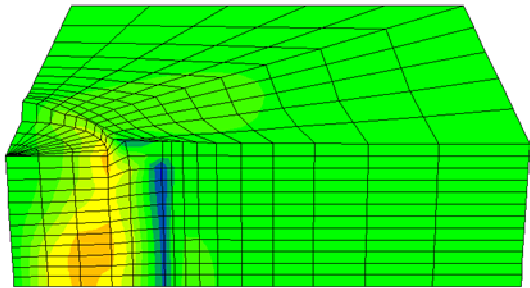
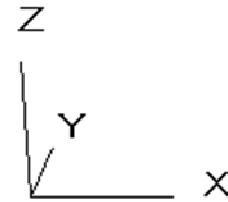
Figure 4.6 shows the horizontal stress (in the x direction) contours in the unreinforced and reinforced models. It is shown that, because of the lateral confinement from the geocell, the geocell-reinforced sand developed more horizontal stress than the unreinforced sand under the same plate displacement of 10mm on top of the sand. The maximum horizontal stress (in the x direction) developed in the unreinforced sand was 36.9kPa. Whereas the maximum horizontal stress (in the x direction) developed in the sand was 65.1kPa within Type I HDPE geocell, 61.7kPa with Type II NPA geocell, and 68.0kPa with Type III NPA geocell. A sudden change of horizontal stress was observed at the location of the geocell in the reinforced model, which means that the horizontal

stress inside the geocell was taken mostly by the geocell rather than the sand outside the geocell.

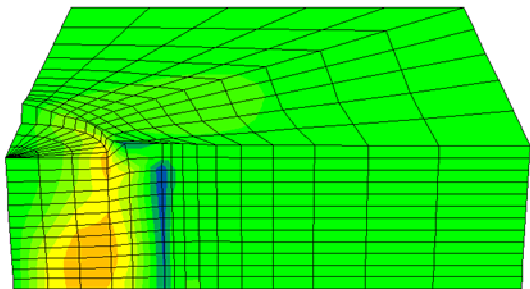
Figure 4.7 shows the horizontal tensile stresses in the three types of geocell. The maximum tensile stresses developed were 2.84kN/m in Type I HDPE geocell, 2.60kN/m in Type II NPA geocell, and 2.89kN/m in Type III NPA geocell. The location of the maximum tensile stress was at the bottom of the geocell.



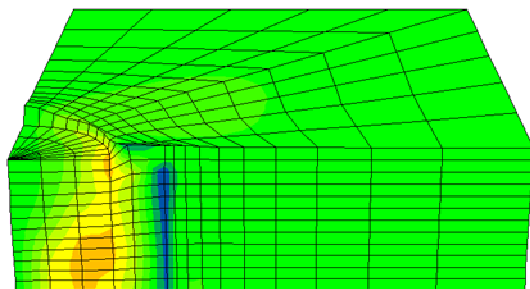
(a) Unreinforced



(b) Geocell-reinforced (Type I HDPE)



(c) Geocell-reinforced (Type II NPA)

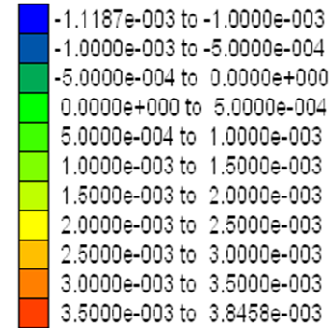


(d) Geocell-reinforced (Type III NPA)

Contour of X-Displacement

Magfac = 1.000e+000

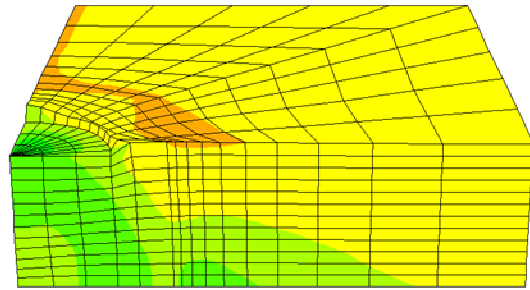
Live mech zones shown



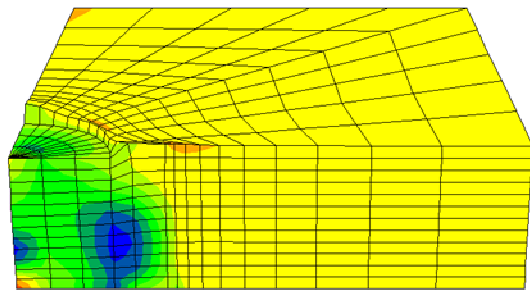
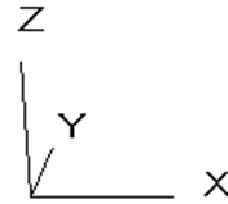
Interval = 5.0e-004

Unit: m

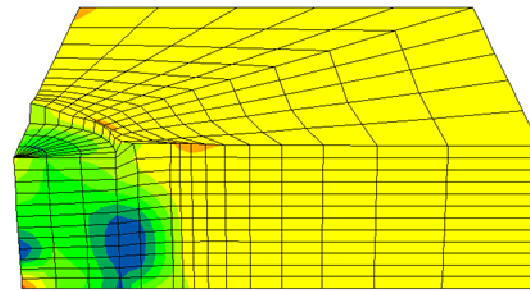
Figure 4.5 Horizontal displacement contour (Plate displacement = 10mm)



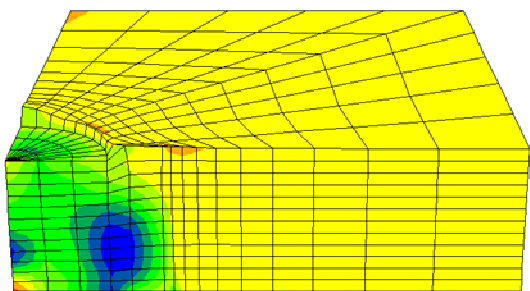
(a) Unreinforced



(b) Geocell-reinforced (Type I HDPE)



(c) Geocell-reinforced (Type II NPA)



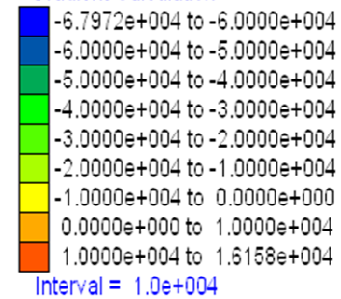
(d) Geocell-reinforced (Type III NPA)

Contour of SXX

Magfac = 1.000e+000

Live mech zones shown

Gradient Calculation

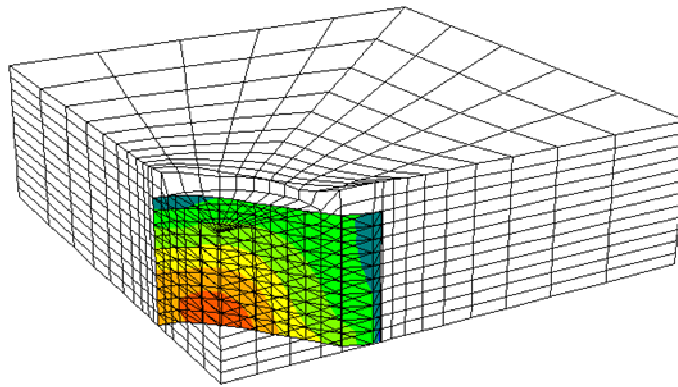


Unit: Pa

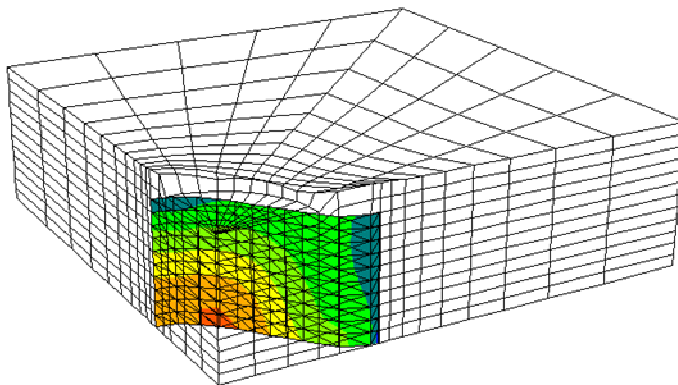
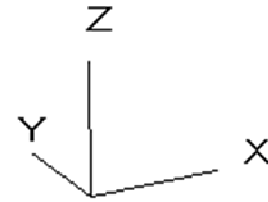
Positive=Tension

Negative=Compression

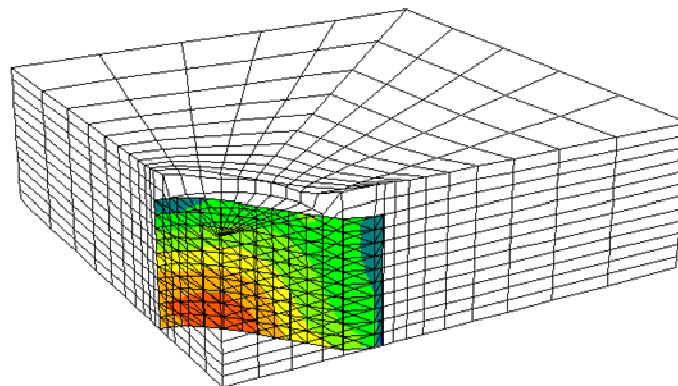
Figure 4.6 Horizontal stress contour (Plate displacement = 10mm)



(a) Type I HDPE geocell



(b) Type II NPA geocell



(c) Type III NPA geocell

SEL sres-Nx

Magfac = 1.000e+000

Blue	-2.0653e+002 to 0.0000e+000
Dark Green	0.0000e+000 to 5.0000e+002
Light Green	5.0000e+002 to 1.0000e+003
Yellow-Green	1.0000e+003 to 1.5000e+003
Yellow	1.5000e+003 to 2.0000e+003
Orange	2.0000e+003 to 2.5000e+003
Red	2.5000e+003 to 2.8947e+003

Interval = 5.0e+002

SurfX = (1.00, 0.00, 0.00)

Unit: N/m

Positive=Tension

Negative=Compression

Figure 4.7 Horizontal stress in the geocell (Plate displacement = 10mm)

The load-displacement curves from the numerical models are compared with the test results in Figure 4.8. Overall, the numerical model well simulated the bearing capacities of the unreinforced and geocell-reinforced sand. The calculated stiffness of the geocell-reinforced sand was lower than the test measurement. The reason for this offset may be that the shear dilatancy behavior of the sand caused more volumetric expansion of the sand during the loading, thus the sand inside the geocell received additional lateral confining stress. Such shear dilatancy behavior cannot be simulated by the Duncan-Chang model used in this study.

The tensile strain at the strain gauge location was also extracted from the model. The strain values from the numerical model matched the test measurement well in the Type II and Type III geocell cases, whereas in the Type I geocell case, the numerical model considerably under-predicted the tensile strain in geocell.

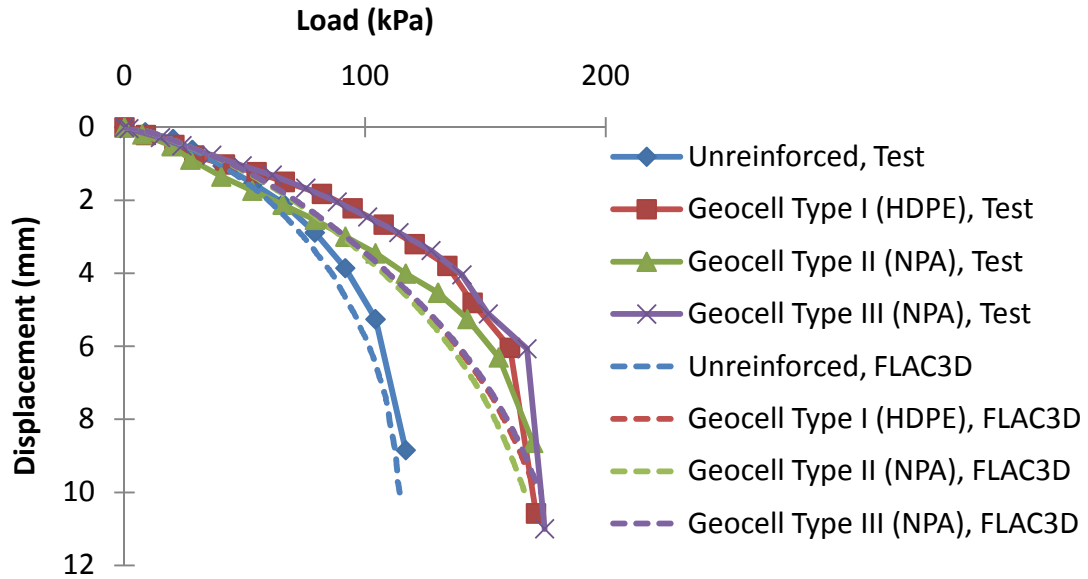


Figure 4.8 Load-displacement curves (Test vs. Numerical results)

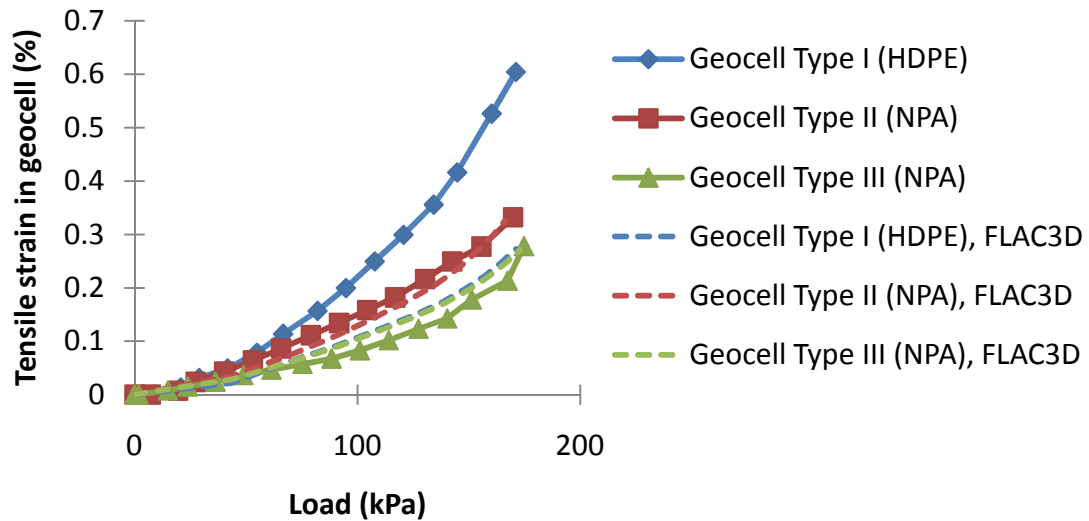


Figure 4.9 Tensile strain on the geocell (Test vs. Numerical results)

4.5 Parametric study

Based on the numerical model created in this study, a parametric study was performed to investigate the behavior of geocell-reinforced sand with underlying clay subgrade. To assist analyzing the wheel load test result in the next chapter, the layer profiles and materials in the road test section 2 constructed in the moving wheel test were used as the baseline model. A steadily increasing (up to the failure of the soil) static load was applied within a rectangular area on top of the soil. The pressure-displacement curves were calculated. Based on the baseline model, variations of parameters were made within reasonable ranges to evaluate the effects of (a) the thickness of the geocell-reinforced sand layer, (b) the modulus of the geocell, (c) the geocell-soil interface shear modulus, and (d) the stiffness of the subgrade.

4.5.1 Unreinforced and reinforced bases

Due to the symmetry of the problem, one quarter of the model was created in FLAC3D (as shown in Figure 4.10). The boundary conditions included the vertical displacement (along the z direction) fixed at the bottom boundary and lateral displacements (along the x and y directions) fixed at the four side-boundaries. A steadily increasing static load was applied within the rectangular area of 0.145m×0.125m as shown in Figure 4.10. It should be noted that the actual contact area of tires on a road surface is not rectangular. The rectangular

loading area was selected in this study to approximate the actual shape of the contact area. The increment of each load was 20 kPa. For a comparison purpose, an unreinforced case, with the same pavement structure as shown in Figure 4.10 but without geocell, was also modeled. The geocell pockets were modeled in a diamond shape, which is more appropriate than a sine curve for a multi-cell situation.

The constitutive models and parameters of the materials are summarized in Table 4.3. All the material parameters were determined from laboratory tests described in Chapter 3, except that the Young's modulus of AB-3 was estimated by typical value of 40MPa.

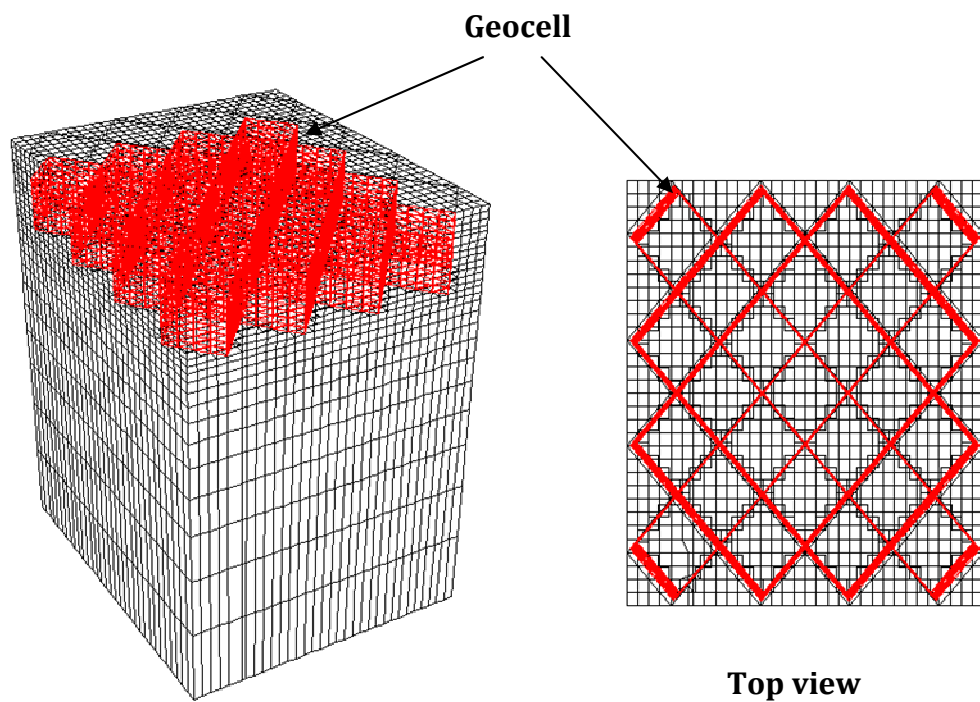
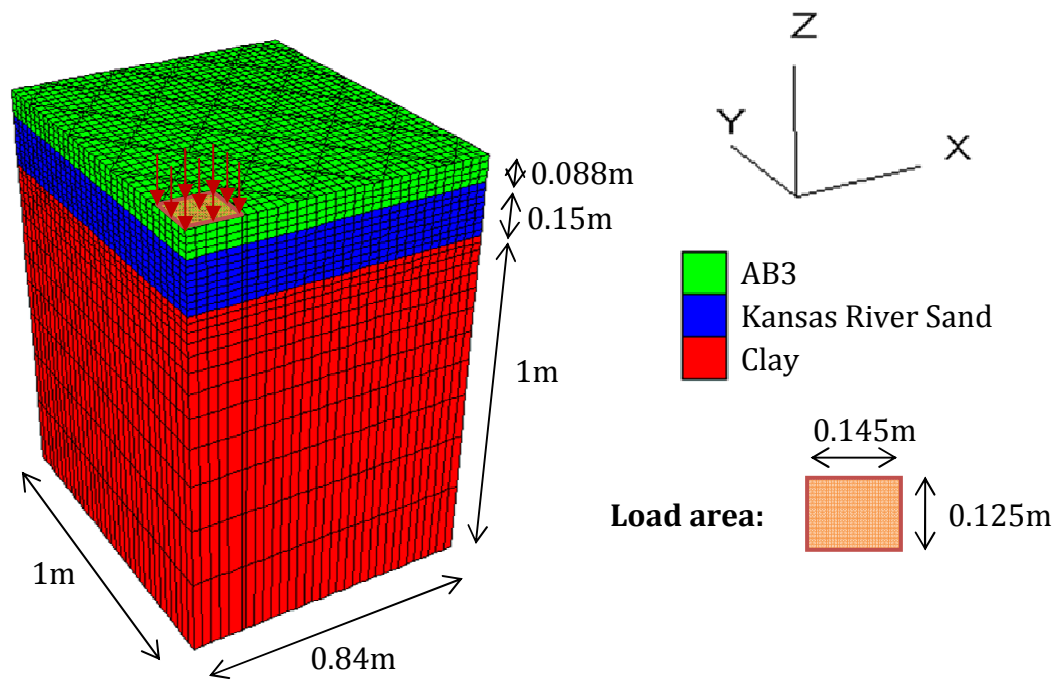


Figure 4.10 Numerical mesh of the baseline model

Table 4.3 Constitutive models and parameters used in the baseline model

AB-3 (Thickness=0.088m)			
Mohr-Coulomb model			
Parameters	Symbol	Unit	Values
Young's modulus	E	MPa	40
Poisson's ratio	ν	--	0.35
Cohesion	c	kPa	4.7
Friction angle	ϕ	Degree	47.2
Unit weight	γ	kN/m ³	22.3
Kansas River sand (Thickness=0.15m)			
Duncan-Chang model			
Parameters	Symbol	Unit	Values
Cohesion	c	kPa	0
Initial friction angle	ϕ_0	Degree	41.1
Friction angle parameter	$\Delta\phi$	Degree	0
Initial bulk modulus	B_i	kPa	3708
Asymptotic volumetric strain	ε_u	--	0.011
Failure ratio	R_f	--	0.66
Modulus number	K	--	561
Modulus exponent	n	--	0.53
Unit weight	γ	kN/m ³	17.9
Clay (Thickness=1m)			
Mohr-Coulomb model			
Parameters	Symbol	Unit	Values
Young's modulus	E	MPa	10.3
Poisson's ratio	ν	--	0.35
Cohesion	c	kPa	104.6
Friction angle	ϕ	Degree	0
Unit Weight	γ	kN/m ³	19.5
Geocell (Height=0.15m)			
Elastic plate model			
Parameters	Symbol	Unit	Values
Young's modulus	E	MPa	420
Poisson's ratio	ν	--	0.45
Interface shear modulus	k_i	MPa/m	19.7
Interface cohesion	c_i	kPa	0
Interface friction angle	ϕ_i	Degree	41.6
Thickness of the geocell	R_f	mm	1.1

The pressure-displacement curves of the unreinforced and geocell-reinforced cases are shown in Figure 4.11. The numerical result shows that geocell-reinforcement can significantly increase the bearing capacity of the road. At 20mm displacement, the bearing capacity of the unreinforced road reached 560kPa, while the bearing capacity of the reinforced road reached 800kPa. This result explains why the unreinforced sand base was not stable under a 550kPa moving wheel load. With geocell reinforcement, the stiffness of the unpaved road was also increased, but such an effect started only after about 5mm vertical displacement developed on top of the road.

Figure 4.12 shows the horizontal displacement contours of the unreinforced and reinforced sections. It is clearly shown that geocell has a significant effect in restraining lateral displacement of the infill soil. Without geocell-reinforcement, the maximum horizontal displacement occurred within the sand layer. With geocell-reinforcement, the maximum horizontal displacement occurred at the top of the subgrade. Under a higher vertical load (1060kPa) on top the road, the maximum horizontal displacement developed in the reinforced section was still less than that developed in the unreinforced section.

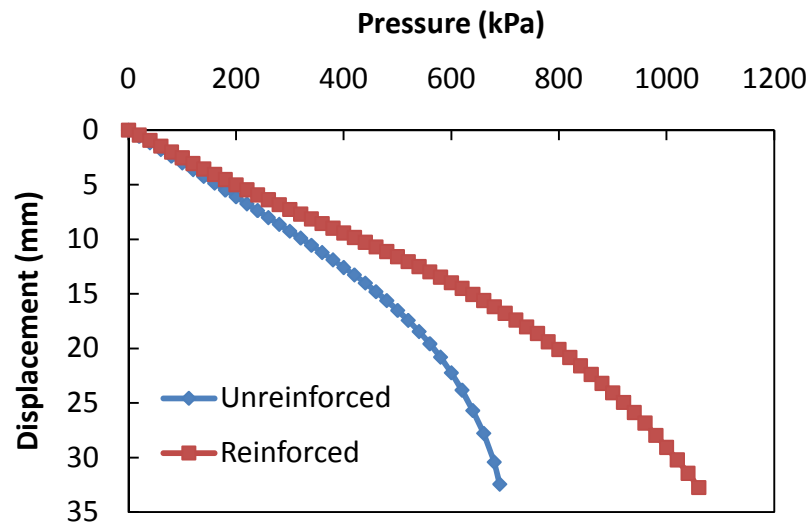
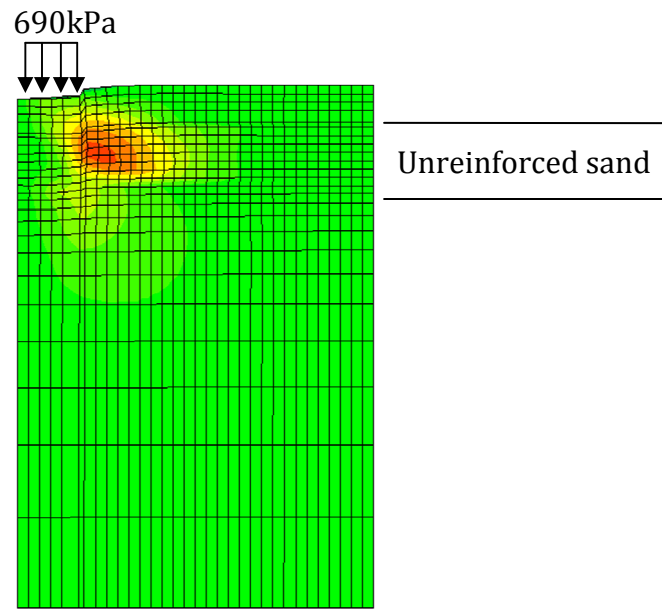
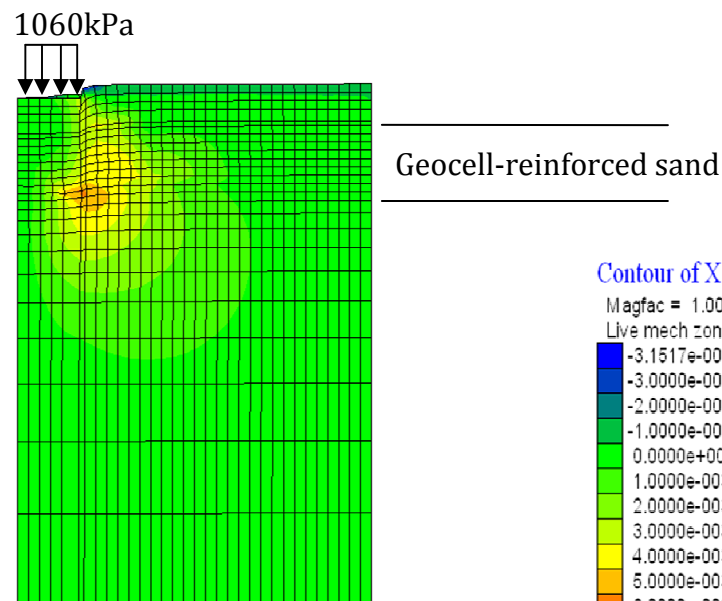


Figure 4.11 Pressure-displacement curves of unreinforced vs. reinforced sand



(a) Unreinforced



(b) Reinforced

Figure 4.12 Horizontal displacement contours

4.5.2 Effect of the thickness of the geocell-reinforced sand layer

Based on the baseline case illustrated in Figure 4.10 and Table 4.3, the thickness of the geocell-reinforced sand layer was changed to 10mm (approximately corresponding to Section 3 in the moving-wheel test) and 20mm. The pressure-displacement curves from the numerical analyses are plotted together in Figure 4.13. It is shown that the thickness of the geocell-reinforced sand layer has a minor effect on the bearing capacity of the road. This result is understandable because, in this particular case, relatively poor base material was placed on a firm subgrade. Shear failure occurred within the base sand layer rather than in the subgrade clay.

However, a thinner geocell-reinforced layer is expected to result in higher horizontal tensile stresses in the geocell. The numerical analyses showed that the maximum horizontal tensile stresses developed in the geocell was 2.30, 2.63, and 2.87kN/m with 20, 15, and 10cm thick geocell-reinforced sand, respectively. A higher tensile load in geocell would cause the premature failure of the joints of the geocell. Currently, due to the lack of a standard definition or test method for the joint strength of the geocell, this information is unavailable from most geocell manufacturers. Thus this failure mode was not considered in the model.

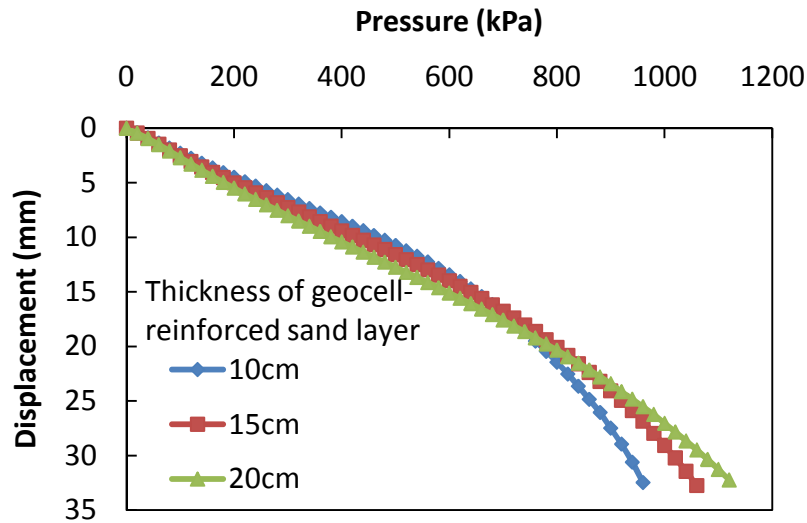


Figure 4.13 Effect of the thickness of geocell-reinforced sand on pressure-displacement curves

4.5.3 Effect of the modulus of the geocell

Based on the baseline case illustrated in Figure 4.10 and Table 4.3, the modulus of the geocell was changed to one-fourth of its original modulus (i.e., 105MPa) and four times its original modulus (i.e., 1680MPa). The pressure-displacement curves from the numerical analyses are plotted together in Figure 4.14. It is shown that the bearing capacity of the reinforced base increased significantly with an increase in the elastic modulus of the geocell. This result is expected because geocell with a higher elastic modulus can provide more confining stress to the infill granular soil under the same lateral deformation. The additional confining stress will increase the modulus and the shear strength of the granular soil.

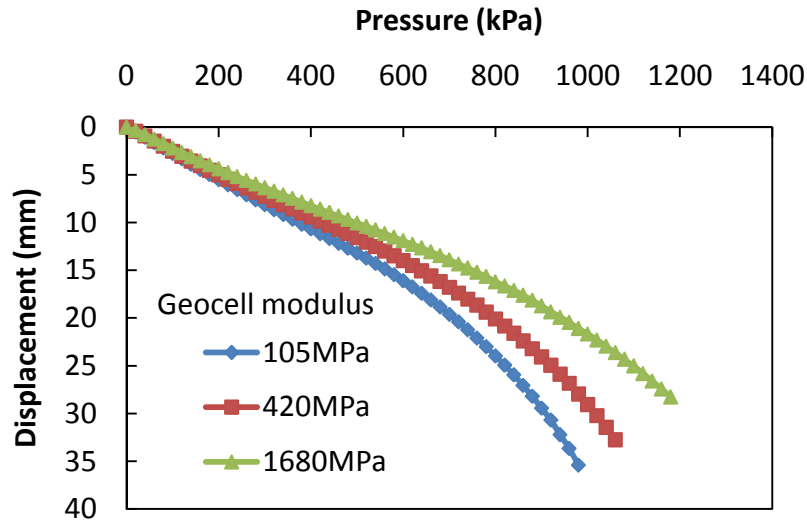


Figure 4.14 Effect of geocell modulus on pressure-displacement curves

4.5.4 Effect of the geocell-soil interface shear modulus

Based on the baseline case illustrated in Figure 4.10 and Table 4.3, the geocell-soil interface shear modulus of the geocell was changed to one-tenth (i.e., 1.97MPa/m) of its original value and 10 times its original value (i.e., 197MPa/m). The pressure-displacement curves from the numerical analyses are plotted together in Figure 4.15. It is shown that the geocell-soil interface shear modulus had almost no influence on the bearing capacity of the reinforced soil. This result was based on the fact that a geocell-reinforced base was over a firm subgrade. When the subgrade is soft, the interface shear modulus may become important and a further study is needed to verify this effect. With a firm subgrade, the primary mechanism of the geocell reinforcement is lateral

confinement. This is different from planar geosynthetic products (geogrid and geotextile), of which the reinforcing effect relies on the friction between the soil and the geosynthetics.

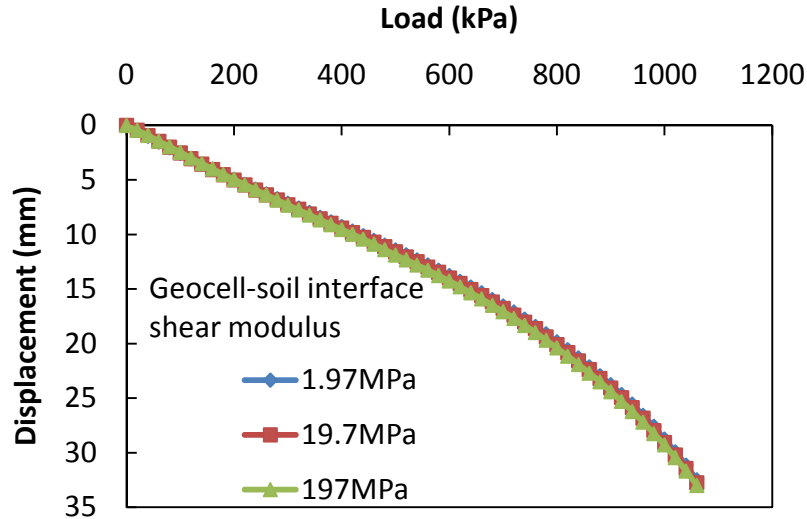


Figure 4.15 Effect of geocell-soil interface shear modulus on pressure-displacement curves

4.5.5 Effect of the type of subgrade

Based on the baseline case illustrated in Figure 4.10 and Table 4.3, the Young's modulus and shear strength of the subgrade clay were changed to half of their original values (i.e., $E=5.15\text{MPa}$ and $c=52.3\text{kPa}$) to simulate a relatively soft subgrade. The pressure-displacement curves from the numerical analyses are plotted together in Figure 4.16. As expected, when soft subgrade was present, the bearing capacity decreased in both unreinforced and reinforced sections. It

is interesting to notice that the reinforced section with soft subgrade behaved similarly to the unreinforced section with firm subgrade. Such a result demonstrates geocell-reinforcement on the top of a relatively soft subgrade can achieve an equivalent performance to that of the unreinforced soil on top of a stiff subgrade. However, this numerical result is only applicable to the particular layer thickness, soil type, and geocell product used in this study. A future study is needed to develop an analytical model to predict the bearing capacity of geocell-reinforced soils.

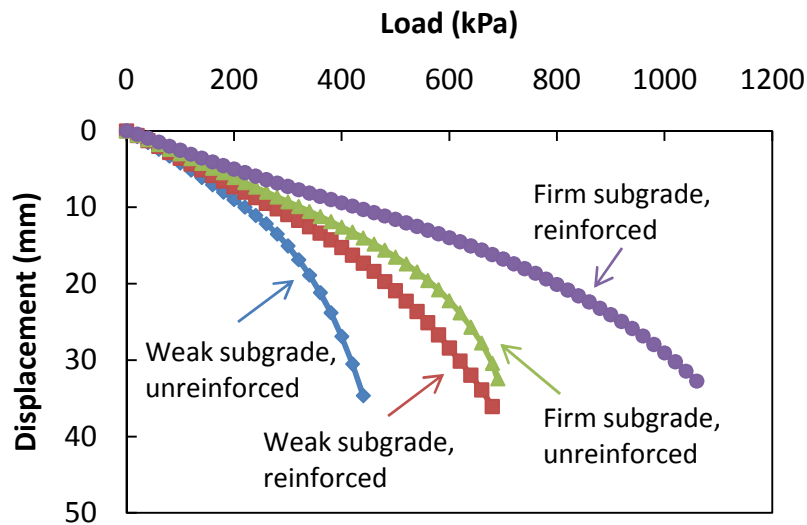


Figure 4.16 Effect of subgrade soil on pressure-displacement curves

4.6 Summary

This chapter describes the development of a numerical model for geocell-reinforced granular soil under a static load. In this model, the infill soil was modeled using the Duncan-Chang model, and the geocell was modeled using a

linear elastic plate model. This numerical model was validated using the laboratory load test conducted on single-geocell-reinforced sand. A parametric study was conducted based on the validated model. Some conclusions can be drawn from this part of study:

- (1) With the geocell and the infill granular soil modeled separately, the numerical model developed in this study can simulate some key features in the performance of the geocell-reinforced soil, such as the increased confining stress and the restrained lateral displacement of the soil.
- (2) For the particular case modeled in the parametric study, the bearing capacity of the road was greatly improved (by about 43%) with the inclusion of geocell. The stiffness of the soil was also increased, but the benefit started to exhibit after about 5mm displacement was developed on the top surface. This result is consistent with the static load test data obtained from the geocell-reinforced sand.
- (3) The parametric study also showed that on firm subgrade the thickness of geocell-reinforced soil layer had a minor effect on the bearing capacity of the road.
- (4) Based on the parametric study, the Young's modulus of the geocell material was the most important parameter of geocell that influenced the performance of geocell-reinforced soil under a static load. The geocell-soil interface shear modulus had almost no impact on the behavior of geocell-reinforced soil when a firm subgrade exists.

- (5) The numerical results by varying the subgrade modulus and strength showed that geocell-reinforcement on the top of a relatively soft clay subgrade could achieve an equivalent performance to the unreinforced soil on the top of a stiff subgrade.

Chapter 5 Numerical analysis of geocell-reinforced soil under a repeated load

5.1 Overview

In this chapter, numerical modeling of the behavior of geocell-reinforced soil under a repeated load was investigated. The numerical model created in this chapter was based on the mechanistic-empirical pavement design model developed in the NCHRP project 1-37A (NCHRP 2004). Modifications were made in order to incorporate geocell reinforcement into the mechanistic-empirical model. Three-dimensional mechanistic response model was used due to the complex geometry of geocell. The compaction-induced lateral earth pressure was considered in the initial stress distribution in the response model. The residual horizontal stress in the soil due to the deformation of geocell was also considered. The numerical model was used to simulate the moving-wheel tests described in Chapter 3.

5.2 Mechanistic-empirical model for geocell-reinforced soil

As introduced in the literature review, the mechanistic-empirical model has been accepted in the current pavement design method in the United States. The model utilizes two components, a response model and a damage model, to predict pavement distresses (rutting and fatigue crack). To consider the stress-

dependency of the soil, a finite element response model can be used to predict resilient strains in the pavement structure. A damage model is a series of empirical relations that correlate the resilient strains at different locations in the pavement structure to different types of distresses. For unpaved roads, rutting is the major type of distress.

As of today, geosynthetic-reinforced road bases have not been included in the mechanistic-empirical design method. To incorporate geocell design into the mechanistic-empirical model, some issues must be first addressed:

- (1) The finite element response model in the NCHRP project 1-37A was an axisymmetric model. It is difficult to simulate the behavior of the geocell-reinforced soil in an axisymmetric model due to the complex three-dimensional geometry of geocell. To create a three-dimensional numerical model, the formula of the tangent resilient modulus (Equation 2.17) must be re-derived to consider the effect of the intermediate principal stress σ_2 .
- (2) Geocell reinforcement cannot be simulated by simply including structure elements in to the finite element model. As Perkins (2004) pointed out in his study on geogrid-reinforced roadway bases, the initial stress increase in the reinforced soil due to the compaction effort and the residual stress accumulated in the soil due to the presence of the geosynthetics must be properly considered.

(3) The empirical damage model in the current mechanistic-empirical model was calibrated based on the field data collected from paved roads. It was assumed that the pavement would finally “shakedown” to a stable state. For unpaved road, however, such an assumption may lead to inadequate design. The bearing capacity failure of the road must be considered.

5.2.1 Three-dimensional tangent resilient modulus model

As discussed in Chapter 2, resilient modulus M_r measured from a cyclic triaxial test is the secant modulus when the stress of the soil element transits from the hydrostatic state ($\sigma_1 = \sigma_3$) to the maximum stress state ($\sigma_1 > \sigma_3$) while σ_3 remains unchanged. In this case, the tangent resilient modulus can be derived as Equation 2.17.

Now consider a more general case where the intermediate stress σ_2 is also cycling (like in a cyclic true triaxial test). Then the resilient modulus M_r can be considered as the secant modulus when the stress of the soil element transits from the hydrostatic state ($\sigma_1 = \sigma_2 = \sigma_3$) to the maximum stress state ($\sigma_1 > \sigma_2 > \sigma_3$) while σ_3 remains unchanged. From the generalized form of Hooke’s Law,

$$\Delta\varepsilon_1 = \frac{1}{M_r} [\Delta\sigma_1 - \nu(\Delta\sigma_2 + \Delta\sigma_3)] \quad 5.1$$

Substitute $\Delta\sigma_1 = \sigma_1 - \sigma_3$, $\Delta\sigma_2 = \sigma_2 - \sigma_3$, and $\Delta\sigma_3 = 0$, Equation 5.1 can be written as

$$\Delta\varepsilon_1 = \frac{1}{M_r} [\sigma_1 - \sigma_3 - \nu(\sigma_2 - \sigma_3)] \quad 5.2$$

or

$$M_r = \frac{1}{\Delta\varepsilon_1} [\sigma_1 - \sigma_3 - \nu(\sigma_2 - \sigma_3)] \quad 5.3$$

The tangential form of Equation 5.3 can be written as

$$E_t = \frac{d[\sigma_1 - \sigma_3 - \nu(\sigma_2 - \sigma_3)]}{d\varepsilon_1} = \frac{d\sigma_1 - \nu d\sigma_2}{\frac{\partial \varepsilon_1}{\partial \sigma_1} d\sigma_1 + \frac{\partial \varepsilon_1}{\partial \sigma_2} d\sigma_2} \quad 5.4$$

where $\frac{\partial \varepsilon_1}{\partial \sigma_1}$ and $\frac{\partial \varepsilon_1}{\partial \sigma_2}$ can be derived from Equation 5.2 as

$$\begin{aligned} \frac{\partial \varepsilon_1}{\partial \sigma_1} &= \frac{1}{M_r} - \frac{[\sigma_1 - \sigma_3 - \nu(\sigma_2 - \sigma_3)]}{M_r^2} \cdot \frac{dM_r}{d\sigma_1} \\ \frac{\partial \varepsilon_1}{\partial \sigma_2} &= \frac{\nu}{M_r} - \frac{[\sigma_1 - \sigma_3 - \nu(\sigma_2 - \sigma_3)]}{M_r^2} \cdot \frac{dM_r}{d\sigma_2} \end{aligned} \quad 5.5$$

where $\frac{dM_r}{d\sigma_1}$ and $\frac{dM_r}{d\sigma_2}$ can be derived from Equation 2.16 as

$$\begin{aligned}\frac{dM_r}{d\sigma_1} &= M_r \left[\frac{k_2}{\theta} + \frac{k_3(2\sigma_1 - \sigma_2 - \sigma_3)}{9\tau_{oct}(\tau_{oct} + p_a)} \right] \quad (\tau_{oct} \neq 0) \\ \frac{dM_r}{d\sigma_2} &= M_r \left[\frac{k_2}{\theta} + \frac{k_3(2\sigma_2 - \sigma_1 - \sigma_3)}{9\tau_{oct}(\tau_{oct} + p_a)} \right] \quad (\tau_{oct} \neq 0)\end{aligned}\tag{5.6}$$

where p_a is the atmospheric pressure, k_2 and k_3 are dimensionless parameters, θ is the bulk stress, and τ_{oct} is the octahedral shear stress.

$$\begin{aligned}\theta &= \sigma_1 + \sigma_2 + \sigma_3 \\ \tau_{oct} &= \frac{\sqrt{(\sigma_1 - \sigma_2)^2 + (\sigma_2 - \sigma_3)^2 + (\sigma_1 - \sigma_3)^2}}{3}\end{aligned}\tag{5.7}$$

Note that Equation 5.6 is valid unless $\tau_{oct} = 0$, which means the stress state of the element remains unchanged ($\sigma_1 = \sigma_2 = \sigma_3$). In such case, the secant modulus and the tangent modulus are the same ($E_t = M_r$).

To eliminate $d\sigma_1$ and $d\sigma_2$ in Equation 5.4, the ratio of $\frac{d\sigma_1}{d\sigma_2}$ is required. FLAC^{3D} utilizes a finite difference method to solve initial and boundary value problems. For a given problem, the equilibrium of the model is achieved by iteration. At each iteration step, a small strain increment (determined automatically by the program) is applied to each zone of the model to obtain the new stress tensor. Thus it can be assumed that the stress increment of each zone in a single iteration step is also small. In such a case, $d\sigma_1/d\sigma_2$ can be approximated by:

$$\frac{d\sigma_1}{d\sigma_2} \approx \frac{\Delta\sigma_1}{\Delta\sigma_2} = \frac{\sigma_1 - \sigma_3}{\sigma_2 - \sigma_3} \quad 5.8$$

Substitute Equations 5.6, 5.7, and 5.8 into Equation 5.4. The general three-dimensional form of the tangent resilient modulus can be written as:

$$E_t = \begin{cases} \frac{M_r}{1 - (\sigma_1 - \sigma_3) \left[\frac{k_2}{\theta} + \frac{k_3(2\sigma_1 - \sigma_2 - \sigma_3)}{9\tau_{oct}(\tau_{oct} + p_a)} \right] - (\sigma_2 - \sigma_3) \left[\frac{k_2}{\theta} + \frac{k_3(2\sigma_2 - \sigma_1 - \sigma_3)}{9\tau_{oct}(\tau_{oct} + p_a)} \right]}, & \tau_{oct} \neq 0 \\ M_r, & \tau_{oct} = 0 \end{cases} \quad 5.9$$

When $\sigma_2 = \sigma_3$, Equation 5.9 can be simplified to Equation 2.17, which is reasonable because an axi-symmetric model is a special case of the general three dimensional model.

The constitutive equations derived above were programmed in C++ and compiled into a DLL file, which was incorporated into FLAC^{3D}.

5.2.2 Initial horizontal stress increase due to compaction effort

It is well known that compaction induces horizontal earth pressure increase within a certain influence depth. The increased horizontal stress, as realized by many researchers, can significantly increase the stiffness of the granular base layer. However, the compaction-induced horizontal stress has not been considered in the finite element response model in the current mechanistic-empirical design guide (NCHRP 2004).

In order to estimate the compaction-induced horizontal earth pressure, Duncan and Seed (1986) proposed a general hysteretic K_0 -loading model. This model suggests that when a compaction load is applied, the stress state of the soil moves along the K_0 -line (from point A to point B in Figure 5.1), which is defined in Equation 5.10.

$$\sigma'_h = K_0 \sigma'_v \quad 5.10$$

where σ'_h and σ'_v are the effective stresses in horizontal and vertical directions respectively; K_0 is the coefficient of lateral earth pressure at rest. For normally consolidated granular soils, K_0 can be estimated from the friction angle ϕ of the soil.

$$K_0 = 1 - \sin \phi \quad 5.11$$

When the compaction load is removed, both vertical and horizontal stresses in the soil decrease. In this stage, the stress state of the soil follows the unloading-line (from point B to point C in Figure 5.1). The unloading-line of the soil is defined in Equation 5.12.

$$\begin{aligned} \sigma'_h &= K'_0 \sigma'_v \\ K'_0 &= K_0 OCR^\alpha \end{aligned} \quad 5.12$$

where K_0' is the coefficient of lateral earth pressure during unloading; OCR is the overconsolidation ratio; and α is the unloading coefficient, which can be estimated from the friction angle ϕ of the soil as shown in Figure 5.2.

For the unreinforced soil, the horizontal stress cannot exceed the passive earth pressure (or above K_1 -line), as the stress path of the soil illustrated by the curve ABCD in Figure 5.1. For a geocell-reinforced soil, it can be assumed that the residual horizontal stress in the soil can exceed the passive earth pressure because the geocell structure stabilizes the soil from the passive failure (see Figure 5.3). With this modification, the stress path of the geocell-reinforced soil during compaction follows the curve ABCE in Figure 5.1.

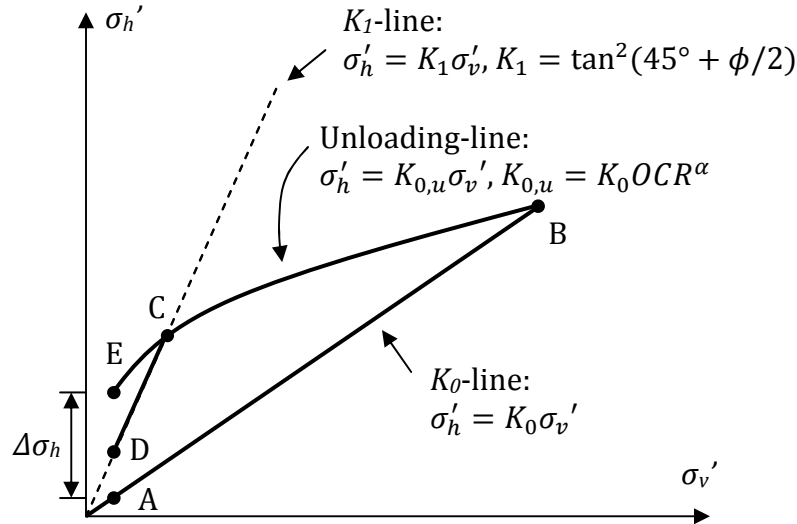


**Figure 5.1 Modified general hysteretic K_0 -loading model
(modified from Duncan and Seed, 1986)**

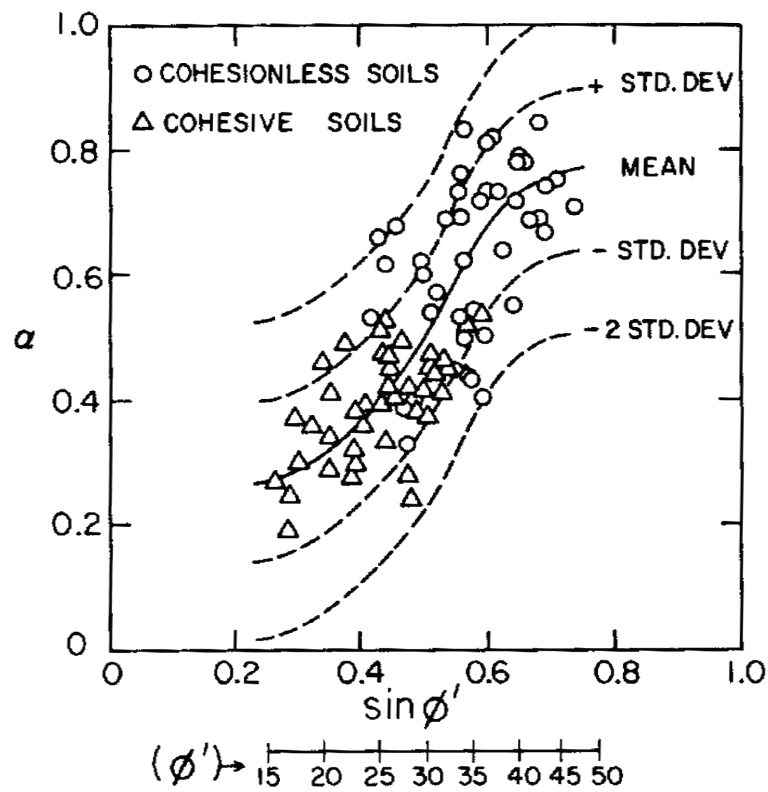


Figure 5.2 Suggested relationship between α and ϕ' (Duncan and Seed 1986)

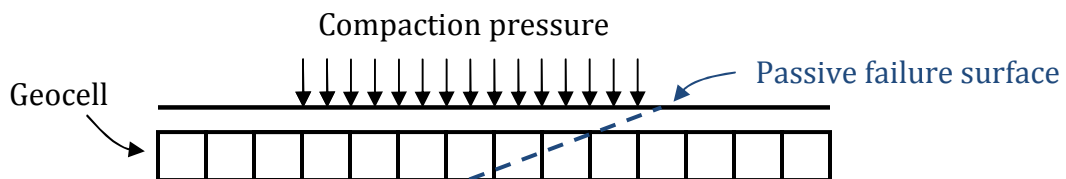


Figure 5.3 Geocell stabilizes the passive earth failure

Since the geocell reinforced layer is often compacted right after the infill material is placed, the compaction-induced vertical stress in the base layer can be approximated by the compaction pressure. Thus the compaction-induced initial horizontal stresses can be calculated at different depths of the reinforced and unreinforced pavement layers. Five parameters are needed in this method: the unit weight γ of the soil, the cohesion c of soil, the internal friction angle ϕ' of the soil, the unloading coefficient α , and the compaction pressure.

In the moving wheel road test performed in this study, the road sections are compacted using a 10.3-ton compactor with a drum width of 2.13m. The compaction pressure was estimated as 338kPa. With the above-mentioned method the calculated compaction-induced initial horizontal stresses at different depths in the base layer of each test section is shown in Figure 5.4 and Figure 5.5. In this study, the initial horizontal stresses in the subgrade layer were set as those in a K_0 condition, because clay is generally considered as a less stress-dependent material.

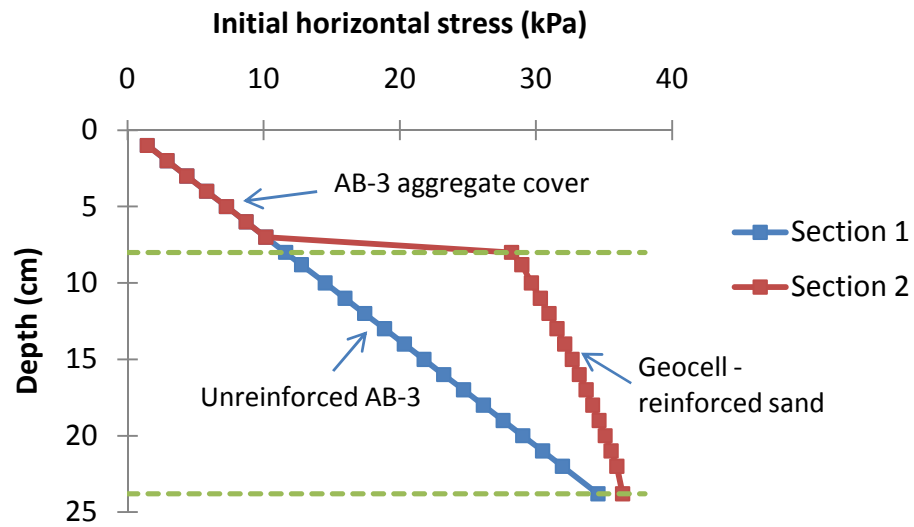


Figure 5.4 Initial horizontal stress after compaction in Section 1 and 2

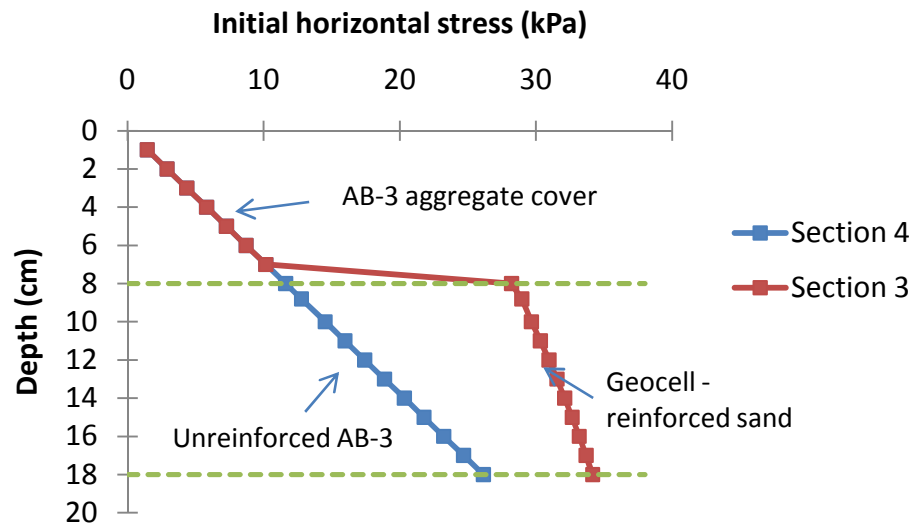


Figure 5.5 Initial horizontal stress after compaction in Section 3 and 4

5.2.3 Residual stress accumulated in the infill soil

As the number of wheel passes increases, permanent deformation accumulates in both soil and geocell. The permanent lateral expansion of the geocell provides additional horizontal confining stress to the infill material. This additional horizontal stress in the soil finally approaches a constant value $\Delta\sigma_3$ (also called a residual stress) when the pavement shakedown to the resilient state. The residual stress increases the resilient modulus of the geocell-reinforced soil. Thus it is important to consider the residual stress when modeling the pavement response. In a numerical response model, the residual stress in the geocell-reinforced soil should be determined and applied to the model as the initial stress.

To determine the effect of geocell reinforcement on the resilient modulus of the infill soil, Mengelt et al. (2000) performed cyclic triaxial tests on single cell-reinforced soil samples. However, such a test is difficult to perform because the cell geometry (diameter and height) varies from product to product and often does not fit the test equipment. In the following paragraphs, an analytical solution for the behavior of single cell-reinforced soil under a cyclic triaxial test is derived.

The damage model currently accepted in the mechanistic-empirical pavement design guide is based on Tseng and Lytton's (1989) model (Equation 5.13):

$$\frac{\varepsilon_{1,p}}{\varepsilon_{1,r}} = \left(\frac{\varepsilon_0}{\varepsilon_r}\right) e^{-\left(\frac{\rho}{N}\right)^\beta} \quad 5.13$$

where $\left(\frac{\varepsilon_0}{\varepsilon_r}\right)$, ρ , and β are the parameters that can be determined from cyclic triaxial tests. In the cyclic triaxial tests, when the soil shakedown to a stable condition ($N \rightarrow \infty$), the ratio of permanent strain to resilient strain is

$$\lim_{N \rightarrow \infty} \frac{\varepsilon_{1,p}}{\varepsilon_{1,r}} = \left(\frac{\varepsilon_0}{\varepsilon_r}\right) \quad 5.14$$

Imagine a cylinder-shaped single cell-reinforced soil sample is subjected to a constant confining stress of σ_3 and a maximum cyclic axial stress of σ_1 . After a large number of cycles of loading and unloading ($N \rightarrow \infty$), the sample will develop both permanent axial deformation $\varepsilon_{1,p}$ and permanent radial deformation $\varepsilon_{3,p}$. Meanwhile, the geocell will expand horizontally together with the infill soil and provide additional confining stress $\Delta\sigma_3$ to the soil. When the sample reaches the resilient state, the total confining stress experienced by the soil will be $(\sigma_3 + \Delta\sigma_3)$, as shown in Figure 5.6(b). For comparison purpose, Figure 5.6(a) illustrates the stress state of an unreinforced soil sample in a cyclic triaxial test.

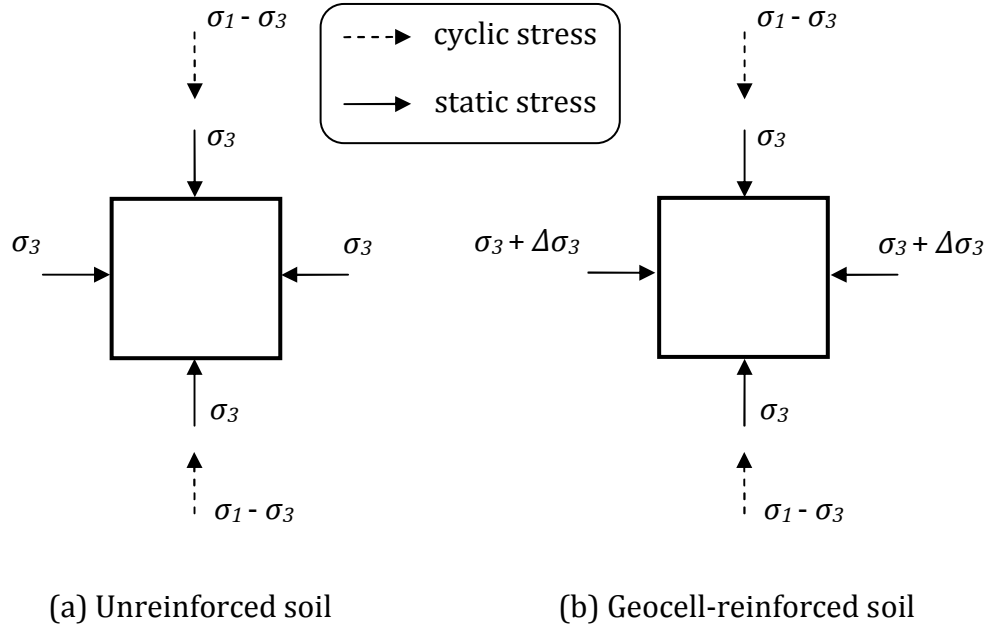


Figure 5.6 The stress state of the soil in a cyclic triaxial test after the sample reaches the resilient state

The resilient stress-strain response of the unreinforced soil sample (see Figure 5.6(a)) can be expressed by the following equations:

$$\varepsilon_{1,r} = \frac{\sigma_1 - \sigma_3}{M_r} \quad 5.15$$

$$M_r = k_1 p_a \left(\frac{\theta}{p_a} \right)^{k_2} \left(\frac{\tau_{oct}}{p_a} + 1 \right)^{k_3} \quad 5.16$$

where

$$\theta = \sigma_1 + 2\sigma_3 \quad 5.17$$

$$\tau_{oct} = \frac{\sqrt{2}}{3} (\sigma_1 - \sigma_3)$$

The resilient stress-strain response of the geocell-reinforced sample is more complicated than that of the unreinforced soil sample. Since the resilient modulus determined by Equation 5.16 is the secant modulus from a hydrostatic state to another stress state with the increased σ_1 , the resilient response of the geocell-reinforced samples must be divide into two consequent stages:

- (1) The axial stress increases from σ_3 to $\sigma_3 + \Delta\sigma_3$. The resilient modulus in this stage $M_{r,1}$ can be determined by Equation 5.16 with

$$\begin{aligned}\theta &= \sigma_3 + 2(\sigma_3 + \Delta\sigma_3) = 3\sigma_3 + 2\Delta\sigma_3 \\ \tau_{oct} &= \frac{\sqrt{2}}{3} \Delta\sigma_3\end{aligned}\tag{5.18}$$

- (2) The axial stress continues to increase from $\sigma_3 + \Delta\sigma_3$ to σ_1 . The resilient modulus in this stage $M_{r,2}$ can be determined by Equation 5.16 with

$$\begin{aligned}\theta &= \sigma_1 + 2(\sigma_3 + \Delta\sigma_3) \\ \tau_{oct} &= \frac{\sqrt{2}}{3} [\sigma_1 - (\sigma_3 + \Delta\sigma_3)]\end{aligned}\tag{5.19}$$

Thus, the resilient strain of the geocell reinforced sample can be derived as

$$\varepsilon_{1,r} = \frac{\Delta\sigma_3}{M_{r,1}} + \frac{\sigma_1 - (\sigma_3 + \Delta\sigma_3)}{M_{r,2}}\tag{5.20}$$

The hoop stress from the geocell to the infill soil can be estimated by:

$$\Delta\sigma_3 = \frac{2M}{D} \cdot (-\varepsilon_{3,p}) = \frac{M}{D} \cdot \varepsilon_{1,p} \quad 5.21$$

assuming that (1) both sample and the membrane deform as a right cylinder under the compressive stress, and (2) the soil and the membrane are both incompressible ($\nu = 0.5$).

Substitute Equation 5.14 into Equation 5.21.

$$\Delta\sigma_3 = \frac{M}{D} \left(\frac{\varepsilon_0}{\varepsilon_r} \right) \varepsilon_{1,r} \quad 5.22$$

In road construction, the granular base course materials are often compacted to a higher relative density, e.g., 95% of the maximum density. Granular materials in this state often show shear-dilatancy behavior. In this case, the soil will “expand” when the vertical load increases, which can generate additional confining stress. In another word, the assumption of constant volume made here will lead to a conservative estimation of $\Delta\sigma_3$. The shear-dilatancy behavior of soil can be characterized by dilation angle ψ , which is defined as

$$\tan \psi = -\frac{\delta\varepsilon_v}{\delta\gamma} \quad 5.23$$

The dilation angle can be determined from triaxial compression tests by monitoring the volumetric strain ε_v and the axial strain ε_1 during the test:

$$\sin \psi = \frac{\frac{\varepsilon_v}{\varepsilon_1}}{\frac{\varepsilon_v}{\varepsilon_1} - 2} = \frac{\varepsilon_v}{\varepsilon_v - 2\varepsilon_1} = \frac{\varepsilon_1 + 2\varepsilon_3}{\varepsilon_1 + 2\varepsilon_3 - 2\varepsilon_1} = \frac{\varepsilon_1 + 2\varepsilon_3}{-\varepsilon_1 + 2\varepsilon_3} \quad 5.24$$

Equation 5.24 can be re-arranged as:

$$-\frac{2\varepsilon_3}{\varepsilon_1} = \frac{1 + \sin \psi}{1 - \sin \psi} \quad 5.25$$

So, if the shear-dilatancy of soil is considered, Equation 5.21 and Equation 5.22 can be updated respectively as follows:

$$\Delta\sigma_3 = \frac{2M}{D} \cdot (-\varepsilon_{3,p}) = \frac{M}{D} \cdot \varepsilon_{1,p} \cdot \frac{1 + \sin \psi}{1 - \sin \psi} \quad 5.26$$

$$\Delta\sigma_3 = \frac{M}{D} \left(\frac{\varepsilon_0}{\varepsilon_r} \right) \varepsilon_{1,r} \cdot \frac{1 + \sin \psi}{1 - \sin \psi} \quad 5.27$$

Note that when shear-dilatancy is neglected, Equation 5.26 and Equation 5.27 will reduce to Equation 5.21 and Equation 5.22.

Substituting Equation 5.20 into Equation 5.27, $\Delta\sigma_3$ then becomes the only unknown variable on both sides of Equation 5.27 thus can be solved by iterations.

The analytical solution derived above can be used to estimate the behaviors of a single cell-reinforced soil sample under a cyclic triaxial test, including (1) the resilient modulus of the geocell-soil composite, (2) the residual tensile stress in the geocell, and (3) the residual horizontal stress in the soil. Factors like soil properties, geocell stiffness, cell height and diameter, stress level are all considered in this solution.

The only available test data that can be used to verify this solution is from the resilient modulus tests conducted by Mengelt et al. (2000) on unreinforced and geocell-reinforced soil samples. These resilient modulus tests were conducted following the standard AASHTO T-294 94. Of all the resilient test data reported by Mengelt et al.'s (2000), the test data from the Rodefeld sand and the Antigo silt loam were used in the verification. Table 5.1 lists all the input parameters for the calculation. The resilient modulus parameters (k_1 , k_2 , and k_3) are calibrated from the resilient modulus tests on the unreinforced samples. Although the permanent strain accumulation data in the first 1000-cycle conditioning period were not included in the original report, the curve fitting parameter (I and S) based on VESYS correlation were presented by Mengelt et al. (2000). These fitted curves were used to calibrate the permanent deformation parameters ($\left(\frac{\epsilon_0}{\epsilon_r}\right)$, ρ , and β) for the unreinforced soils.

Using the above-presented analytical method, the resilient modulus test data at each load sequence were re-calculated for the unreinforced and reinforced samples. The calculated results are compared with the test data in Table 5.2 for Rodefeld sand and Table 5.3 for Antigo silt loam. The measured and calculated relationships between resilient modulus M_r and bulk stress θ for Lodefeld sand are plotted respectively in Figure 5.7 and Figure 5.8. The measured and calculated relationships between resilient modulus M_r and confining stress σ_3 for the Antigo silt loam are plotted respectively in Figure 5.9 and Figure 5.10. The comparison shows that the calculated resilient moduli matched well with the test data (also shown in Figure 5.11 and Figure 5.12).

The calculated residual stresses in the soil when the soil reached the resilient state at each load sequence were also presented in Table 5.2 for Rodefeld sand and Table 5.3 for Antigo silt loam.

Table 5.1 Material parameters from Mengelt et al. (2000)

Input					
Infill soil: Rodefeld sand					
Resilient modulus parameters			Permanent deformation parameters		
k_1	k_2	k_3	$\left(\frac{\varepsilon_0}{\varepsilon_r}\right)$	ρ	β
433	0.57	-0.01	15.09	3.35×10^3	0.120
Infill soil: Antigo silt loam compacted at 2% dry of optimum water content					
Resilient modulus parameters			Permanent deformation parameters		
k_1	k_2	k_3	$\left(\frac{\varepsilon_0}{\varepsilon_r}\right)$	ρ	β
397	0.49	-1.24	45.04	8.59×10^3	0.164
Geocell					
Tensile stiffness, M (kPa/m)				212	
Cell diameter, D (m)				0.25	

Table 5.2 Measured and calculated resilient moduli of unreinforced and geocell-reinforced sand

Seq. No.	σ_3 (kPa)	$\sigma_1 - \sigma_3$ (kPa)	Test result		Calculated result		$\Delta\sigma_3$ (kPa)
			M_r (MPa) Unreinforced	M_r (MPa) Reinforced	M_r (MPa) Unreinforced	M_r (MPa) Reinforced	
1	20.7	20.7	36.6	34.7	39.1	40.6	6.5
2	20.7	41.4	44.2	43.4	44.3	46.4	11.4
3	20.7	62.1	51.7	52.8	49.1	51.5	15.4
4	34.5	34.5	50.2	52.5	52.2	53.7	8.2
5	34.5	68.9	63.4	66.4	59.2	61.3	14.4
6	34.5	103.4	66.4	71.3	65.6	67.8	19.5
7	68.9	68.9	79.6	84.5	77.4	78.9	11.2
8	68.9	137.9	89.8	95.1	87.7	89.7	19.7
9	68.9	206.8	87.9	86.4	97.1	99.2	26.7
10	103.4	68.9	92.8	97.4	92.8	94.0	9.4
11	103.4	103.4	96.2	96.2	97.4	98.9	13.4
12	103.4	206.8	111.7	113.2	110.3	112.3	23.5
13	137.9	103.4	108.7	104.9	110.6	111.9	11.8
14	137.9	137.9	115.8	113.6	114.7	116.2	15.2
15	137.9	275.8	127.2	127.9	129.8	131.8	26.8

Table 5.3 Measured and calculated resilient modulus of unreinforced and geocell-reinforced silt loam

Seq. No.	σ_3 (kPa)	$\sigma_1 - \sigma_3$ (kPa)	Test result		Calculated result		$\Delta\sigma_3$ (kPa)
			M_r (MPa) Unreinforced	M_r (MPa) Reinforced	M_r (MPa) Unreinforced	M_r (MPa) Reinforced	
1	41	12.7	41.3	48.4	43.2	45.7	10.6
2	41	25.1	41.5	51.7	42.2	46.7	20.5
3	41	36.9	42.6	52.4	41.3	47.4	29.7
4	41	49.5	42.1	52.2	40.4	48.0	39.4
5	41	62.1	41.5	52.7	39.4	48.3	49.0
6	21	12.5	32.7	38.2	32.5	34.8	13.7
7	21	25.1	32.2	38.0	32.7	36.9	26.0
8	21	36.9	32.2	39.2	32.8	38.3	36.8
9	21	49.5	33.1	39.8	32.7	39.5	47.9
10	21	62.1	33.6	41.0	32.6	40.3	58.8
11	0	12.5	14.9	17.4	13.4	21.0	22.7
12	0	25.1	17.4	19.7	17.7	25.4	37.6
13	0	36.9	19.0	22.0	20.1	28.0	50.4
14	0	49.5	20.3	24.3	21.9	29.8	63.4
15	0	62.1	22.5	26.4	23.1	31.1	76.2

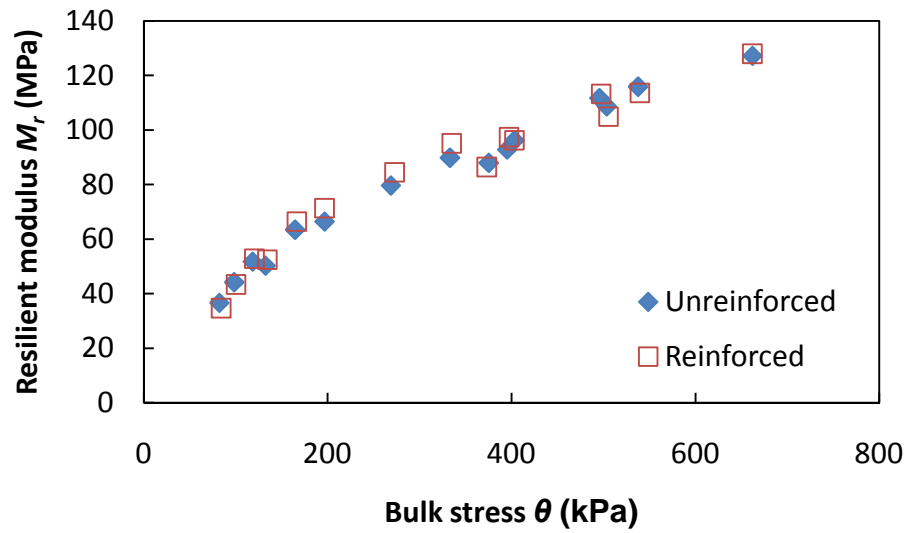


Figure 5.7 Measured resilient modulus vs. bulk stress for Roddefeld sand (Mengelt et al. 2000)

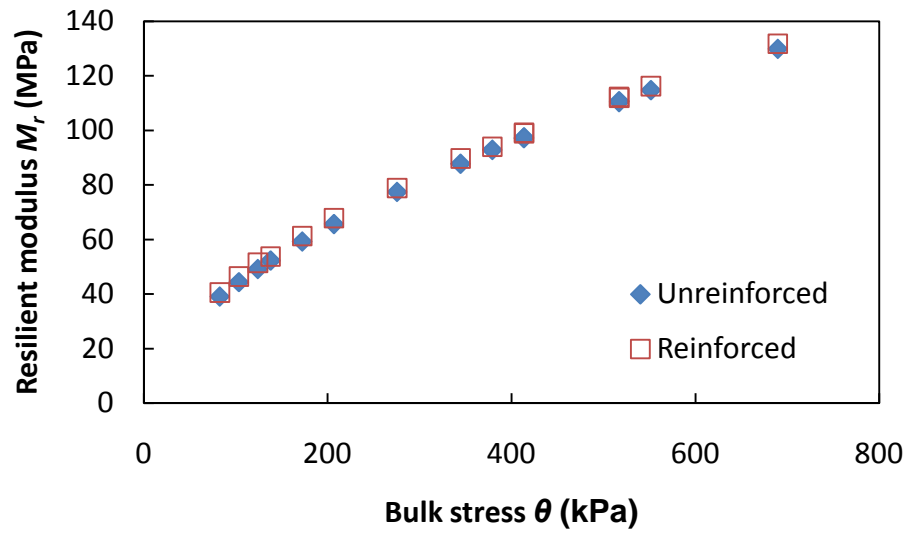


Figure 5.8 Calculated resilient modulus vs. bulk stress for Roddefeld sand

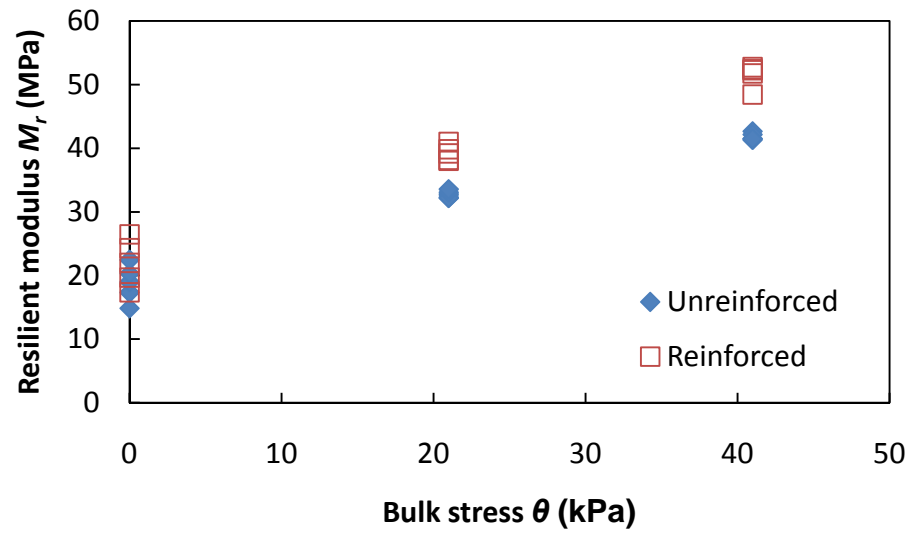


Figure 5.9 Measured resilient modulus vs. bulk stress for Antigo silt loam (Mengelt et al. 2000)

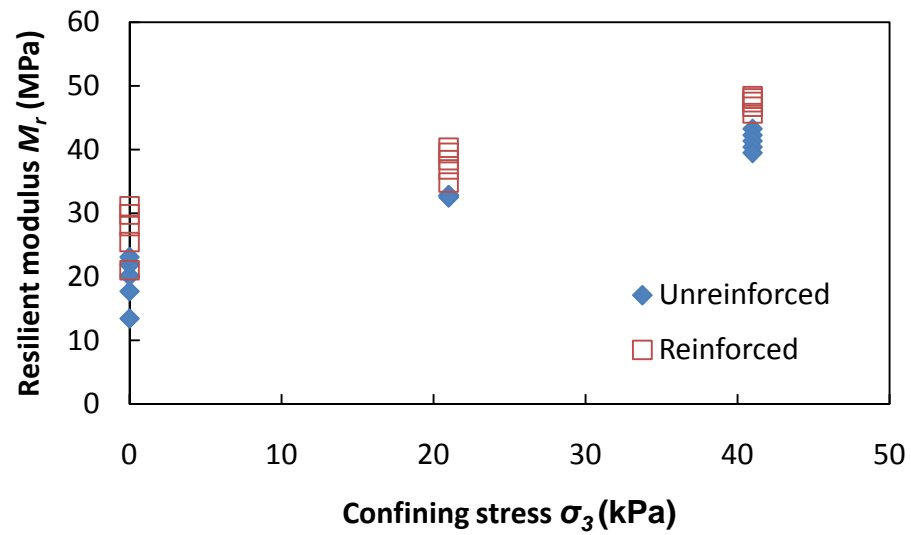


Figure 5.10 Calculated resilient modulus vs. bulk stress for Antigo silt loam

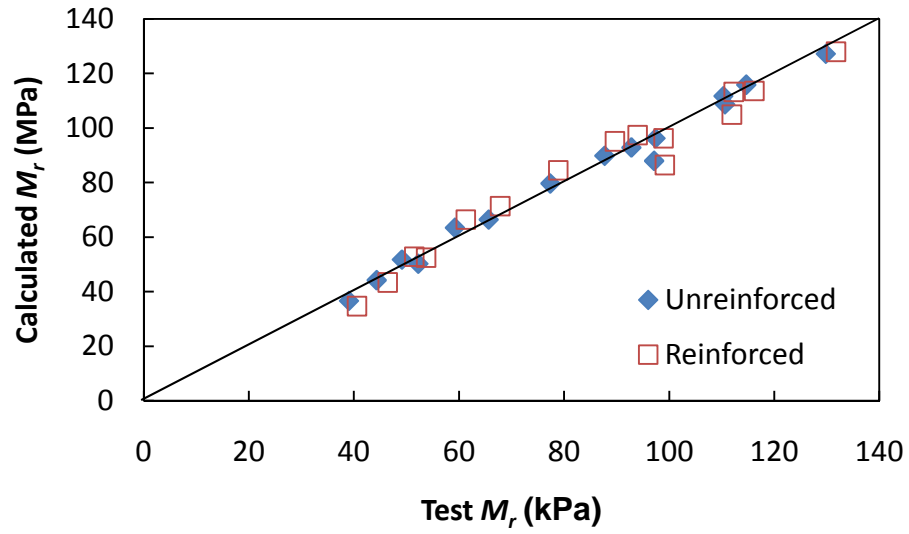


Figure 5.11 Calculated vs. measured resilient moduli for Lodefeld sand

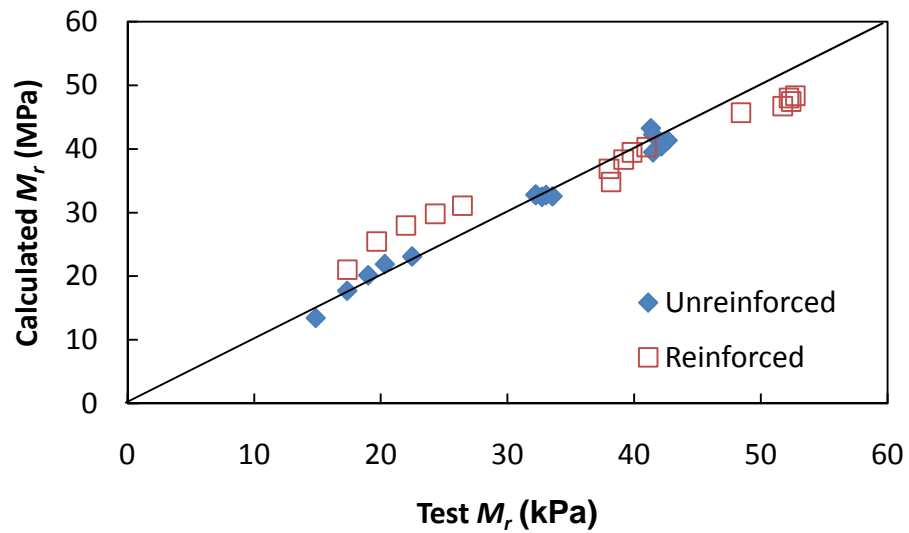


Figure 5.12 Calculated vs. measured resilient moduli for Antigo silt loam

5.2.4 Equivalent resilient modulus parameters

The analytical solution developed in the previous section provides a simple and rational method to estimate the residual stress in the infill soil. However, the stress path of soil in a cyclic triaxial test is relatively simple compared to the stress path of soil induced by a moving wheel load. In reality, the vertical and the horizontal stresses in the pavement are both cyclic. In this case, a simple modification to the analytical solution developed above is to substitute all the terms σ_1 and σ_3 in Equations 5.18, 5.19, and 5.20 by the maximum wheel load-induced vertical stress σ_v and horizontal stress σ_h , assuming the soil is incompressible and the stress-strain behavior of the soil is independent of loading sequence (or stress path).

However, even with this modification, it is still difficult to use this analytical solution to calculate the residual stress in the geocell reinforced soil in a pavement, because σ_v and σ_h should be, ideally, calculated or estimated for the soil at the center and mid-depth of each cell. Apparently, an exact solution based on multi-layer elastic theory is tedious and difficult to achieve due to the presence of geocell. Besides, applying different horizontal stresses to the soil in each cell will cause an unbalance initial stress situation.

To solve this problem, equivalent resilient modulus parameters (k_1' , k_2' and k_3') can be used as an alternative way to consider the effect of geocell reinforcement

on the increased resilient modulus of soil. Such equivalence assumes that the resilient modulus of the geocell-reinforced soil can be simulated using the same stress-dependent resilient modulus model (Equation 5.16) as that of the unreinforced soil. The equivalent resilient modulus parameters can be determined by a similar regression procedure as for the unreinforced soil on the calculated resilient modulus for the geocell-reinforced soil at each load sequence of a standard resilient modulus test. In this study, the equivalent resilient modulus parameters for the infill soil were used in the numerical analysis.

5.3 Material model and parameters

In this section, the behavior of unpaved road Section 2 in the moving-wheel test was modeled using the mechanistic-empirical model. In the response model, base and subgrade materials were both modeled using the non-linear elastic model based on the tangent resilient modulus equation (Equation 5.9) derived previously in this chapter. The permanent deformation (damage) model proposed by Tseng and Lytton's (1989) was adopted in this study to be consistent with the current mechanistic-empirical pavement design guide. All the material parameters are listed in Table 5.4. The resilient modulus and permanent deformation parameters for the Kansas River sand and AB-3 aggregate were calibrated from the cyclic triaxial test data (see Appendix A). The resilient modulus of the clay was estimated from a correlation (Equation 5.28) to a CBR value. Poisson's ratio ν for all materials were assumed to be 0.25.

The permanent deformation parameters for the clay were calibrated by trial-and-error to match the measured rutting development curve in test Section 2.

$$M_r \text{ (psi)} = 2555(CBR)^{0.64} \quad 5.28$$

The equivalent resilient modulus parameters (listed in Table 5.5) for the geocell-reinforced sand were obtained based on the method introduced in the previous section.

Table 5.4 Material parameters of each material

Kansas River Sand						
Resilient modulus parameter				Permanent deformation parameter		
k_1	k_2	k_3	ν	$\left(\frac{\varepsilon_0}{\varepsilon_r}\right)$	ρ	β
820	0.67	-0.45	0.35	8.97	8.21×10^3	0.095
AB-3						
Resilient modulus parameter				Permanent deformation parameter		
k_1	k_2	k_3	ν	$\left(\frac{\varepsilon_0}{\varepsilon_r}\right)$	ρ	β
1321	0.53	-0.32	0.35	9.20	3.18×10^2	0.120
Clay						
Resilient modulus parameter				Permanent deformation parameter		
CBR (%)	M_r (psi)	M_r (MPa)	ν	$\left(\frac{\varepsilon_0}{\varepsilon_r}\right)$	ρ	β
5	7157	49.3	0.35			
Geocell Type IV						
E (MPa)	t (mm)	M (kN/m)	ν	Height (cm)	Equivalent diameter (cm)	
420	1.1	462	0.45	15	18.1	

Table 5.5 Equivalent resilient modulus parameters for the geocell reinforced sand

Resilient modulus parameter of unreinforced sand:					
$k_1 = 820, k_2 = 0.67, k_3 = -0.45$					
Seq. No.	σ_3 (kPa)	$\sigma_1 - \sigma_3$ (kPa)	M_r (MPa) Unreinforced (Calculation)	M_r (MPa) Reinforced (Calculation)	M_r (MPa) Reinforced (Regression)
1	20.5	20.8	69.3	75.8	74.9
2	20.5	41.8	77.7	87.8	84.1
3	20.6	61.6	84.6	97.2	91.9
4	34.3	34.9	95.4	103.3	101.7
5	34.6	68.8	104.8	117.1	112.5
6	34.4	102.7	112.1	127.6	121.3
7	68.5	68.7	142.9	154.0	150.7
8	68.5	137.9	150.6	168.1	161.9
9	68.5	206.3	157.0	178.7	171.5
10	102.6	68.8	176.7	187.1	184.0
11	102.5	102.9	177.8	191.8	187.3
12	102.6	206.7	182.2	203.6	197.3
13	137.6	102.8	207.3	220.7	216.3
14	137.6	137.5	206.6	223.1	218.0
15	137.5	274.9	206.8	231.3	225.7
Resilient modulus parameter of geocell-reinforced sand:					
$k_1 = 891, k_2 = 0.61, k_3 = -0.26$					

5.4 Modeling of the moving wheel test

Numerical response models were first created with FLAC^{3D} to simulate the result of the moving wheel test performed in this study. The vertical compressive strains along the center-line of the model were then extracted from the response model to calculate the rut depth development with the number of passes. Details about the test procedure and results were discussed in Chapter 3.

5.4.1 Numerical mesh and boundary conditions

The dimension of the response model should be large enough to minimize the boundary effect. Thus the vertical boundaries were set to be 0.84m in x direction and 1m in y direction from the center of the load area, and the bottom boundary was set at 1m below the top of the subgrade. The thickness and material of each layer in the response model for each test section were provided in Table 5.6. The geocell pockets were modeled in a diamond shape, which is more appropriate than sine curve for a multi-cell situation. Tire pressure of 550kPa (80psi) was applied to a rectangular contact area (0.29m×0.25m) to simulate a 40kN (9kips) wheel load. Due to the symmetry of the problem, a quarter of the model was created for each test section. As an example, Figure 5.13 shows the numerical mesh of the response model for test Section 2.

Table 5.6 Layer thickness and materials in the response model

	Layer	Thickness (cm)	Material
Section 1	Base	23.8	AB3
	Subgrade	100	Clay
Section 2	Base	23.8	15cm Geocell reinforced sand + 8.8cm AB3 cover
	Subgrade	100	Clay
Section 3	Base	18	10cm Geocell reinforced sand + 8cm AB3 cover
	Subgrade	100	Clay
Section 4	Base	18	AB3
	Subgrade	100	Clay

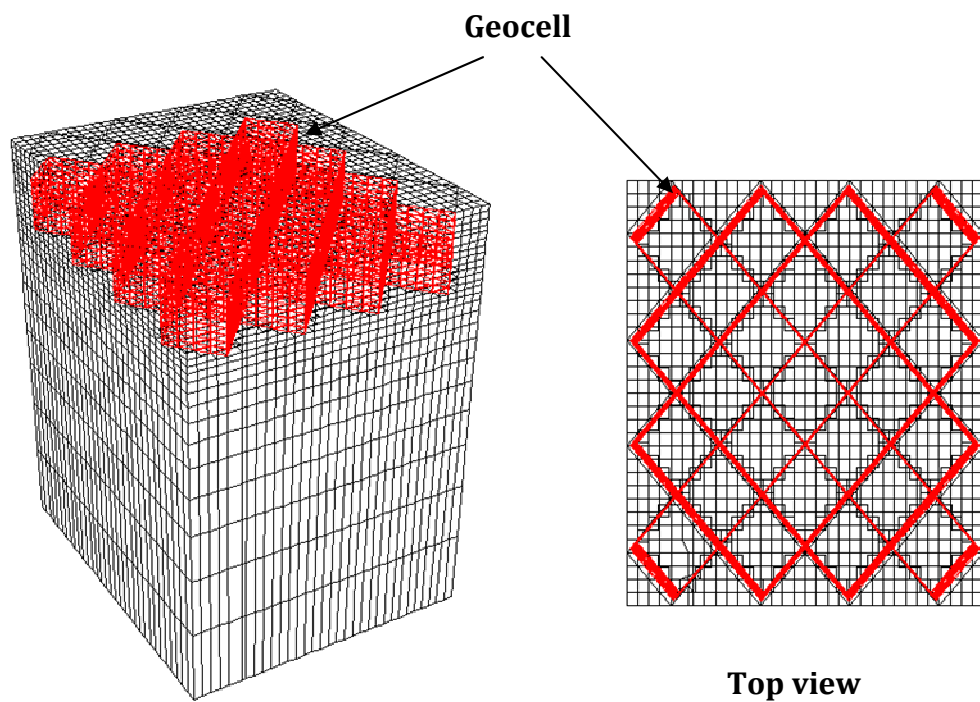
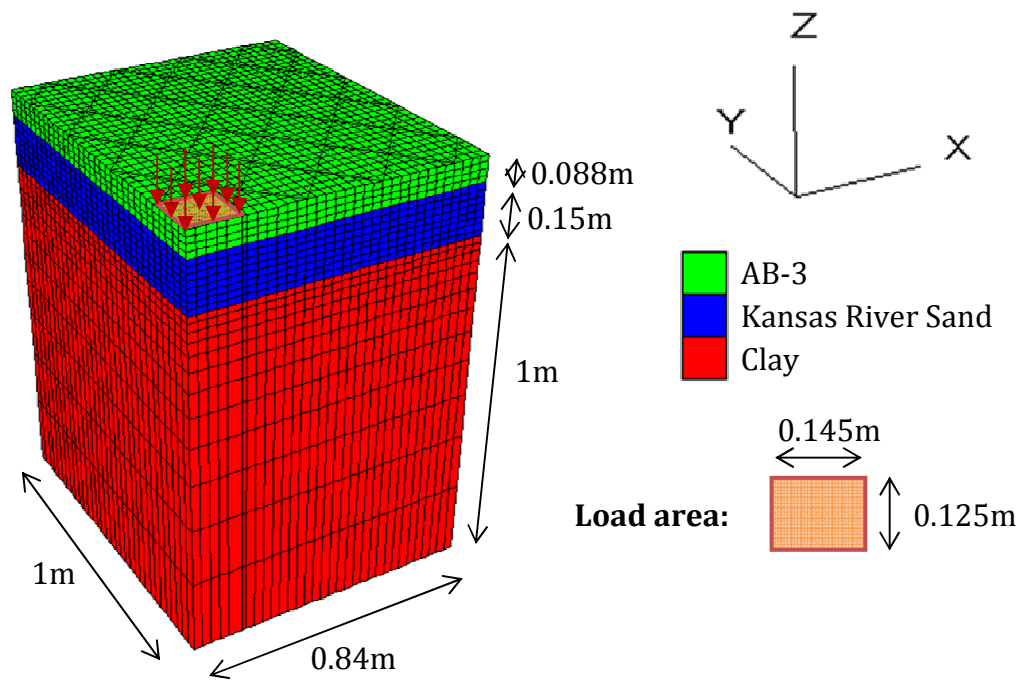


Figure 5.13 Numerical mesh of the response model (Section 2)

5.4.2 Load application

The formulation of the tangent resilient modulus requires that the load should be added in adequately small steps to maintain the accuracy of the model. In a series of trial runs of the model, it was found that the deformation of the model is more sensitive to the load step at the beginning of the loading, especially the first 50kPa. But applying load in small steps (e.g., 1kPa) would significantly slow down the calculation. To seek a balance between efficiency and accuracy, it was finally determined that the first step of load was set to 0.5kPa, after that, the load increment in each following step was set to be 1.2 times the load increment in the previous step. So the 2nd load applied was $0.5+0.5\times1.2=1.1\text{kPa}$, and the 3rd load applied was $1.1+0.5\times1.2\times1.2=1.82\text{kPa}$, and so on. When the last calculated load exceeded 550kPa, it was set to be 550kPa (i.e., tire contact pressure).

5.4.3 Resilient response

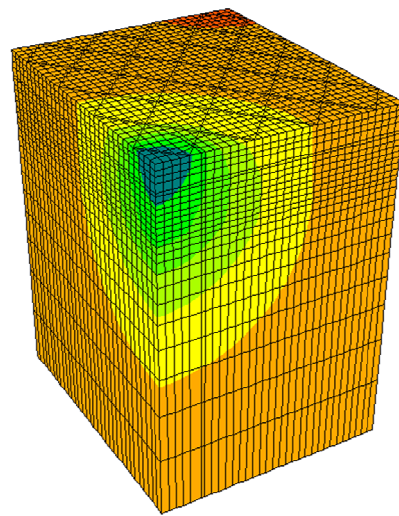
Some of the calculated resilient responses obtained from the numerical response models are listed in Table 5.7. Overall, the two sections (1 and 2) with 23.8cm thick bases performed better than the two sections (3 and 4) with 18cm bases. And the geocell-reinforced sand base course exhibited similar performance to the AB3 aggregate gravel base course. Figure 5.14 shows the vertical displacement contours of the four sections. Figure 5.15 shows the vertical stress contours of the four sections. Figure 5.16 shows the contours of vertical stresses

only in the subgrade. It is shown that an increase of the base course thickness by 5cm thicker reduced the maximum vertical stress on the top of subgrade reduced by about 20%. Figure 5.17 shows the distribution of the horizontal resilient stress in the geocell. It is shown that the 10cm high geocell developed higher tensile stresses than the 15cm high geocell.

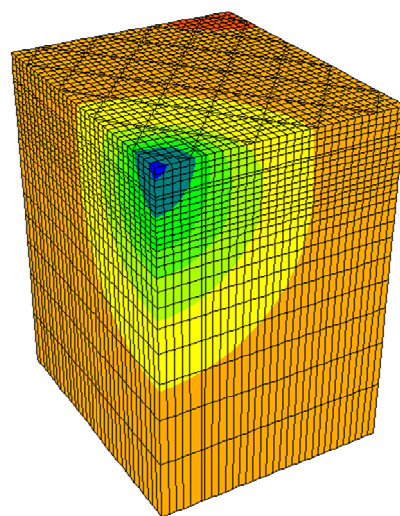
The vertical resilient strains along the center line of the load can be extracted from the response model, as shown in Figure 5.18 and Figure 5.19. These resilient strain data can be input into the damage model to calculate the permanent deformation of the road sections.

Table 5.7 Some resilient responses from the response models

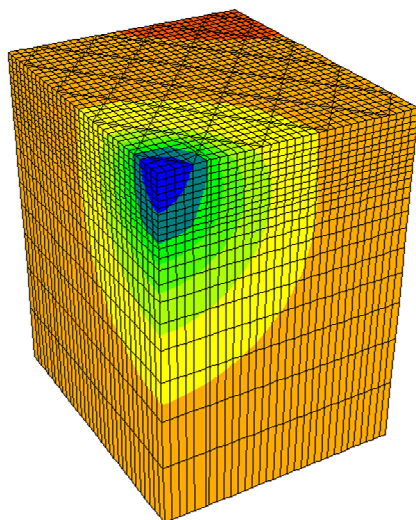
Resilient response	Section 1	Section 2	Section 3	Section 4
Vertical displacement (mm)	1.16	1.22	1.38	1.34
Vertical stress on top of subgrade (kPa)	159	177	219	221
Vertical strain on top of subgrade (%)	0.36	0.36	0.46	0.46
Maximum tensile stress in geocell (N/m)	--	353	811	--
Maximum tensile strain in geocell (%)	--	0.08	0.18	--



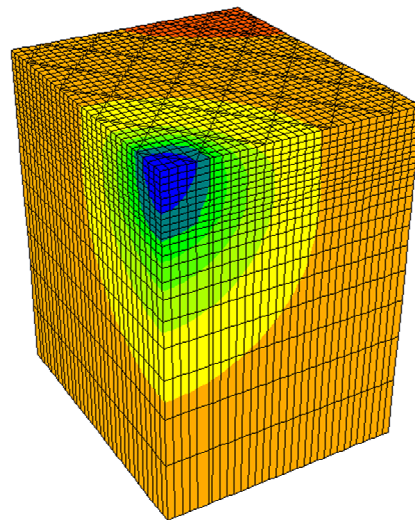
Section 1 (Max=1.16mm)



Section 2 (Max=1.22mm)



Section 4 (Max=1.34mm)



Section 3 (Max=1.38mm)

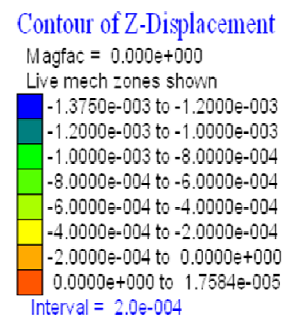
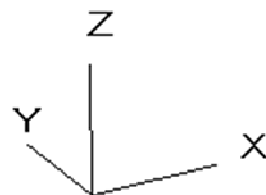
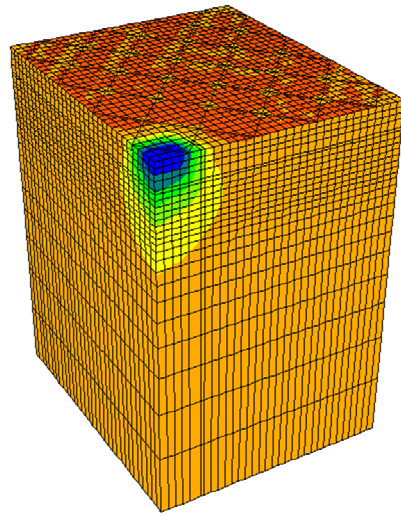
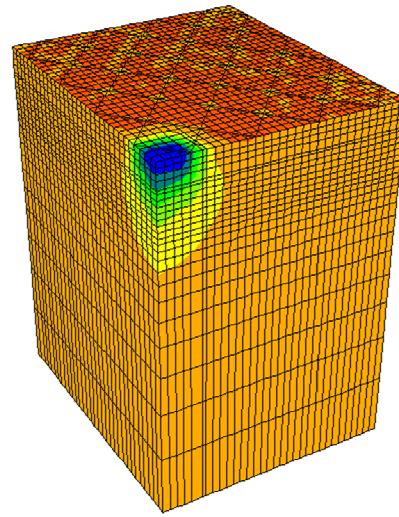


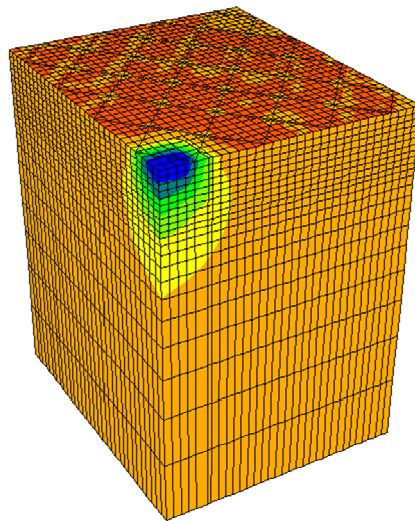
Figure 5.14 Contours of vertical displacement (Unit: m)



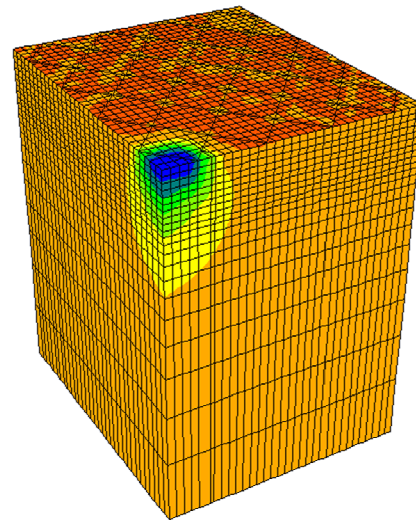
Section 1



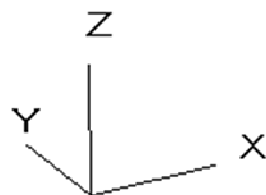
Section 2



Section 4



Section 3



Contour of SZZ

Magfac = 0.000e+000

Live mech zones shown

Gradient Calculation

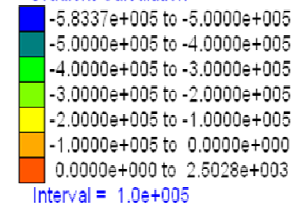
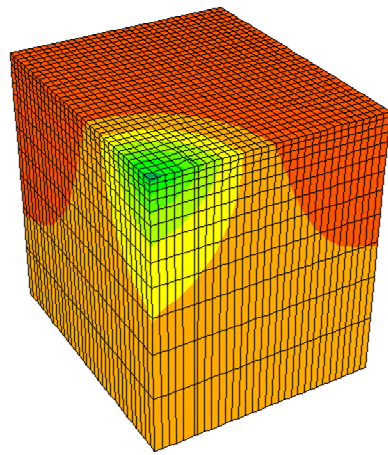
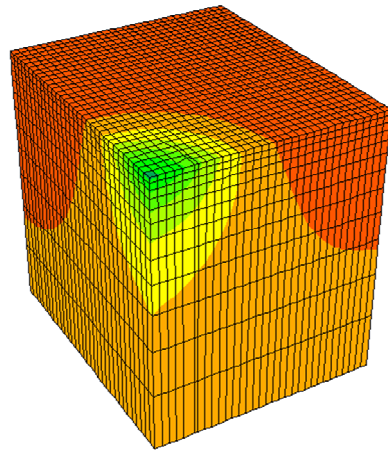


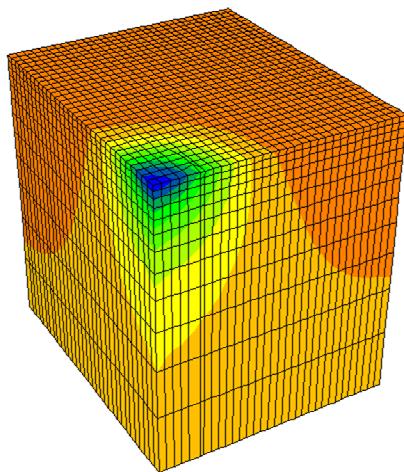
Figure 5.15 Contours of vertical stress (Unit: Pa)



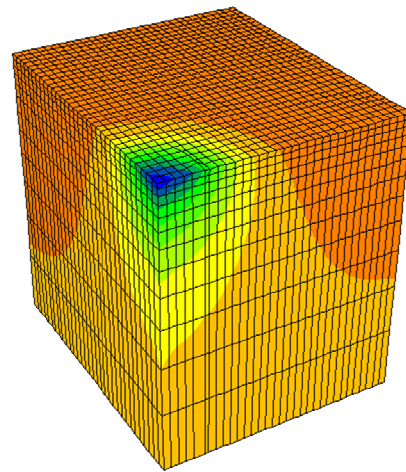
Section 1 (Max=159kPa)



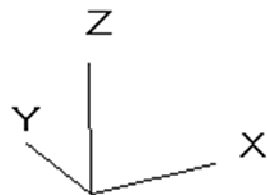
Section 2 (Max=157kPa)



Section 4 (Max=221kPa)



Section 3 (Max=219kPa)



Contour of SZZ

Magfac = 0.000e+000

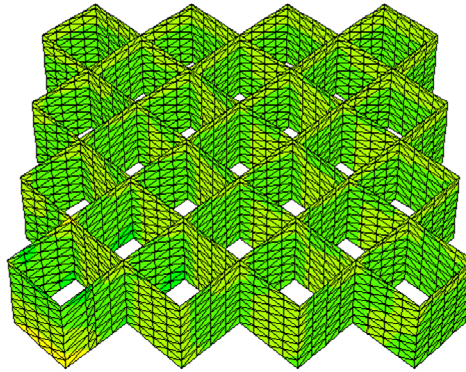
Live mech zones shown

Gradient Calculation

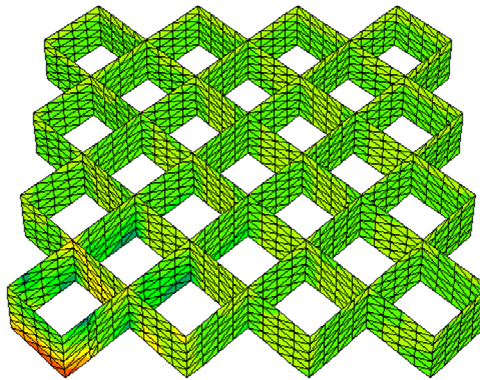
-2.2153e+005 to -2.0000e+005
 -2.0000e+005 to -1.7500e+005
 -1.7500e+005 to -1.5000e+005
 -1.5000e+005 to -1.2500e+005
 -1.2500e+005 to -1.0000e+005
 -1.0000e+005 to -7.5000e+004
 -7.5000e+004 to -5.0000e+004
 -5.0000e+004 to -2.5000e+004
 -2.5000e+004 to 0.0000e+000
 0.0000e+000 to 5.3496e+003

Interval = 2.5e+004

Figure 5.16 Contours of vertical stress in the subgrade (Unit: Pa)



Section 2 (Geocell height=15cm)



Section 3 (Geocell height=10cm)

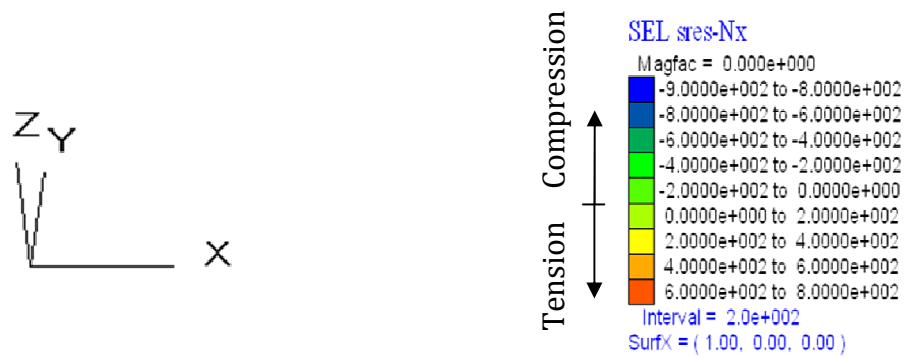
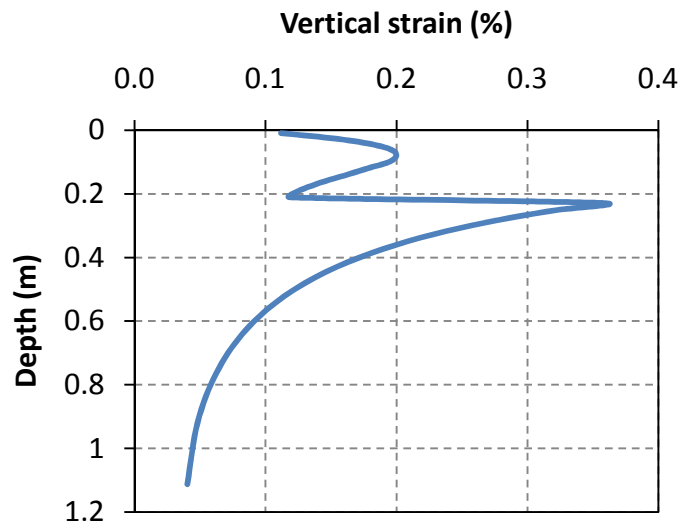
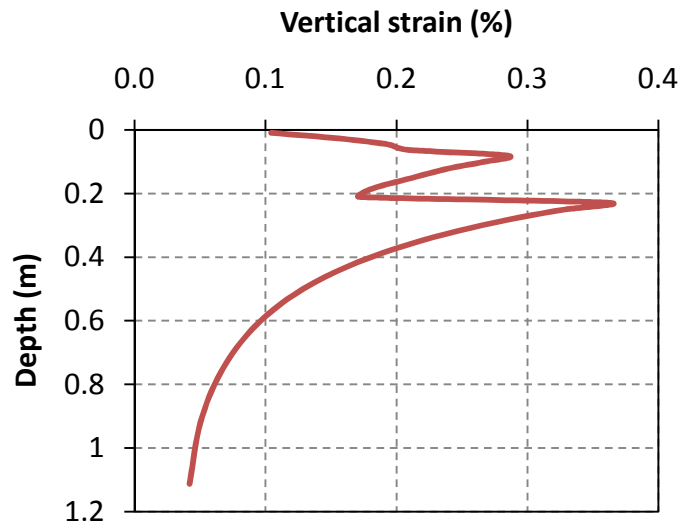


Figure 5.17 Contours of horizontal resilient stress in geocell (Unit: N/m)

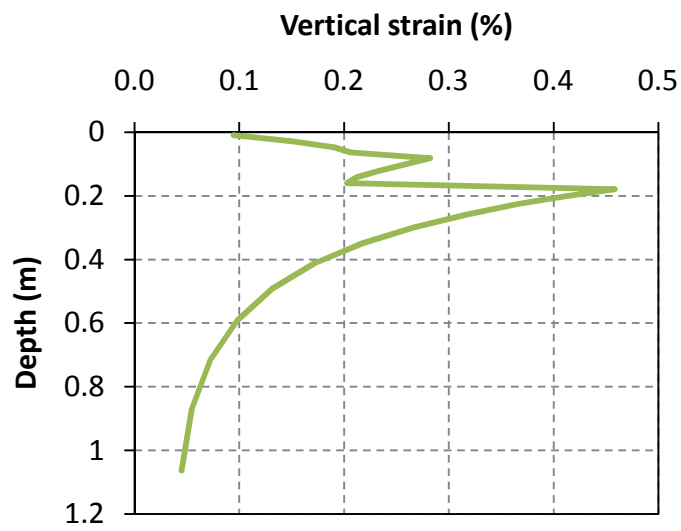


(a) Section 1

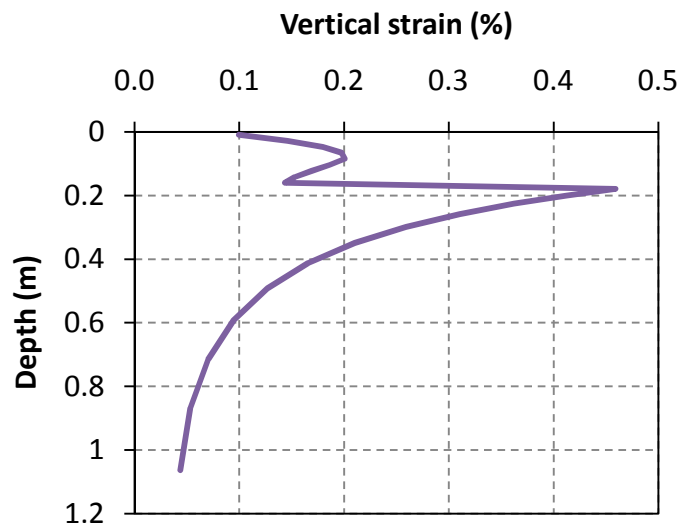


(b) Section 2

Figure 5.18 Vertical resilient strains along the center line (Sections 1 and 2)



(a) Section 3



(b) Section 4

Figure 5.19 Vertical resilient strains along the center line (Sections 3 and 4)

5.4.4 Permanent deformation

From the vertical resilient strain data extracted from the response model, the average vertical resilient strain ε_v can be calculated for each layer of material in each section. Then permanent strains accumulated in each layer can be calculated from the average resilient strain using the damage model. In this study, the rutting damage model for unbound aggregate in the MEPDG is modified by replacing the local and global calibration factors in Equation 2.24 by a single calibration factor k (as shown in Equation 5.29). The calibration factor k is used to account for the differences in the conditions between the soil sample under a cyclic triaxial test and the soil in the field under a moving-wheel load.

$$PD = k\varepsilon_v h_{soil} \left(\frac{\varepsilon_0}{\varepsilon_r} \right) \cdot e^{-\left(\frac{\rho}{N} \right)^\beta} \quad 5.29$$

where PD is the permanent deformation in a particular layer, ε_v is the average vertical resilient strain along the centerline of the model in this layer, h_{soil} is the thickness of this layer, and $\left(\frac{\varepsilon_0}{\varepsilon_r} \right)$, ρ , and β are the material parameters obtained from the cyclic triaxial tests.

Since no external data is available for calibrating the factor k , one of the test sections (Section 2) was selected to determine the calibration factor. The permanent deformation parameters for clay also need to be calibrated since the

cyclic triaxial test data for clay is also not available. The calibration was carried out by a trial-and-error procedure until the permanent deformation in each layer in Section 2 match the accumulated permanent deformation data (see Figure 3.28 Rut depth vs. Number of passes, N Figure 3.28) as well as the profile data measured after the moving-wheel test (see Figure 3.30). For a comparison purpose, the permanent deformation model in MEPDG (Equation 2.24) was also calibrated by replacing the global and local calibration factors by a single calibration factor k . The calibrated parameters for both methods are listed in Table 5.8 and Table 5.9 respectively. The calibrated parameters listed in Table 5.8 were then applied to the rutting prediction for other sections. It should be noted that the calibration factors for the base layer is considerably higher than 1. This is because the confining stress and cyclic stress applied to the sample in the cyclic triaxial test is not representative of the field stress level in an unpaved road base. Currently there is no test standard available for the permanent deformation test. Future investigation is needed for the representative stress level to be used in a permanent deformation test on unpaved road base materials.

Table 5.8 Calibrated parameters for rutting prediction from Section 2 (based on permanent deformation test data)

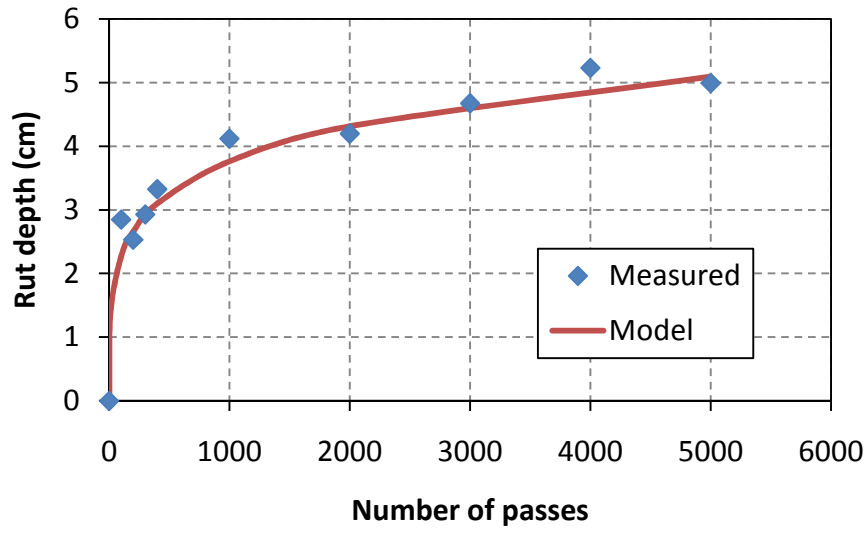
Layers	Calibrated parameters
AB-3	$k = 20$
Kansas River sand	$k = 18$
Subgrade*	$k \left(\frac{\varepsilon_0}{\varepsilon_r} \right) = 110, \rho = 2.5 \times 10^4, \beta = 0.2$

*For subgrade, k and $\left(\frac{\varepsilon_0}{\varepsilon_r} \right)$ has to be calibrated together.

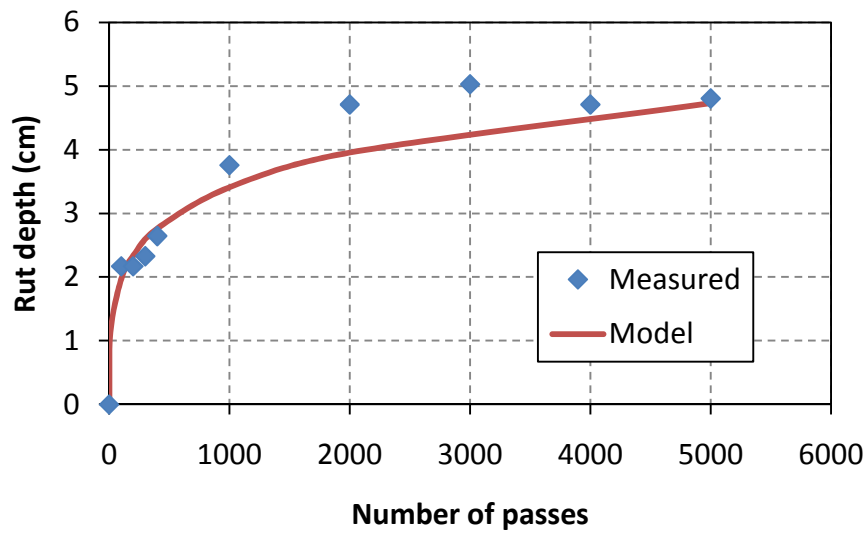
**Table 5.9 Calibrated parameters for rutting prediction from Section 2
(based on the permanent deformation model in MEPDG (Equation 2.24))**

Layers	Calibrated parameters
AB-3	$k = 13$
Kansas River sand	$k = 8$
Subgrade	$k = 8$

The calculated rut depth accumulations for each section were compared with the test data in Figure 5.20. Overall, the calculated results from the mechanistic-empirical model matched the test data well except Section 3. In this section, the measured rut depth from the moving wheel test was considerably larger than the calculated results after 500 wheel passes. This phenomenon may be caused by the damage of the geocell as discovered after the test (see Figure 3.29).

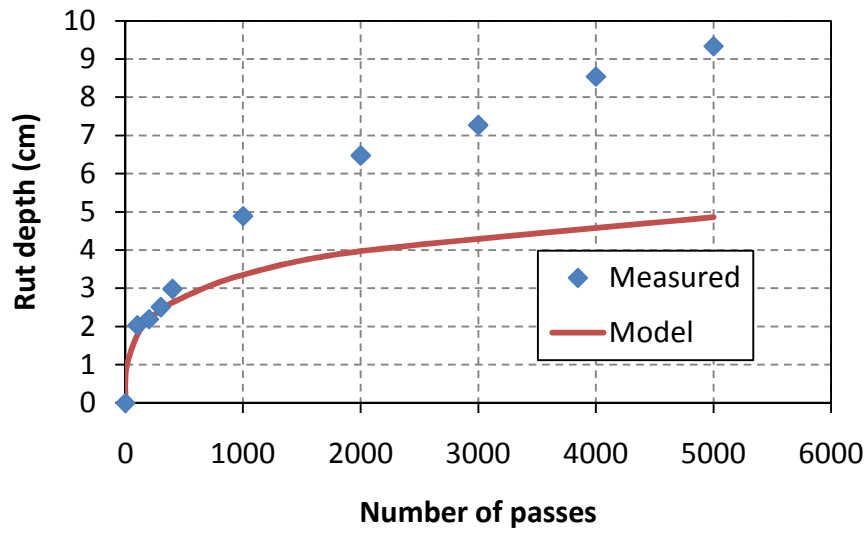


(a) Section 1

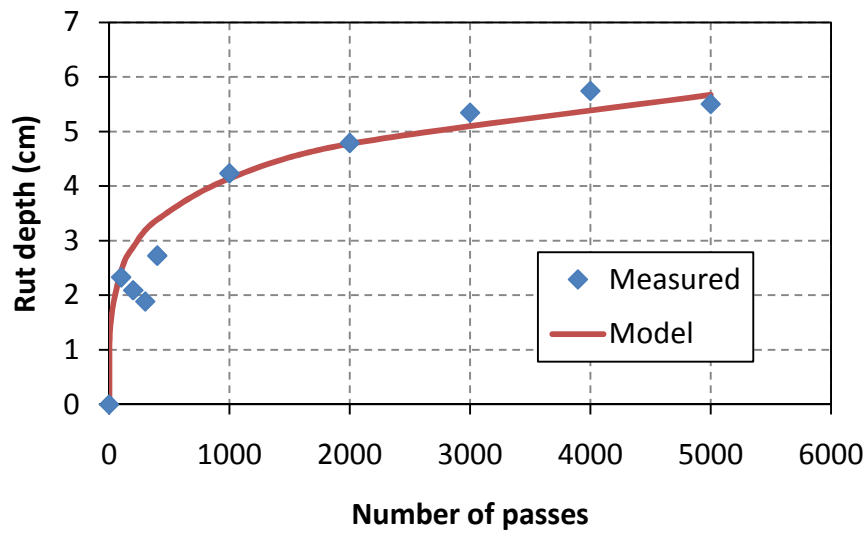


(b) Section 2

Figure 5.20 Calculate vs. measured rut depths (Sections 3 and 4)



(c) Section 3



(d) Section 4

Figure 5.20 Calculate vs. measured rut depths (continued)

5.5 Parametric study

Based on the numerical model created in this study, a parametric study was performed to investigate the rutting behavior of the unpaved road with a geocell reinforced base. In this section, the layer profile and material in road test Section 1 (with full-depth AB-3 base) was used as the baseline case. The material models, parameters, boundary conditions, and load application were all described in the previous sections. Based on the baseline case, variations were made to evaluate the effect of (a) the resilient modulus of the infill material, (b) the modulus of the geocell, and (c) the resilient modulus of the subgrade.

5.5.1 Reinforced and unreinforced bases

With the numerical model developed in this study, a reinforced case based on Section 1 was modeled. In this case, a 15 cm high geocell was used at the bottom of the AB-3 layer (similar to Section 2). The accumulated rut depths of the unpaved roads, with and without the geocell reinforcement, were plotted in Figure 5.21. It is shown that, in the particular case modeled, the rut depth of the geocell-reinforced unpaved road is about 7% less than that of the unreinforced road. In other words, for a well-graded high-quality base course material, the benefit of geocell in reducing rutting is insignificant.

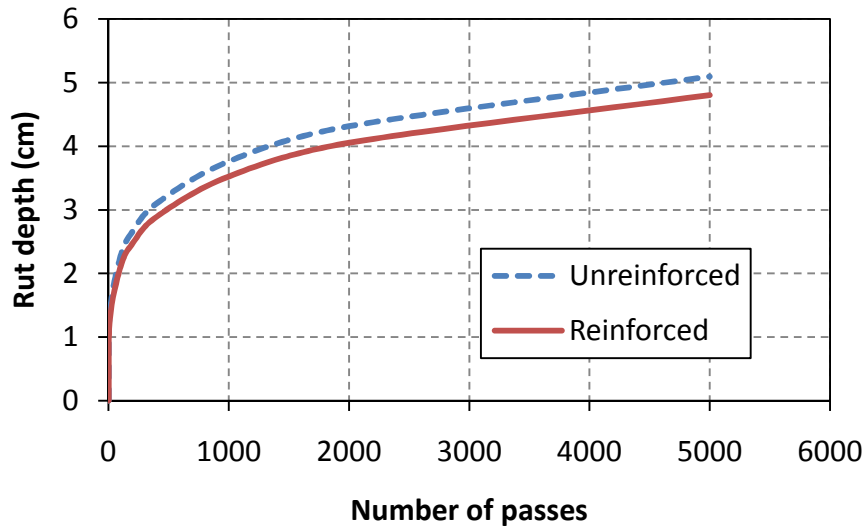


Figure 5.21 Accumulated rut depths of the road with vs. without geocell reinforcement

5.5.2 Effect of the resilient modulus of the infill material

Since k_1 is proportional to the magnitude of resilient modulus of granular material (see Equation 5.16), the value of k_1 is reduced to 660 in this section to simulate a relatively low-quality base course material, such as sand. The reinforced case and the unreinforced case are both modeled. The accumulated rut depths of the unpaved road, with and without the geocell reinforcement, were plotted in Figure 5.22. Since the subgrade is relatively firm (CBR=5%) in this case, the reduced base course modulus greatly increased the deformation in the base course. It is also shown that when the resilient modulus of the infill material was reduced, the benefit of geocell became more significant. Furthermore, the low-quality base material may fail under the wheel load as demonstrated in the moving wheel test for sand, before it can carry more

number of passes. Unfortunately, the failure of the base course cannot be modeled using the resilient model. Therefore, the benefit of geocell reinforcement for low-quality infill materials (such as sand) would be even more significant if the failure of the base course could be modeled. Figure 5.22 also shows an increase of k_1 to 1321 reduced the benefit of geocell reinforcement.

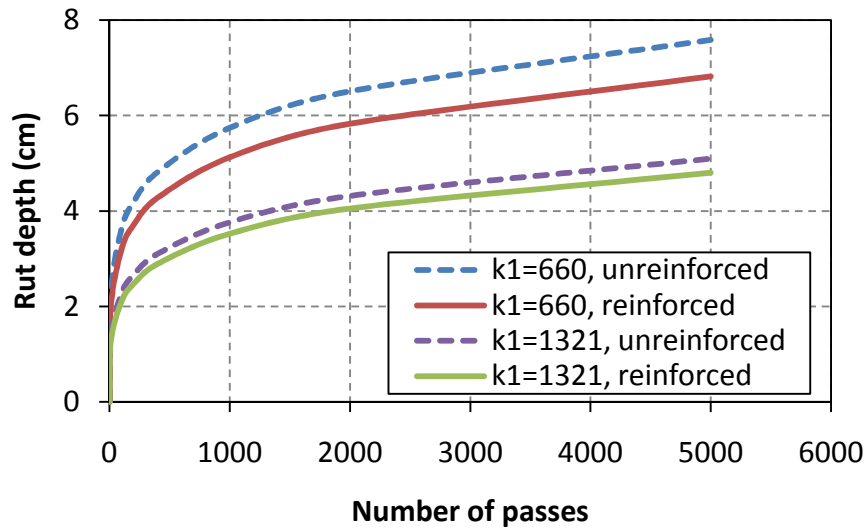


Figure 5.22 Accumulated rut depths of the road with different infill materials

5.5.3 Effect of the modulus of the geocell

Based on the baseline case with an AB-3 base course reinforced by a 15-cm high geocell, the tensile stiffness of the geocell was changed to 1848 kN/m and 3696 kN/m, which is four times and eight times of its original value respectively. The

accumulated rut depths of the unpaved road were plotted in Figure 5.23. As expected, increasing the tensile stiffness of the geocell reduced the rut depths of the geocell-reinforced base. It is also indicated that the increase of geocell modulus from 1848 kN/m to 3696 kN/m did not provide further improvement.

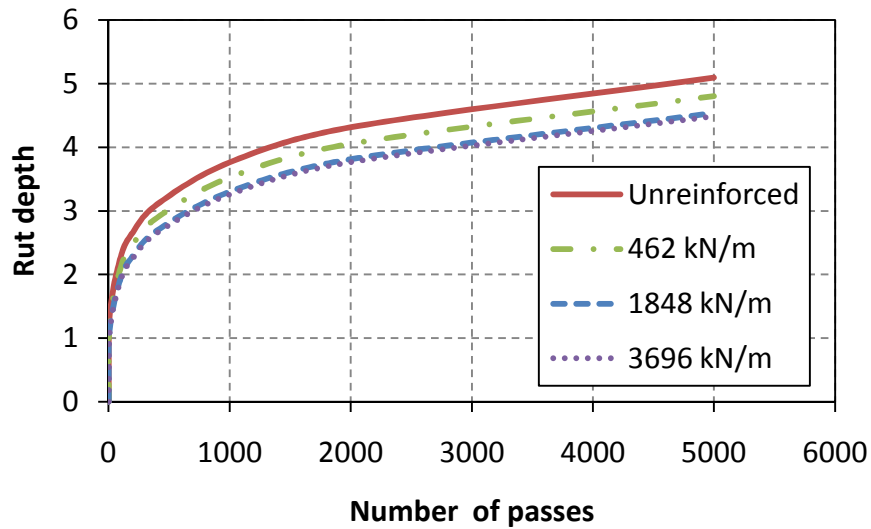


Figure 5.23 Accumulated rut depth of the road with different geocell modulus

5.5.4 Effect of the stiffness of the subgrade

Based on the baseline case, the resilient modulus of the subgrade was reduced to 25MPa, which is about one half of its original value. The accumulated rut depths of the unpaved road, with and without the geocell reinforcement, are plotted in Figure 5.24. As expected, the unpaved roads constructed on a relatively soft subgrade developed more rutting than those on a stiff subgrade. However, the benefit of geocell-reinforcement is still not significant in Figure 5.24 because the

baseline case had a high-quality base material (AB-3). Analyses were also performed on the roads with a low-quality base material ($k_1=660$), the calculated rut depths for reinforced and unreinforced roads are shown in Figure 5.25.

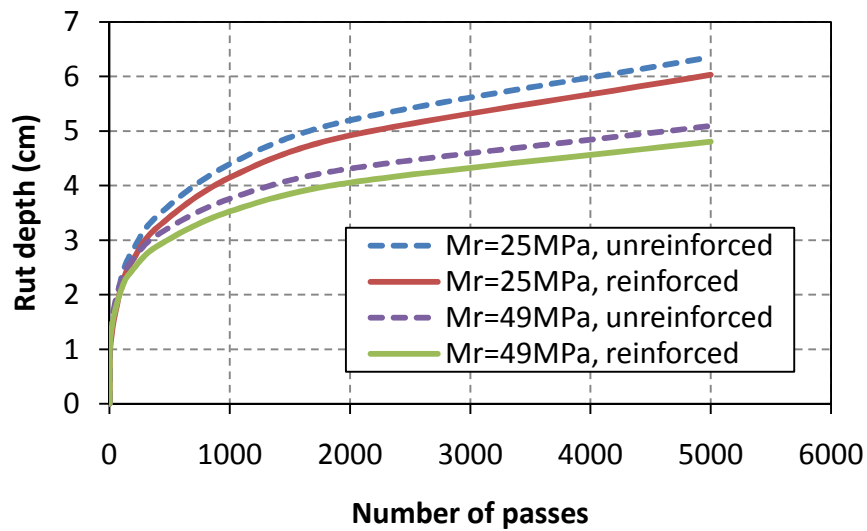


Figure 5.24 Accumulated rut depth of the road with different types of subgrade (high-quality infill material)

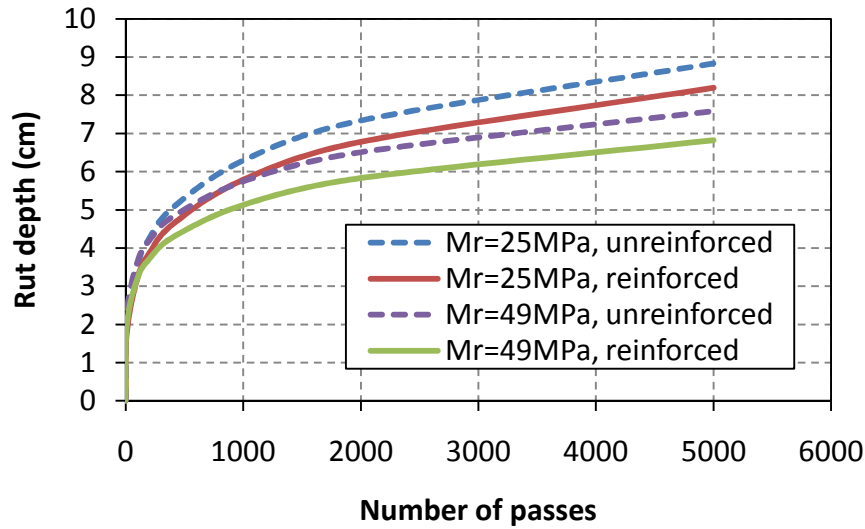


Figure 5.25 Accumulated rut depth of the road with different types of subgrade (low-quality infill material)

5.6 Mechanistic-empirical design method for the geocell-reinforced base in paved and unpaved roads

5.6.1 Paved roads

The newly-developed mechanistic-empirical pavement design guide (MEPDG) and the associated design software (ME-PDG version 1.1) are still in a draft stage. Researchers and government agencies are currently making efforts to calibrate and improve the design method and the software. Since ME-PDG (version 1.1) is not able to consider the compaction effect and the reinforcement in the finite element response model. The only way to incorporate the geocell design into the program is to use the equivalent resilient modulus parameters in the material input. The analytical solution derived in this study can be used to

estimate the equivalent k_1 , k_2 , and k_3 values for the geocell-reinforced layer. The input parameters for infill materials can be determined from a resilient modulus test following the test standard developed under NCHRP project 1-28A or AASHTO standard T 307. When test data is not available, regression equations proposed by Yau and Von Quintus (2002) can be used to estimate k_1 , k_2 , and k_3 of the infill material, and Equation 2.24 (accepted in the MEPDG) can be used to estimate the value of $\left(\frac{\varepsilon_0}{\varepsilon_r}\right)$. These equations were all calibrated from the LTPP database and should be representative of various types of unbound materials. The additional benefit from compaction model can be considered as a safety margin.

5.6.2 Unpaved roads

ME-PDG (version 1.1) cannot be used to design unpaved roads because an AC (or concrete) surface layer is required in the analysis. Thus the mechanistic-empirical design for geocell-reinforced base in unpaved roads must be done by finite element analyses. Based on the findings in this study, it is recommended that the bearing capacity of the road has to be checked before running the mechanistic-empirical analyses. The wheel load can be applied as a static load on the unpaved road as described in Chapter 4. To ensure the stress level in the base/subgrade materials is lower than the “shakedown” limit, the designed bearing capacity of the road has to be higher than the wheel load by some extent.

Based on the limited test data in this study, a safety factor of 1.5 at 25 cm settlement (based on the analyses on Section 2) is recommended for checking the bearing capacity of the road. The permanent deformation model from the MEPDG can be used to predict the rut depth of the road. The calibration factor k obtained in this study (see Table 5.9) is recommended to be used with Equation 2.24 to replace the global and local calibration factors.

5.7 Summary

In this chapter, the development of a mechanistic-empirical model for geocell reinforced bases was described. Three-dimensional mechanistic response model was created using FLAC^{3D}. Several technical problems were addressed during the development of the response model, including: (a) the three-dimensional constitutive equation for tangent resilient modulus, (b) the compaction-induced initial horizontal earth pressure in the geocell-reinforced layer, and (c) the effect of residual tensile stress accumulated in geocell on the infill material. The permanent deformation model was used to calculate the rut depth of a road at certain numbers of wheel passes. The permanent deformation model was calibrated using the field measurement from one of the test sections in the moving-wheel load test. Then the calibrated model was used to predict rut depths of other sections. A parametric study was carried out to investigate the effect of several factors on the rut depth development of the geocell-reinforced unpaved road. Conclusions drawn from the numerical analyses are:

- (1) The fundamental assumption of the mechanistic-empirical model is that the permanent deformation of a pavement structure becomes stable after a large number of load passes. The mechanistic-empirical model developed in this study also had this assumption and well simulated the rutting behavior of the unpaved roads, as long as the pavement structure stayed stable.
- (2) The benefit of geocell reinforcement in reducing rutting depends on the quality of base course materials. When a relatively low-quality base material with a lower resilient modulus was used, the effect of geocell reinforcement became more significant. The benefit of geocell reinforcement decreased with a better-quality base course. Considering possible bearing capacity failure, geocell reinforcement is expected to have more benefit in reducing rut depths when a low-quality base is used.
- (3) The benefit of geocell-reinforcement increased with the modulus (or tensile stiffness) of the geocell.
- (4) The type of infill material and resilient modulus of subgrade both significantly influenced the rut depth of the unpaved road.
- (5) The design method for geosynthetic-reinforced layers has not been incorporated into the current mechanistic-empirical design software (ME-PDG, version 1.1). The only way to consider the effect of geocell reinforcement is by inputting equivalent parameters for the reinforced

layer. Analytical procedures were proposed in this study for determining the equivalent k_1 , k_2 , and k_3 .

- (6) For an unpaved road, the bearing capacity of the road must be checked before running the mechanistic-empirical model. Numerical methods developed in Chapter 4 and Chapter 5 can be used together to analyze unpaved roads. A future study has to be performed to develop design guidelines for typical base and subgrade materials.

Chapter 6 Conclusions and recommendations

6.1 *Conclusions from this study*

In this study, numerical models were created using a commercial finite difference code, Fast Lagrangian Analysis of Continua in Three-Dimensions (FLAC^{3D}). Two sets of numerical models were created for modeling the geocell-reinforced soil under static and repeated loading conditions. Some features of the developed models are listed in Table 6.1.

Table 6.1 Features of the numerical models developed in this study

Features of the numerical model for static load	Features of the numerical model for repeated load
<ul style="list-style-type: none">❖ Three –dimensional numerical model with geocell and infill material modeled separately.❖ Stress-dependent elasto-plastic model for the infill material.❖ Linear-elastic plate model for geocell❖ Frictional interface between the infill material and the geocell.❖ Able to model the increased stiffness and strength of the geocell-reinforced soil under static load.	<ul style="list-style-type: none">❖ Three –dimensional mechanistic-empirical model with geocell and infill material modeled separately.❖ Stress-dependent resilient response model for the infill material.❖ Linear-elastic plate model for geocell❖ Frictional interface between the infill material and the geocell.❖ Analytical model for estimating the compaction-induced horizontal stress in a geocell-reinforced base.❖ Analytical model for considering the accumulated residual strain in the geocell and the induced additional confining stress to the infill material.❖ Able to model the increased resilient modulus and the reduced permanent deformation of the geocell-reinforced base under repeated load.

6.1.1 Experimental study

A series of laboratory static-load tests and full-scale moving wheel load tests were performed using novel polymeric alloy (NPA) geocells to validate and calibrate the numerical models. Conclusions drawn from the experimental results are:

- (1) The static load test demonstrated that NPA geocell reinforcement improved the bearing capacity of the granular soil. The stiffness of the granular soil was also improved. However the improvement in soil stiffness was not significant until the geocell reinforced soil deformed to some extent.
- (2) For the particular test setup in this study, the ultimate tensile strength of the geocell had no significant influence on the bearing capacity of the geocell-reinforced sand. Based on the measured strain of the NPA geocell, the maximum tensile strain (<1%) developed in the geocell was much lower than the tensile strain (>10%) needed to mobilize the ultimate tensile strength of the material.
- (3) The moving wheel test demonstrated the NPA geocell had a significant effect in improving the stability of unpaved roads and reducing the permanent deformation. Without geocell reinforcement, the unpaved road base with 15cm sand and 8.8cm AB3 cover could not support 80 kN (18 kips) traffic axle load for one pass. When NPA geocell reinforcement, the same base

course only developed 4.8cm rut depth after 5,000 wheel passes, which is comparable to the performance of a 23.8cm well-graded aggregate base course on the same subgrade.

- (4) Base course thickness is an important factor that influences the stability of the unpaved road under moving wheel loads. The geocell reinforcement must be thick enough for the unpaved road to be stable.
- (5) For the particular test setup in this study, the geocell-reinforced base course with an inadequate thickness had a “cell bursting” failure. Under the wheel load, both the vertical and the horizontal stresses in the base under the wheel path increased considerably. The lateral movement of soil was restricted by the geocell. When the tensile stresses at joints of geocell exceeded the tensile strength of the joint (typically lower than the tensile strength of the geocell material), the soil escaped through the geocell joint and moved laterally to both sides of the wheel path. The loss of the base material under the wheel path resulted in a significant increase in the rut depth of the road.
- (6) Strain gauges were installed on the NPA geocell for the static load test and the moving-wheel test. In the static load test, the maximum tensile strain measured in the geocell was 0.6%. In the moving-wheel test, the maximum tensile strain measured in the NPA geocell was 0.54% from the 15cm thick geocell and more than 2% from the 10cm thick geocell. The strain data also indicated that under the wheel load, the geocell along the wheel path experienced tensile stresses whereas the geocell outside the wheel path

experienced compressive stresses. As the deformation of the geocell increased, the horizontal stresses in the geocell outside the wheel tended to transfer from compression to tension.

6.1.2 Numerical analyses on geocell-reinforced granular soil under a static load

Conclusions drawn from the numerical analyses on geocell-reinforced soil under static load are:

- (1) With the geocell and the infill granular soil modeled separately, the numerical model developed in this study can simulate some key features in the performance of the geocell-reinforced soil, such as the increased confining stress and the restrained lateral displacement of the soil.
- (2) For the particular case modeled in the parametric study, the bearing capacity of the road was greatly improved (by about 43%) with the inclusion of geocell. The stiffness of the soil was also increased, but the benefit started to exhibit after about 5mm displacement was developed on the top surface. This result was also shown in the load test data obtained from the geocell-reinforced sand.
- (3) The parametric study also showed that on the firm subgrade, the thickness of the geocell-reinforced soil layer had a minor effect on the bearing capacity of the road.

- (4) Based on the parametric study, the Young's modulus of the geocell material is the most important parameter for the geocell to influence the performance of the geocell-reinforced soil under a static load. Geocell-soil interface shear modulus had almost no impact on the behavior of geocell-reinforced soil when the subgrade is firm.
- (5) The numerical result by varying of subgrade modulus and strength showed that geocell-reinforcement on top of relatively soft clay subgrade can achieve a performance that is equivalent to the unreinforced soil on top of stiff subgrade.

6.1.3 Numerical analyses on geocell-reinforced granular soil under a repeated load

Conclusions drawn from the numerical analyses on the geocell-reinforced soil under repeated load are:

- (1) The fundamental assumption of the mechanistic-empirical model is that the permanent deformation of the pavement structure becomes stable after a large number of wheel passes. The mechanistic-empirical model developed in this study also had this assumption but could well simulate the rutting behavior of the unpaved roads, as long as the road structure was stable.

- (2) The benefit of geocell reinforcement in reducing rutting depends on the quality of base course materials. When a relatively low-quality base material with a lower resilient modulus was used, the effect of geocell reinforcement became more significant. The benefit of geocell reinforcement decreased with a better-quality base course. Considering possible bearing capacity failure, geocell reinforcement is expected to have more benefit in reducing rut depths when a low-quality base is used.
- (3) The benefit of geocell reinforcement increased with an increase of the modulus (or tensile stiffness) of the geocell.
- (4) Both the type of infill material and the resilient modulus of subgrade significantly influenced the rut depth of the unpaved road.
- (5) The approach to consider the effect of geocell reinforcement in the current mechanistic-empirical design software (ME-PDG, version 1.1) is to input equivalent parameters for the reinforced layer. Analytical procedures was proposed in this study to determine these equivalent parameters (k_1 , k_2 , and k_3).
- (6) For an unpaved road, the bearing capacity of the road must be checked before running the mechanistic-empirical model. Numerical methods developed in Chapter 4 and Chapter 5 can be used together to analyze the unpaved road.

6.2 Recommendations for future studies

This research also identified some areas that need additional investigation.

These areas are recommended for future studies:

- (1) A standardized laboratory test should be developed for determining the joint strength of geocell, which is one of the key parameters in geocell design.
- (2) A finite element response model has been incorporated into the current MEPDG design software. A stress-dependent resilient modulus can be input into the program. However, the compaction-induced lateral earth pressure has not been considered into the initial stress distribution. In this study, it was found that the initial stress can greatly influence the resilient modulus of the granular soil, and thus affect the resilient strain distribution in the pavement structure. A future study is needed to verify the proposed compaction model from field earth pressure measurements.
- (3) According to the shakedown theory, there exists a threshold stress level (also called the shakedown limit) beyond which the soil will fail continuously under a repeated load. Such a threshold stress level can be determined in the laboratory by performing cyclic triaxial tests under different cyclic deviatoric stresses. A future study should be performed to find reliable correlation between this threshold stress level to index properties or other strength parameters that are easy to determine in the

lab. Such a correlation will greatly improve the current paved and unpaved design methods.

(4) The numerical models developed in this study can well simulate the behavior of the geocell-reinforced granular soil under static and repeated loads but they are difficult to be implemented into the current mechanistic-empirical design method. To better implement the geocell technology, a future study is needed to develop a simplified design procedure.

References

- Adams, M. T., and Collin, J. G. (1997). "Large model spread footing load tests on geosynthetic reinforced soil foundations." *Journal of Geotechnical and Geoenvironmental Engineering*, 123(1), 66-72.
- Andrei, D. (1999). "Development of a harmonized test protocol for the resilient modulus of unbound materials used in pavement design," M.S. Thesis, University of Maryland - College Park.
- Bardet, J. P. (1986). "Bounding surface plasticity model for sands." *Journal of Engineering Mechanics*, 112(11), 1198-1217.
- Barksdale, R. D. (1972). "Laboratory evaluation of rutting in base course materials." *3rd International Conference on Structure Design of Asphalt Pavements*, 161-174.
- Bathurst, R. J. (1988). "Large-Scale model tests of geocomposite mattresses over peat subgrade." *Transportation Research Record: Journal of Transportation Research Board*, 1188, 28-36.
- Bathurst, R. J., and Karpurapu, R. (1993). "Large-Scale triaxial compression testing of geocell-reinforced granular soils." *Geotechnical Testing Journal*, 16(3), 296-303.
- Bathurst, R. J., and Knight, M. A. (1998). "Analysis of Geocell Reinforced-Soil Covers over Large Span Conduits." *Computers and Geotechnics*, 22(3/4), 205-219.

- Bonaquist, R. F., and Witczak, M. W. (1997). "A comprehensive constitutive model for granular materials in flexible pavement structures." *Proceedings of the 8th International Conference on Asphalt Pavement*, 783-802.
- Boscardin, M. D., Selig, E. T., Lin, R.-S., and Yang, G.-R. (1990). "Hyperbolic parameters for compacted soils." *Journal of Geotechnical Engineering*, 116(1), 88-104.
- Boulbibane, M., Weichert, D., and Raad, L. (1999). "Numerical application of shakedown theory to pavements with anisotropic layer properties." *Transportation Research Record: Journal of Transportation Research Board*, 1687, 75-81.
- Collins, I. F., and Boulbibane, M. (2000). "Geomechanical analysis of unbound pavements based on shakedown theory." *Journal of Geotechnical and Geoenvironmental Engineering*, 126(1), 50-59.
- Collins, I. F., Wang, A. P., and Saunders, L. R. (1993a). "Shakedown in layered pavements under moving surface loads." *International Journal for Numerical and Analytical Methods in Geotechnics*, 17(3), 165-174.
- Collins, I. F., Wang, A. P., and Saunders, L. R. (1993b). "Shakedown theory and the design of unbound pavements." *Road & Transportation Research*, 2(4), 28-39.
- Dash, S. K., Rajagopal, K., and Krishnaswamy, N. R. (2004). "Performance of different geosynthetic reinforcement materials in sand foundations." *Geosynthetics International*, 11(1), 35-42.

- Dash, S. K., Sireesh, S., and Sitharam, T. G. (2003). "Model studies on circular footing supported on geocell reinforced sand underlain by soft clay." *Geotextiles and Geomembranes*(21), 197-219.
- De Garidel, R., and Morel, G. (1986). "New soil strengthening techniques by textile elements for low-volume roads." *the Third International Conference on Geotextiles*, Vienna, Austria, 1027-1032.
- Desai, C. S. (2007). "Unified DSC constitutive model for pavement materials with numerical implementation." *International Journal of Geomechanics*, 7(2), 83-101.
- Desai, C. S., and Faruque, M. O. (1984). "Constitutive model for (geological) materials." *Journal of Engineering Mechanics*, 110(9), 1391-1408.
- Duncan, J. M., Byrne, P., Wong, K. S., and Mabry, P. (1980). "Strength, Stress-Strain and Bulk Modulus Parameters for Finite Element Analyses of Stresses and Movements in Soil Masses." *UCB/GT/80-01*, University of California, Berkeley, CA.
- Duncan, J. M., and Seed, R. B. (1986). "Compaction-Induced earth pressures under K_0 -conditions." *Journal of Geotechnical Engineering*, 112(1), 1-22.
- Evan, M. D. (1994). "Geocell Mattress effects on the Embankment Settlements." *Vertical and horizontal deformations of foundations and embankments: Settlement '94*, 584-597.
- García-Rojo, R., and Hermann, H. J. (2005). "Shakedown of unbound granular material." *Granular Matter*, 7(2-3), 109-118.

- Han, J., Yang, X., Leshchinsky, D., and Parsons, R. L. (2008). "Behavior of geocell-reinforced sand under a vertical load." *Journal of Transportation Research Board*, n 2045, 95-101.
- Henkel, D. J., and Gilbert, G. D. (1952). "The effect of the rubber membrane on the measured triaxial compression strength of clay samples." *Geotechnique*, 3(1), 20-29.
- Hicks, R. G. (1970). "Factors influencing the resilient properties of granular materials," Ph.D. thesis, University of California, Berkeley, Berkeley, CA.
- Hicks, R. G., and Monismith, C. L. (1971). "Factors influencing the resilient response of granular materials." *Highway Research Record*, 345, 15-31.
- Huang, Y. (1993). *Pavement Analysis and Design*, Prentice Hall, Englewood Cliffs, NJ.
- Janbu, N. (1963). "Soil compressibility as determined by oedometer and triaxial tests " *European Conference on Soil Mechanics and Foundation Engineering*, Montreal, Germany, 19-25.
- Koiter, W. T. (1960). "General theorems for elastic-plastic solids." *Progress in Soil Mechanics*, 167-221.
- Kondner, R. L. (1963). "Hyperbolic stress-strain response: cohesive soils." *Journal of the Soil Mechanics and Foundations Division, ASCE*, 89(SM1), 115-143.
- Kwon, J., Tutumluer, E., and Al-Qadi, I. L. (2009). "A validated mechanistic model for geogrid base reinforced flexible pavements." *Journal of Transportation Engineering*, in press.

- Lade, P. V. (2005). "Overview of constitutive models for soils." *Geo-Frontiers 2005 Congress, Calibration of Constitutive Models (GSP 139)*, Austin, Texas, USA, 1-34.
- Lekarp, F., Isacsson, U., and Dawson, A. (2000a). "State of the art. I: Resilient response of unbound aggregates." *Journal of Transportation Engineering*, 126(1), 66-75.
- Lekarp, F., Isacsson, U., and Dawson, A. (2000b). "State of the art. II: Permanent strain response of unbound aggregates." *Journal of Transportation Engineering*, 126(1), 76-83.
- Ling, H. I., Cardany, C. P., and Sun, L.-X. (2000). "Finite element study of a geosynthetic-reinforced soil retaining wall with concrete-block facing." *Geosynthetics International*, 7(3), 163-188.
- Madhavi Latha, G. (2000). "Investigations on the behaviour of geocell supported embankments," Ph.D. Thesis, Indian Institute of Technology Madras, Chennai, India.
- Madhavi Latha, G., Dash, S. K., and Rajagopal, K. (2008). "Equivalent Continuum Simulations of Geocell Reinforced Sand Beds Supporting Strip Footings." *Geotechnical and Geological Engineering*.
- Madhavi Latha, G., Dash, S. K., and Rajagopal, K. (2009). "Numerical simulation of the behavior of geocell reinforced sand in foundations." *International Journal of Geomechanics*, 9(4), 143-152.

- Madhavi Latha, G., and Rajagopal, K. (2007). "Parametric Finite Element Analyses of Geocell-Supported Embankment." *Canadian Geotechnical Journal*, 44(8), 917-927.
- Madhavi Latha, G., Rajagopal, K., and Krishnaswamy, N. R. (2006). "Experimental and Theoretical Investigations on Geocell-Supported Embankments." *International Journal of Geomechanics*, 6(1), 30-35.
- Madhavi Latha, G., and Somwanshi, A. (2009). "Effect of reinforcement form on the bearing capacity of square footings on sand." *Geotextiles and Geomembranes*, 27(6), 409-422.
- Mandal, J. N., and Gupta, P. (1994). "Stability of geocell-reinforced soil." *Construction and building materials*, 8(1), 55-62.
- Melan, E. (1938). "Zur plastizitat des raumlichen Kontinuums." *Ing. Arch.*, 9, 116-125.
- Mengelt, M. J., Edil, T. B., and Benson, C. H. (2000). "Reinforcement of Flexible Pavements Using Geocells." *Geo Engineering Report No. 00-04*, University of Wisconsin-Madison, Madison, WN.
- Mhaiskar, S. Y., and Mandal, J. N. (1994). "Three dimensional geocell structure: performance under repetitive loads." 5th International conference on Geotextiles, Geomembranes, and Related Products, Singapore, 155-158.
- Mhaiskar, S. Y., and Mandal, J. N. (1996). "Investigations on soft clay subgrade strengthening using geocells." *Construction and building materials*, 10(4), 281-286.

- Mitchell, J. K., Kao, T.-C., and Kavazanjian Jr, E. (1979). "Analysis of Grid Cell Reinforced Pavement Base." *Technical Report GL-79-8*, Department of Civil Engineering, University of California, Berkeley, CA.
- Mróz, Z. (1983). "Constitutive model for sand with anisotropic hardening rule." *International Journal for Numerical and Analytical Methods in Geotechnics*, 7(3), 305-320.
- NCHRP. (2004). *Guide for Mechanistic-Empirical Design of New and Rehabilitated Pavement Structures*, ARA, Inc., ERES Consultants Division, Champaign, IL.
- Paute, J. L. (1988). "Modèle de calcul pour le dimensionnement des chaussées souples." *Bull. de Liaison des Laboratoires des Ponts et Chaussées*, 156, 21-36, (in French).
- Paute, J. L. (1994). "Comportement mécanique des graves non traitées." *Bull. de Liaison des Laboratoires des Ponts et Chaussées*, 190, 27-38, (in French).
- Pérez, I., Medina, L., and Romana, M. G. (2006). "Permanent deformation model for a granular material used in road pavements." *Construction & Building Materials*, 20(9), 790-800.
- Perkins, S. W. (2004). "Development of Design Methods for Geosynthetic Reinforced Flexible Pavements." *DTFH61-01-X-00068*, U.S. Department of Transportation, FHWA, Washington, D.C.
- Pokharel, S. K., Han, J., Leshchinsky, D., Parsons, R. L., and Halahmi, I. (2009a). "Behavior of geocell-reinforced granular bases under static and repeated loads." *International Foundation Congress & Equipment Expo 2009 -*

IFCEE '09, Geotechnical Special Publication No. 187, Orlando, FL, 409-416.

Pokharel, S. K., Han, J., Leshchinsky, D., Parsons, R. L., and Halahmi, I. (2009b).

"Experimental evaluation of influence factors for single geocell-reinforced sand." Oral presentation and CD publication at the TRB 88th Annual Meeting, Washington, DC.

Rajagopal, K., Krishnaswamy, N. R., and Latha, G. M. (1999). "Behaviour of Sand Confined with Single and Multiple Geocells." *Geotextiles and Geomembranes*, 17, 171-184.

Rea, C., and Mitchell, J. K. (1978). "Sand reinforcement using paper grid cells." *Symposium on Earth Reinforcement*, ASCE, Pittsburgh, 644-663.

Rodriguez-Roa, F. (2000). "Observed and calculated load-settlement relationship in a sandy gravel." *Canadian Geotechnical Journal*, 37, 333-342.

Sekine, E., Muramoto, K., and Tarumi, H. (1994). "Study on properties of road bed reinforced with geocell." *Quarterly Report of RTRI (Railway Technical Research Institute)(Japan)*, 35(1), 23-31.

Sharp, R., and Booker, J. (1984). "Shakedown of pavement under moving surface loads." *Journal of Transportation Engineering*, 110(1), 1-14.

Sweere, G. T. H. (1990). "Unbound Granular Bases for Roads," Ph.D. Dissertation, University of Delft, Delft, Netherlands.

Thallak, S. G., Saride, S., and Dash, S. K. (2007). "Performance of surface footing on geocell-reinforced soft clay beds." *Geotechnical and Geological Engineering*, 25, 509-524.

- Tseng, K., and Lytton, R. (1989). "Prediction of permanent deformation in flexible pavement materials." *Implication of Aggregates in the Design, Construction, and Performance of Flexible Pavements*, ASTM STP 1016, ASTM, 154-172.
- Uzan, J. (1985). "Characterization of granular material." *Transportation Research Record: Journal of Transportation Research Board*, 1022, 52-59.
- Webster, S. L. (1979a). "Investigation of Beach Sand Trafficability Enhancement Using Sand-Grid Confinement and Membrane Reinforcement Concepts; Report 1, Sand Test Sections 1 and 2." *Technical Report GL-79-20*, Geotechnical Laboratory, US Army Corps of Engineers Waterways Experimentation Station, Vicksburg, MS.
- Webster, S. L. (1979b). "Investigation of Beach Sand Trafficability Enhancement Using Sand-Grid Confinement and Membrane Reinforcement Concepts; Report 2, Sand Test Sections 3 and 4." *Technical Report GL-79-20*, Geotechnical Laboratory, US Army Corps of Engineers Waterways Experimentation Station, Vicksburg, MS.
- Webster, S. L., and Watkins, J. E. (1977). "Investigation of Construction Techniques for Tactical Bridge Approach Roads Across Soft Ground." *Technical Report S-77-1*, U.S. Army Engineer Waterways Experiment Station, Vicksburg, MS.
- Werkmeister, S., Dawson, A. R., and Wellner, F. (2003). "Design concept of unbound granular layers in pavement constructions." *Proceedings of the*

21st ARRB and 11th REAAA Conference. Transport. Our Highway to a Sustainable Future, Cairns, Australia.

Wesseloo, J. (2004). "The Strength and Stiffness of Geocell Support Packs," Ph.D. Dissertation, University of Pretoria, Pretoria, South Africa.

Wesseloo, J., Visser, A. T., and Rust, E. (2004). "A Mathematical Model for the Strain-Rate Dependent Stress-Strain Response of HDPE Geomembranes." *Geotextiles and Geomembranes*, 22, 273-295.

Wolff, H., and Visser, A. T. (1994). "Incorporating elasto-plasticity in granular layer pavement design." *Proc., Institution of Civil Engineers Transport*, 259-272.

Yau, A., and Von Quintus, H. L. (2002). "Study of LTPP laboratory resilient modulus test data and response characteristics." *FHWA-RD-02-051*, Fugro-BRE, Inc., Austin, TX.

Appendix A Cyclic triaxial tests on base materials and parameter calibration

To determine the resilient modulus and permanent deformation parameters, cyclic triaxial tests were conducted on two base materials, AB-3 and Kansas River sand, according to test standard AASHTO T 307. AB-3 and Kansas River sand samples were both prepared at the optimum water content and were compacted to 95% of the maximum density. The cyclic triaxial test results and the regression parameters were listed in Table A.1 to Table A.4. The permanent strain accumulation curves during the first 1000 conditioning load cycles were plotted together with the regression curves in Figure A.1 and Figure A.2.

Table A.1 Cyclic triaxial test on Kansas River Sand (resilient modulus)

Seq. No.	Load cycle	Confining stress σ_3 (kPa)	Maximum axial stress σ_1 (kPa)	Bulk stress θ (kPa)	Hexagonal shear stress τ_{oct} (MPa)	Resilient modulus Test M_r (MPa)	Regression M_r (MPa)
1	100	20.5	41.3	82.3	9.8	72.6	69.3
2	100	20.5	62.3	103.3	19.7	77	77.9
3	100	20.5	82.2	123.4	29.0	81.1	84.7
4	100	34.4	69.2	137.8	16.5	100	95.5
5	100	34.6	103.4	172.6	32.4	104.7	105.0
6	100	34.5	137.1	205.9	48.4	106.1	112.3
7	100	68.5	137.2	274.2	32.4	148	143.4
8	100	68.5	206.4	343.4	65.0	151.8	151.3
9	100	68.4	274.8	411.8	97.3	151.8	158.0
10	100	102.6	171.4	376.6	32.4	172.1	177.6
11	100	102.4	205.4	410.4	48.5	177.6	178.9
12	100	102.4	309.3	514.5	97.4	186.7	183.5
13	100	137.6	240.4	515.6	48.5	205.1	208.7
14	100	137.4	275.1	550.3	64.8	211.2	208.1
15	100	137.6	412.4	687.4	129.6	219	208.5
Regression Equation		$M_r = k_1 p_a \left(\frac{\theta}{p_a} \right)^{k_2} \left(\frac{\tau_{oct}}{p_a} + 1 \right)^{k_3}$					
Parameters		$k_1 = 820, \quad k_2 = 0.67, \quad k_3 = -0.45$					
R ²		0.992					

Table A.2 Cyclic triaxial test on Kansas River Sand (permanent deformation)

Confining stress σ_3	Maximum axial stress σ_1	Resilient strain ϵ_r	Regression Equation Regression parameters $\left(\frac{\epsilon_0}{\epsilon_r} \right)$	$\frac{\epsilon_p}{\epsilon_r} = \left(\frac{\epsilon_0}{\epsilon_r} \right) e^{-\left(\frac{\rho}{N} \right)^\beta}$ ρ	β
103.4	206.8	8.8×10 ⁻⁴	8.97	8.21×10 ³	0.095

Table A.3 Cyclic triaxial test on AB-3 (resilient modulus)

Seq. No.	Load cycle	Confining stress σ_3 (kPa)	Maximum axial stress σ_1 (kPa)	Bulk stress θ (kPa)	Hexagonal shear stress τ_{oct} (MPa)	Resilient modulus Test M_r (MPa)	Regression M_r (MPa)
1	100	20.5	41.1	82.1	9.7	118.1	116.3
2	100	20.5	62.3	103.3	19.7	126.2	127.8
3	100	20.5	82.1	123.1	29.0	134.1	136.9
4	100	34.4	69.3	138.1	16.5	155.1	150.2
5	100	34.6	103.0	172.2	32.2	168.5	162.2
6	100	34.5	137.1	206.1	48.4	168.5	172.0
7	100	68.5	137.2	274.2	32.4	216.9	207.3
8	100	68.5	206.0	343.0	64.8	220.0	217.7
9	100	68.4	274.7	411.5	97.3	205.4	226.4
10	100	102.6	171.3	376.5	32.4	226.2	245.0
11	100	102.4	205.2	410.0	48.5	238.8	247.2
12	100	102.4	309.2	514.0	97.5	254.9	254.5
13	100	137.6	240.3	515.5	48.4	281.7	279.0
14	100	137.4	275.3	550.1	65.0	293.0	279.2
15	100	137.6	413.0	688.2	129.8	301.8	283.0
Regression Equation		$M_r = k_1 p_a \left(\frac{\theta}{p_a} \right)^{k_2} \left(\frac{\tau_{oct}}{p_a} + 1 \right)^{k_3}$					
Parameters		$k_1 = 1312, \quad k_2 = 0.53, \quad k_3 = -0.32$					
R ²		0.978					

Table A.4 Cyclic triaxial test on AB-3 (permanent deformation)

Confining stress σ_3	Maximum axial stress σ_1	Resilient strain ϵ_r	Regression Equation Regression parameters $\left(\frac{\epsilon_0}{\epsilon_r} \right)$	$\frac{\epsilon_p}{\epsilon_r} = \left(\frac{\epsilon_0}{\epsilon_r} \right) e^{-\left(\frac{\rho}{N} \right)^\beta}$	
				ρ	β
103.4	206.8	7.3×10 ⁻⁴	8.82	201.44	0.119

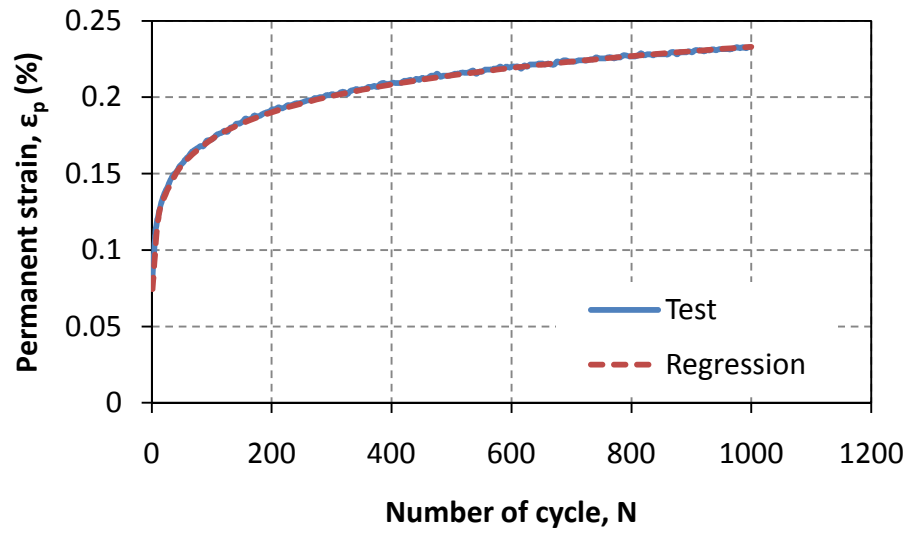


Figure A.1 Permanent strain accumulation of Kansas River Sand

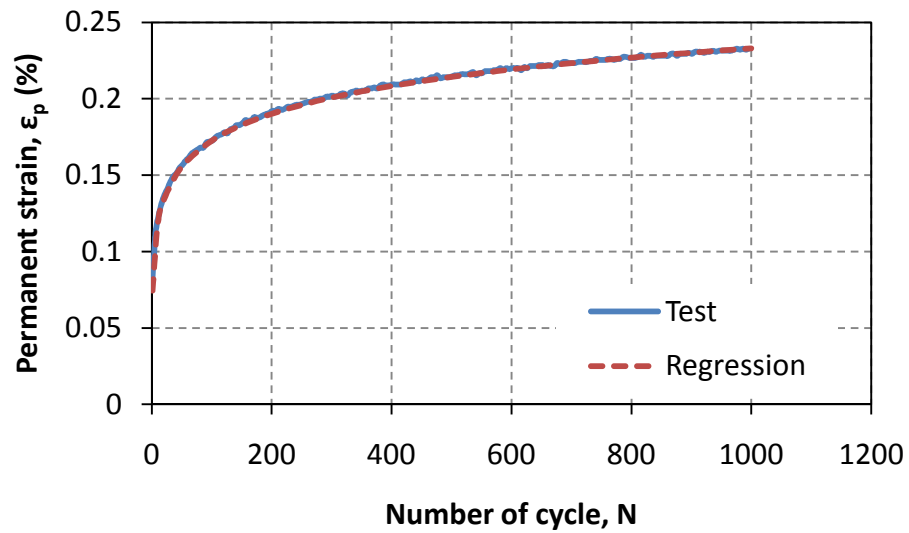


Figure A.2 Permanent strain accumulation of AB3